

# 2013

## Annual Report Jahresbericht

### Remote Sensing Technology Institute

Department  
Atmospheric Processors



<b>Published by</b>	<b>German Aerospace Center (DLR)</b> A member of the Helmholtz Association
	<b>Remote Sensing Technology Institute</b> Institut für Methodik der Fernerkundung (MF)
	Department <b>Atmospheric Processors (MF-ATP)</b>
<b>Department Head</b>	Prof. Dr. Thomas Trautmann
<b>Editorial Team</b>	Prof. Dr. Thomas Trautmann Dr. Manfred Gottwald
<b>Layout</b>	Dr. Manfred Gottwald
<b>Cover</b>	The “Ring of Fire” around the Pacific Ocean. Volcanic eruptions are detected via their SO <sub>2</sub> emission by the GOME-2 instrument on-board the MetOp platform. They trace the regions with high tectonic activity, mainly at the edges of tectonic plates (see chapter 4.2). The underlying elevation model is NOAA’s ETOPO1 model.

## Contents

<b>1. Foreword</b> .....	<b>3</b>
<b>2. Atmospheric Remote Sensing – Missions and Sensors</b> .....	<b>5</b>
2.1 SCIAMACHY Processors and Products.....	5
2.2 Instrument Studies for Sentinel 4 and Sentinel 5.....	9
2.3 MERLIN – The Methane Remote Sensing Lidar Mission .....	11
2.4 The CarbonSat Mission .....	13
<b>3. Atmospheric Remote Sensing – Methods</b> .....	<b>15</b>
3.1 Operational O3M-SAF Trace Gas Column Products from GOME-2 on MetOp-A and -B.....	15
3.2 Water Vapour Column Density Time Series from GOME, SCIAMACHY and GOME-2 Instruments.....	17
3.3 The Sentinel 5 Precursor Mission .....	21
3.4 Carbon Monoxide Retrievals from Shortwave Infrared Observations of SCIAMACHY .....	26
3.5 Retrieval of Stratospheric HCl in Activated Arctic Air from TELIS Far-Infrared Data.....	28
3.6 A First Look at Temperature Retrieval by the Microwave Temperature Profiler.....	29
3.7 Scattering Simulations for the ADM-Aeolus Mission .....	31
3.8 Scattering Data Base for Ice Particles to Study the Scattering Greenhouse Effect of CO <sub>2</sub> Ice Clouds .....	33
3.9 GARLIC – Generic Atmospheric Radiation Line-by-Line Infrared Code .....	35
3.10 A New Version of the OPAC Software.....	37
3.11 Three-dimensional Radiative Transfer: Effects of Cloud Variability on TROPOMI Reflectivity Spectra.....	39
3.12 Discrete Ordinate Method with Matrix Exponential for Stochastic Radiative Transfer in Broken Cloud Fields .....	41
3.13 Dimensionality Reduction Techniques for Trace Gas Retrieval: Principal Component Analysis and Alternatives .....	43
<b>4. Atmospheric Remote Sensing – Applications</b> .....	<b>45</b>
4.1 The Ozone_CCI Project .....	45
4.2 Detection and Monitoring of Volcanic Eruptions with the GOME-2 Instrument .....	47
4.3 Dragon 3: Impact of the East Asian Monsoon on Tropospheric Ozone over Hong Kong .....	49
4.4 Textbook on Mathematical Chemistry and Chemoinformatics and its Relevance to Astrobiology.....	53
4.5 Jacobian Matrix of the Atmospheres of Earth-like Planets .....	55
4.6 Earth and Space Science Outreach Activities in the Dominican Republic.....	56
<b>5. Documentation</b> .....	<b>59</b>
5.1 Books and Book Contributions.....	59
5.2 Journal Papers .....	59
5.3 Conference Proceeding Papers and Presentations.....	61
5.4 Attended Conferences.....	64
5.5 Academic Degrees.....	65
5.6 Seminar Talks .....	65
<b>Abbreviations and Acronyms</b> .....	<b>67</b>



## 1. Foreword

For us, the past year 2013 marked a real transition - from the era of atmospheric sounding using ESA's first and second generation large Earth observation platforms ERS-2 and ENVISAT to the multiple capabilities offered by Europe's Copernicus program in the near future. Although both GOME/ERS and SCIAMACHY/ENVISAT data are not yet fully exploited and will still provide information for a better understanding of the changing Earth's atmosphere, our involvement in the new Sentinel missions, together with further fulfilling our responsibilities for GOME-2 on EUMETSAT's MetOp platforms, has now received much higher priorities. The ambitious schedule for the Sentinel 5 Precursor with an envisaged launch already in late 2015 is currently one of our major challenges where we intend to provide substantial contributions to the payload ground segment. When successfully accomplished, we will have an outstanding role in this mission. We consider the Sentinel 5 Precursor a stepping stone for the continuation of our now almost 20 year long experience in space-borne remote sensing of the atmosphere.

The year 2013 required not only to prepare for the future but also to look back and recapitulate what had been achieved in previous years. It was needed in support of the second evaluation of the Earth Observation Center. A detailed report summarized the scientific and engineering highlights of our entire institute. We contributed the chapter *Spectrometric Sounding of the Atmosphere*, a comprehensive description of what we and colleagues from the department *Experimental Methods* accomplished in the time period 2007-2013 in that field. This chapter nicely illustrated how multifaceted our research meanwhile has become. We hope, that this trend will continue with new and exciting challenges emerging from new missions and scientific problems.

This annual report demonstrates again that atmospheric sounding is no longer restricted to our home planet but reaches far into space where the atmospheres of exoplanets await their understanding. And this opens even more opportunities like speculating of how life started to evolve or participating in exciting Earth and space science outreach activities. In the beginning this is always based on individual motivation but has the potential to attract a wider community.

A summary of the past year would be incomplete without thanking Brigitte Rüba who was our secretary for more than 12 years. She retired by the end of 2013. She was always the right contact and helped to maintain a smooth running of our department. We wish her all the best.

Our thanks go also to our staff for their efforts and achievements in 2013 and their contributions to this annual report.

Prof. Dr. Thomas Trautmann  
Dr. Manfred Gottwald



## 2. Atmospheric Remote Sensing – Missions and Sensors

### 2.1 SCIAMACHY Processors and Products

*G. Lichtenberg, B. Aberle, A. Doicu, S. Gimeno García, S. Hrechanyy, M. Meringer, F. Schreier, D. Scherbakov, S. Slijkhuis*

SCIAMACHY's data processors, both for level 1 and level 2, will experience major modifications with the next release when version V7.04 will be replaced by version V.8.

#### **Level 0-1 Processing**

The implementation and verification of the new level 0-1 processor version was finished in early 2013. Since the level 0-1 processor underwent extensive changes (see Table 2-1), the remainder of the year had to investigate the impact of these changes on level 2. It turned out that due to the chosen reference point of the degradation correction, the ozone total columns showed an unphysical change with time. A new version of m-factors was provided in October and the verification data sets for level 1 and level 2 were recalculated. With the new m-factors, the total column no longer displayed the induced trend with the values being overall improved.

Change	Description
Stray light channels 3-8	Extend matrix correction approach to channels 3-8.
Memory correction limb	Correct and improve the estimate of the previous signal for the first scan at a given tangent height.
PMD scaling nadir/limb	Improve scaling for low signal cases.
Hot pixel correction limb	Implement more robust hot pixel detection.
Polarization occultation off	Do not calculate polarisation correction for Occultation measurements. Since the available calibration data are not valid for this instrument mode, we do not provide polarisation values anymore.
SAA check for etalon off	Usually no calibration values are calculated in the Southern Atlantic Anomaly. However, etalon calculation is not impacted by the SAA, since cosmics are filtered out before.
Dark selection for fit	Implement a selection option to specify which of the 5 dark states should be used for dark signal correction.
New Key Data for polarization and radiance	New key data are used for calculation.
Scan mirror model	The scan mirror model from SRON is now used to correct degradation.
m-factor correction for pmd_int	Write the degradation corrected, integrated PMD values to the level 1b product.

Table 2-1: Summary of changes to level 0-1 processing included in version V.8.

The modifications concerning the memory effect correction and the dark signal correction deserve a closer look. The memory effect is an "after image" caused by the previous exposure of the detector in channels 1-5. The correction for limb data is particularly complicated by the fact that at each new tangent height a reset readout is done, which is discarded. Thus, to apply the correction, the signal for the first (reset) readout has to be estimated. The current V.7.04 processor estimation of the signal led to a "zig-zag" of the correction, especially at the end of the limb state where the signal (and thus the

actual memory effect) is rather constant. The new correction in V.8 introduces a more sophisticated estimate, taking properly into account the movement of the mirrors during the reset readout using the last state before the reset readout and the first state after it to interpolate the signal.

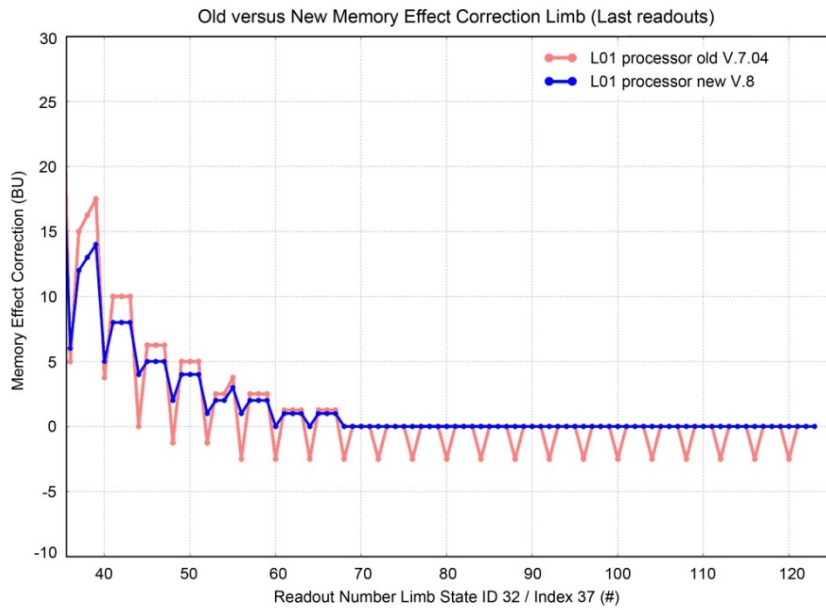


Fig. 2-1: Old (red) and new (blue) memory effect correction for limb measurements.

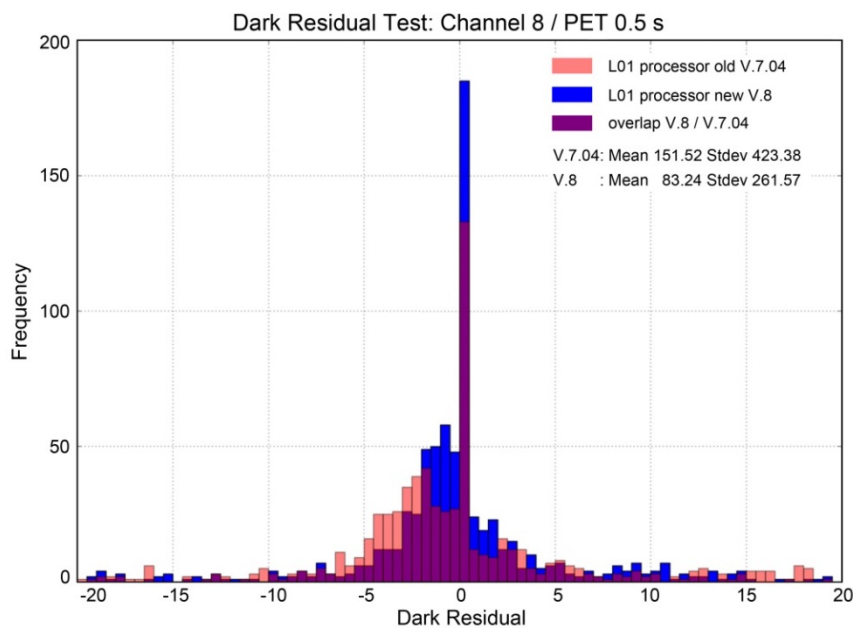


Fig. 2-2: Histogram of residuals for one dark state using all dark states (red) and leaving out problematic states (blue).

For the dark correction the possibility of selecting only certain dark measurements used in the calculation of the correction was introduced. This is especially useful for the SWIR channels, where very short exposure times might be influenced by non-linearity. Discarding states with the shortest integration time improves the dark residual considerably: Most of the values lie between -3 and 3 Binary Units (BU) with now fewer outliers. Note that the background signal is several 1000 BU and a residual of a few BU is considered a very good value. Some additional variance might come from the fact that for this test we did not take the orbital variation fully into account and that some bad pixels possibly remained undetected.

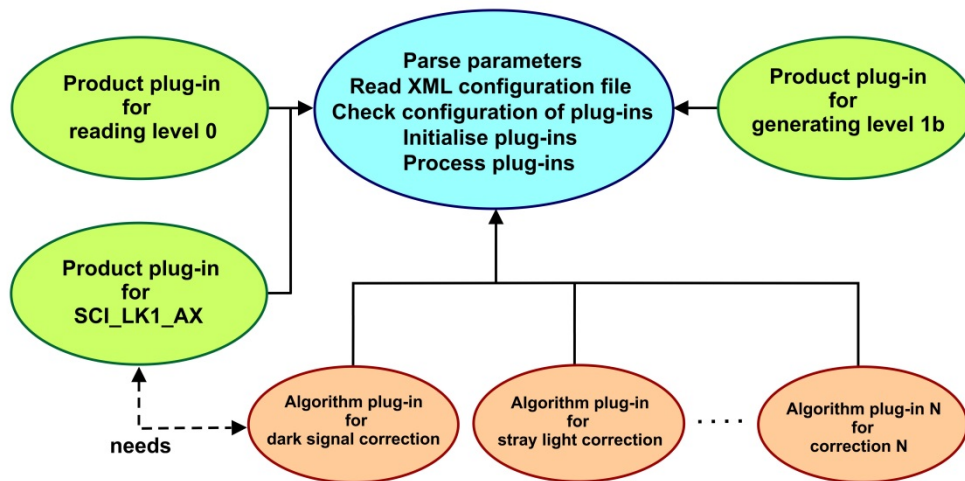


Fig. 2-3: Plugin architecture of the generic framework GCAPS. A processor for a given instrument is realised by implementing input/output plugins, algorithm plugins and by defining the processor calibration chains and logic in the configuration file. The framework provides interfaces to easily write the plugins.

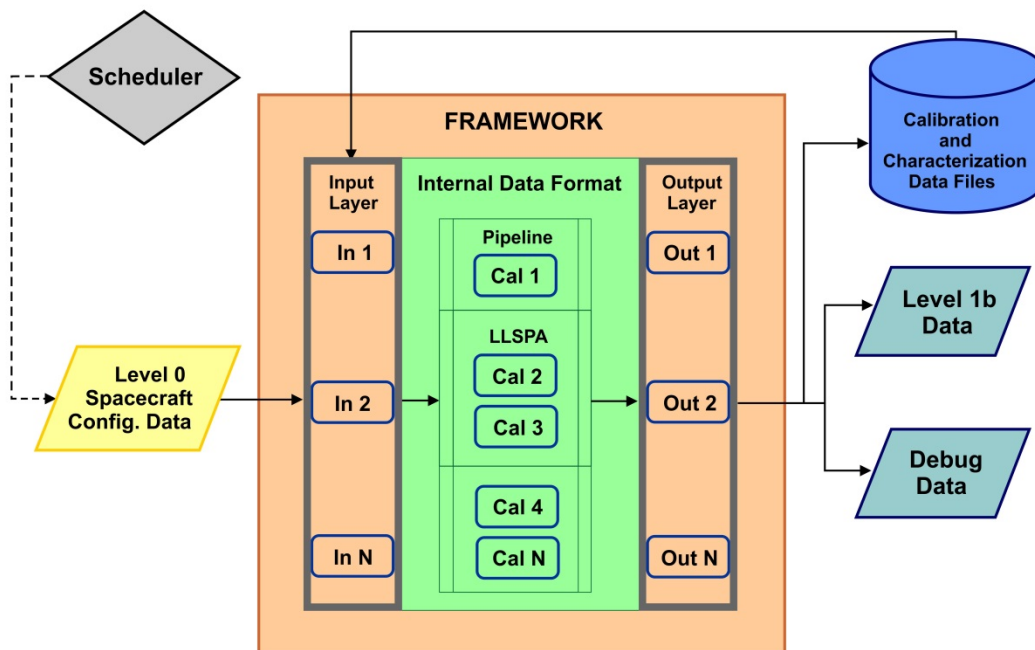


Fig. 2-4: Data flows for the framework. All data are passed through input and output plugins and are processed in the core using a separated internal data representation (green). Different calibration chains, e.g. pipeline processing for regular data and long loop sensor performance analysis (LLSPA) can be defined in the configuration file. Where needed, different chains can share individual algorithms.

In addition to the changes listed above we modified the approach how to transfer the algorithms to the operational system. Previously, we provided the prototype code (IDL) and its specification. This was then used by industry to code the operational processor. Several disadvantages existed:

- Long turn around times (> 6 months) between final prototype and operational processor.
- IDL prototype was used quasi-operational for the re-processing of calibration data, but was inadequate for this purpose because it was never intended to be used this way (e.g. processing a whole orbit required 100 min)

The new approach uses the DLR developed generic level 0-1 processor C++ framework GCAPS (Generic Calibration Processing System) and the processor is directly implemented in the ground segment without a third party re-implementation. Now the advantages are:

- The complete processing logic exists in the configuration file and not in the code.
- No separation between "prototype" and operational code, the only difference is the environment. Thus the transfer and testing is much simplified.
- C++ code, multi-thread capable, needs 3-5 minutes per orbit

The processor consists of a framework that handles the data flow and provides an easy interface for input/output plugin and algorithm plugins. Its internal data representation is completely independent from input and output format, thus different formats can easily be added without the need to change the algorithmic core (Fig. 2-3 and 2-4).

### **The Level 1b-2 Processor**

The next processor version (V.6) will add 4 new nadir and one new limb product in addition to several other improvements. Table 2-2 gives an overview of the history of processor development since the establishment of the SCIAMACHY Quality Working Group (SQWG).

	V 3.01	(V 4)	V 5/5.02	V 6
<b>Nadir</b>				
O <sub>3</sub>	improved <sup>1</sup>	improved	maintenance	maintenance
NO <sub>2</sub>	improved	improved	maintenance	maintenance
AAI	improved	new algorithm <sup>3</sup>	maintenance	improved
CTH	improved	maintenance <sup>2</sup>	maintenance	maintenance
CFR	improved	maintenance	improved	improved
SO <sub>2</sub>		new <sup>4</sup> (SCD)	improved (VCD)	improved
BrO		new (SCD)	improved (VCD)	maintenance
OCIO			new (SCD)	improved
H <sub>2</sub> O			new	maintenance
CO			new	improved
CHOCHO				new
HCHO				new
CH <sub>4</sub>				new
<b>Limb</b>				
O <sub>3</sub>	improved	improved	improved	improved
NO <sub>2</sub>	improved	improved	maintenance	maintenance
BrO			new	maintenance
Cloud			new	improved
<b>Limb/Nadir</b>				
Tropospheric NO <sub>2</sub>				new

<sup>1</sup> improved: Algorithm/entries of product were improved.

<sup>2</sup> maintenance: Algorithms was checked versus validation and bugs

<sup>3</sup> new algorithm: Newly implemented algorithm, same product

<sup>4</sup> new: New product (SCD or VCD marks the introduction of the vertical or slant column density)

Table 2-2: Product improvements in the level 1b-2 processor since the SQWG was established. The algorithms are developed in collaboration with BIRA, IUP-IFE Bremen, KNMI and SRON. Tropospheric NO<sub>2</sub> will exist in V.6 or V.7 depending on the maturity of the operational algorithm. V.4 was delivered to ESA, but was not implemented in the ground segment due to delays in the ground segment migration to Linux.

The main focus of the past year was the verification of the newly implemented algorithms and the investigation of the impact of the level 1 changes on the level 2 retrievals. Table 2-3 lists the current status of our work.

Product	Remark
<b>Nadir</b>	
O <sub>3</sub> , NO <sub>2</sub> , HCHO, CHOCHO, H <sub>2</sub> O, CH <sub>4</sub> , Cloud Parameters	<b>Verification complete</b>
BrO,OCIO	<b>Verification complete.</b> 8 orbits deviate for both, reference and operational processor.
CO	L1b V.8 gives degraded results compared to L1b V.7 and previous operational version. A detailed investigation is planned.
AAI	<b>Verification complete.</b> However, data set should be extended to 2011/2012 and the varying time behavior will be investigated.
<b>Limb</b>	
O <sub>3</sub> , NO <sub>2</sub> , BrO	<b>Verification complete</b>
NLCs, Water Clouds, Ice Clouds, PSCs	<b>Verification complete.</b> For 12 orbits of the verification data set the height of the maximum Cloud Index Ratio (CIR) differs when L1b V.8 is used (compared to V.7). For the other orbits the results agree. Further investigations are planned.

Table 2-3: Summary of the study of the impact of level 1 changes on level 2 products in 2013.

Compared to the previous processor version the total column values of CO are now much too low. The investigation showed that this is an effect of the level 1 changes: Using the level 1 V.7 input for the CO retrieval, the values are the same as for the current operational processor. Thus, since the level 2 retrieval remained unchanged, the decrease of the total columns is caused directly either by a change in the level 1 spectra or an incompatibility between the level 2 retrieval settings and the level 1 spectra. However, except for CO total columns and a few outliers in some of the other products, the level 1 changes improved the quality of the level 2 products. The investigation will be continued in 2014 to cure the remaining issues.

## 2.2 Instrument Studies for Sentinel 4 and Sentinel 5

*G. Lichtenberg, S. Slijkhuis, M. Hamidouche*

Both Sentinels are part of the European Copernicus program. They will provide atmospheric services in the next decade. For us, participation in the Sentinel 4 and 5 missions means continuity in space-borne spectrometric sounding of the Earth's atmosphere. Presently we contribute studies covering calibration aspects for Sentinel-4 UVN, Sentinel-5 UVNS.

### **Sentinel-4 UVN Instrument**

The Sentinel-4 mission will be launched 2019 into a geostationary orbit on-board the Meteosat Third Generation Sounder platform (MTG-S). A second satellite with the same instrumentation is planned to be launched 2026. Thus a long-term, consistent data set for the monitoring of Earth's atmosphere can be ensured. Both platforms comprise two instruments: The thermal infrared sounder IRS and the UVN spectrometer for measuring from the UV to the near infrared (NIR). UVN shall obtain spectra with moderate spectral resolution and a spatial sampling of better than 10 km. Owing to the geostationary in-orbit position, the observations cover the area from 30°-65° N in latitude and 30° W-45° E in longitude, i.e. focus on Europe. Their repeat cycle will amount to one hour or even shorter thus enabling the instruments for the first time to detect short-term changes of the atmospheric composition – main target species will be O<sub>3</sub>, NO<sub>2</sub>, SO<sub>2</sub>, HCHO and aerosol optical depth – over Europe throughout the day.

We are involved in the definition of the level 0-1 processor for the calibration of the S4-UVN instrument and the implementation of algorithms for its spectral calibration, its stray light correction and the instrument calibration and characterization database.

### **Sentinel-5 UVNS Instrument**

The Sentinel-5 mission will be launched on the EUMETSAT Polar System Second Generation (EPS-SG) satellite into a polar low-Earth orbit. It comprises an Ultraviolet Visible Near-infrared Shortwave (UVNS) spectrometer, the thermal infrared sounder IRS, the Visible Infrared Imager (VII) and the Multi-viewing Multi-channel Multi-polarization Imager (3MI). The UVNS spectrometer covers the UV, the VIS and the NIR bands together with two SWIR channels. Its prime focus will be air quality and composition-climate interactions, with the main data products being O<sub>3</sub>, NO<sub>2</sub>, SO<sub>2</sub>, HCHO, CO, CH<sub>4</sub> and aerosol optical depth and, potentially, CO<sub>2</sub>. The specific objective is to support global air quality monitoring and forecast on a daily basis. Similar to our Sentinel 4 tasks, we contribute, in the now concluded Phase A/B1 within the consortium led by Kayser-Threde, to the definition of the level 0-1 processor for the calibration of the S5-UVNS instrument, the implementation of algorithms for the spectral calibration and how to handle heterogeneous scenes during processing.

### **Spectral Calibration Algorithms**

For both instruments we investigated the spectral calibration. We implemented a method suggested earlier by IUP-IFE Bremen that uses a DOAS-type algorithm fitting wavelength and radiance at the same time with a non-linear Levenberg-Marquardt fit. Since the goal of the study was to find an optimum parameter set, the algorithm was implemented in several variants:

- Use the complete spectrum and do one fit over the spectrum and optionally an absorber (this was the original method proposed in the IUP-IFE study).
- Use microwindows, concatenate these and do a fit.
- Use microwindows, perform the fit for each microwindow and do a second polynomial fit using the results of the individual microwindow fits to obtain the calibration for the whole channel.
- Use an arbitrary number of absorbers.

In order to estimate the performance for a given mission, we modeled instrument spectra for different scenarios such as a change in the shape of the instrument spectral response function (ISRF) or wavelength shifts. We also tested what precision could be achieved using spectral line sources. As part of the S4-UVN studies we also compared the performance of the spectral calibration algorithm with the nominal calibration of GOME-2 (Fig. 2-5) and OMI.

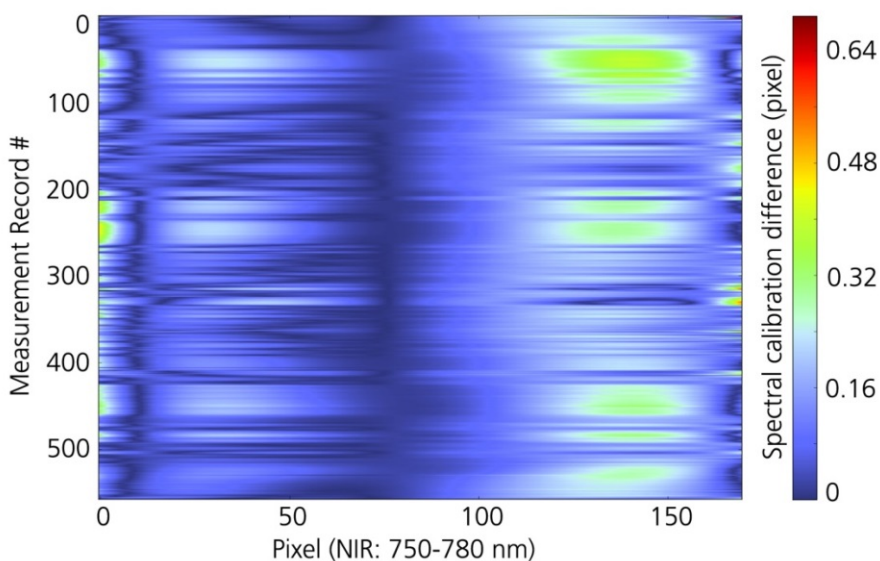


Fig. 2-5: Comparison between spectral calibration of the GOME-2 A Band 4 NIR range using the on-board spectral line source and using a spectral calibration derived from the spectrum itself. The latter method might be used to correct for scene inhomogeneity dependent spectral shifts. Differences between the two approaches are shown in units of spectral pixels for one orbit (y-axis).

### **Determination of Instrument Spectral Response Function**

For each of the instrument's five bands, one needs to retrieve its ISRF in-flight in order to track any change of its shape or FWHM during the entire mission lifetime. To retrieve such an in-flight ISRF, we

developed a mathematical algorithm using different instrument parameters. We simulated two separate cases, one using solar spectra and the other using laser lines for the in-flight measurements. We had in hand raw solar spectra and we simulated laser lines at different wavelengths.

First, we modeled the ISRF's from the instrument characteristics. Typically, the ISRF is an exponential function, and contains the main free parameters in our fitting strategy. Next, we simulated the *in-flight* measurements by convolving raw solar spectra or simulated laser lines with this *modeled* ISRF, and added simulated in-flight noise. Furthermore, we obtained the *actual* ISRF from the instrument's designers' team. In a similar way as before, we calculated the *actual* measurements by convolving the actual ISRF with raw solar spectra or laser lines, to which we also added noise. Finally, we fitted the actual measurement to the modeled one. From the best fit, we retained the corresponding modeled ISRF. We analyzed it and compared it to the actual one. We deduced that the modeled ISRF matches nicely the *actual* one, in both shape and FWHM. Thus, our algorithm is capable of fully retrieving the *in-flight* ISRF.

## 2.3 MERLIN – The Methane Remote Sensing Lidar Mission

*M. Hamidouche, G. Lichtenberg, D. Scherbakov, T. Trautmann*

After water vapour and carbon dioxide, methane ( $\text{CH}_4$ ) is the most abundant greenhouse gas in the Earth atmosphere. In the context of the global warming it is of paramount importance to understand its cycle on a global scale, both in terms of sources and sinks. The goal of the MERLIN (Methane Remote Sensing Lidar Mission) mission is to provide this information. It shall make very sensitive measurements of the methane distribution with unprecedented quality, i.e. 50 km averaged methane columns with an accuracy of about 1%. MERLIN is a joint project of DLR and the French space agency CNES. Germany has agreed to develop and operate the space based methane lidar (Light Detection and Ranging) instrument while France provides the satellite platform.

MERLIN is the first European mission using an active spaceborne instrument – IPDA, the Integrated Path Differential Absorption Lidar – to obtain measurements of the column content of a specific atmospheric trace gas. In this case, the difference in atmospheric transmission between a laser emission with a wavelength placed at, or near, the center of a  $\text{CH}_4$  absorption line ( $\lambda_{\text{on}} \approx 1.6 \mu\text{m}$ ) and a reference wavelength ( $\lambda_{\text{off}}$ ), located where the absorption is smaller, is exploited (Fig. 2-6).  $\lambda_{\text{off}}$  is slightly shifted by a few tenths of a nm from  $\lambda_{\text{on}}$  (Kiemle *et al.* 2011). The Laser double pulse (on/off) is emitted at a pulse rate of 12 Hz.

With an anticipated launch date in 2017, MERLIN is one of the next atmospheric remote sensing missions with major contributions by us. These cover tasks in instrument performance monitoring and payload data processing.

### ***Payload Long-Term-Monitoring***

During the commissioning and routine operations phase, the task of long-term instrument monitoring is one of the key ground segment functions. It tracks the performance of the instrument and its subsystems on a daily up to a monthly basis. This includes monitoring the behavior in response to planned or unexpected operational situations or a changing in-orbit environment, e.g. induced by the space weather. Long-term monitoring extracts information from various channels such as recorded calibrated housekeeping telemetry, measurement data, as well as calibration parameters. As an example, monitoring the spacecraft attitude is required since any slight rotations could affect the measured backscattered laser

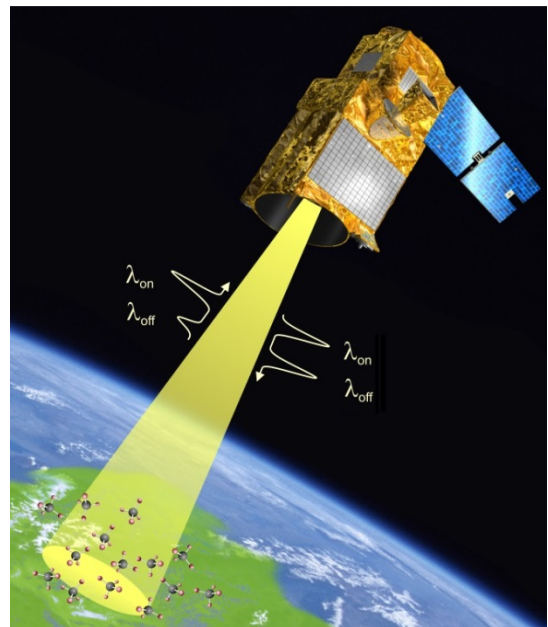


Fig. 2-6: The instrument sends and receives the backscattered laser light at both  $\lambda_{\text{on}}$  and  $\lambda_{\text{off}}$ .

via the Doppler effect. Additionally, the laser pulses ( $\lambda_{on}$ ,  $\lambda_{off}$ ) are among the key items to be closely monitored. Only when precise knowledge about pulse's time of fire, return time, and energy is maintained, a reliable measurement of the relative signal intensities (on/off) can be accomplished.

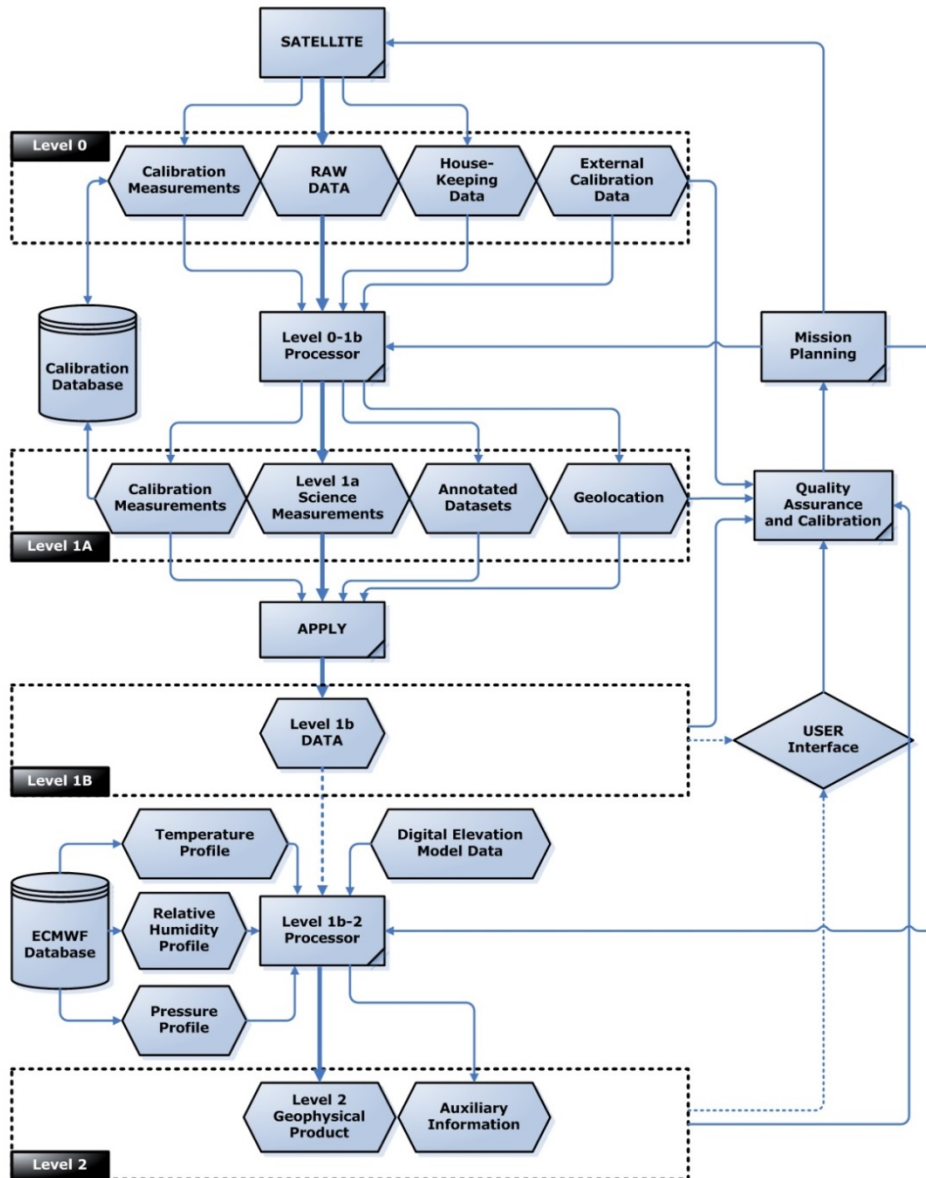


Fig. 2-7: Processing flow for MERLIN from level 0 to level 2.

### ***Payload Data Processing***

In the realm of data processing we deal with the level 0-1b processing. This step will provide the differential absorption optical thickness (DAOD) for further processing to level 2. A sequence of calibration steps needs to be performed:

- correct for solar background and detector dark signal
- correct the detector non-linearity
- correct frequency shifts
- calculate geolocation
- classify pulses with respect to their quality
- using the quality, generate a weighted average individual pulse (pairs) to achieve sufficient signal-to-noise.
- detect possible clouds

- correct for degradation
- calculate the DAOD

The basis of the algorithms will be the level 0-1 Algorithm Theoretical Baseline Document provided by DLR-IPA. Two products are the result of the corresponding processing step: Level 1a with raw data and calibration parameters and level 1b with calibrated data. The processor will be based on our GCAPS framework (see chapter 2-1). It will run directly in the CNES ground segment without a third party re-implementation. Level 1b will be used as input to the level 1b-2 processor developed by CNES to provide methane concentrations. A preliminary processing flow is illustrated in Fig. 2-7.

### References

*Kiemle C., Quatrevalet M., Ehret G., Amediek A., Fix A., Wirth M.:* Sensitivity studies for a spaceborne methane lidar mission. *Atmos. Meas. Tech.*, 4, 2195-2211, 2011.

## **2.4 The CarbonSat Mission**

*M. Hamidouche, S.Slijkhuis*

CO<sub>2</sub> and CH<sub>4</sub> are two greenhouse gases that are directly affected by anthropogenic, e.g. fossil fuel combustion, and natural activities. A thorough knowledge of their sources and sinks is essential for studying the future of our Planet's climate. Detailed measurements with high spatial resolution as well as a large coverage of the Earth's surface will play a key role for such investigations. CarbonSat (Carbon Monitoring Satellite) can achieve this. It will map for the first time detailed spatial patterns of CO<sub>2</sub> emission with a resolution of 2 × 2 km<sup>2</sup> and a good global coverage; the aim is 500 km swath.

Together with FLEX (Fluorescence Explorer), CarbonSat was selected to be one of the two ESA Earth Explorers candidates to enter Phase A/B1. These phases include the feasibility study and a consolidation of their different components constituting finally a successful satellite mission. We participate in the areas of level 0-1 processing and the spectral calibration.

### **Level 0 to 1b processing**

We support the prime contractor, Astrium, in deriving the approach for in-flight calibration and on-ground data processing from the uncalibrated instrument signals (level 0) to the calibrated atmospheric radiance and solar irradiance (level 1). Based on instrument design, including instrument stability, this incorporates a trade-off between calibration complexity and instrument requirements, and – from Astrium side – between technical feasibility and cost. A point of attention for level 0-1b processing is the data volume, which will be even higher than that of the already challenging Sentinel-5 mission. Our tasks shall finally deliver the CarbonSat's level 0-1b Algorithm Theoretical Baseline Document (ATBD).

### **Spectral Calibration**

As a subcontractor to Astrium, we also perform the spectral calibration work package for CarbonSat. We used the same DOAS algorithm as for Sentinel 5 (see chapter 2.2) and modeled different measurement scenarios by using different spectra (several Earth radiances and the solar irradiance). In addition, we incorporated the atmospheric molecular absorptions generated from infrared atmospheric radiative transfer models. Furthermore, we simulated slight variations which could occur during flight, such as, e.g., a deformation of the Instrument Spectral Response Function (ISRF).

In both areas work is ongoing. Assuming that CarbonSat will be selected for flight, our goal is to also play a major role when it comes to specifying, implementing and operating the associated payload data ground segment.



### 3. Atmospheric Remote Sensing – Methods

#### 3.1 Operational O3M-SAF Trace Gas Column Products from GOME-2 on MetOp-A and -B

*P. Valks, N. Hao, M. Grossi, P. Hedelt, D. Loyola, H. Bauer, W. Zimmer*

The operational GOME-2 trace gas column and cloud products from MetOp-A and MetOp-B are provided by MF-ATP in the framework of EUMETSAT's Satellite Application Facility on Ozone and Atmospheric Chemistry Monitoring (O3M-SAF). The current GOME-2 trace gas products of the O3M-SAF include total ozone, total and tropospheric NO<sub>2</sub>, SO<sub>2</sub>, BrO, formaldehyde and water vapour. The O3M-SAF trace gas column products are generated operationally at DLR using the GOME Data Processor (GDP) version 4.7 (Valks *et al.* 2013). The GOME-2 trace gas column data from MetOp-A and -B are used in the near-realtime system of the Copernicus atmospheric service project MACC (Monitoring Atmospheric Composition and Climate, see Hao *et al.* 2013). During the second Continuous Development and Operation Phase (CDOP-2) of the O3M-SAF (2012-2017), the focus will be on the development of new and better products, on new dissemination methods and on improved user services. New GOME-2 trace gas column products planned for the CDOP-2 are: total OCIO, tropospheric ozone, BrO and glyoxal, and climate products for NO<sub>2</sub> and water vapour. The main developments within the O3M-SAF project in 2013 are described below.

##### **Operational trace gas column products from GOME-2 on MetOp-B**

In June 2013, an Operational Readiness Review (ORR) of the GOME-2 trace gas column products for MetOp-B was carried out successfully. The operational dissemination of total ozone, total and tropospheric NO<sub>2</sub>, SO<sub>2</sub>, BrO, formaldehyde and water vapour column products from GOME-2B started in July 2013. The retrieval is carried out with the GDP 4.7, which includes improvements in the total ozone, SO<sub>2</sub>, BrO and water vapour columns algorithms (see below and chapter 3.2). On a global scale, GOME-2B has the same high accuracy as the corresponding GOME-2A products, and generally there is a very good agreement between the trace gas column products from the two sensors. Since July 2013, the GOME-2 instruments are operated in tandem mode. GOME-2A operates on a reduced swath width of 960 km with an increased spatial resolution of approx. 40 × 40 km<sup>2</sup> while GOME-2B operates on a nominal wide swath at 1920 km. This implementation increases both the daily coverage and the spatial resolution of GOME-2 measurements.

##### **Total O<sub>3</sub> product**

With the GDP 4.7, algorithm improvements were introduced in the total ozone retrieval for the GOME-2 instruments on MetOp-A and MetOp-B, including the use of the Brion-Daumont-Maliget (BDM) ozone absorption cross sections and an empirical correction to minimize the instrument scan angle dependency in the total ozone columns. The consistency between GOME-2A and GOME-2B has been investigated using DOAS fit residuals and the retrieved total ozone columns. The GOME-2B ozone fit residuals are much smaller than those of GOME-2A in 2013, but about 40% higher than those of GOME-2A in the early 2007 at the beginning of MetOp-A operations. This might be related to issues in the characterization of the GOME-2B slit function. On a global scale, GOME-2B is providing smaller total ozone columns by about 0.55±0.29% compared to GOME-2A. A first global validation for GOME-2B total ozone measurements, using Brewer and Dobson ground-based measurements shows an average difference of 1.5±3.7% between the GOME-2B and Dobson total ozone observations and 1.8±3.9% for the GOME-2A dataset.

Fig. 3-1 illustrates the total ozone column from GOME-2A and GOME-2B for 18 October 2013, as retrieved with the GDP 4.7 algorithm. This figure demonstrates the capacity of the GOME-2 instruments to provide homogeneous total ozone data with full daily global coverage, and shows important features such as the Antarctic ozone hole and characteristics of the polar vortex. The 2013 Antarctic ozone hole began to form in middle of August and the area of the ozone hole reached a maximum of 24.0×10<sup>6</sup> km<sup>2</sup>, which is larger than the ozone holes in 2012 and 2010, but less than in 2011 according to the World Meteorological Organization (WMO) Antarctic Ozone Bulletin. Fig. 3-2 shows the Antarctic ozone hole for 29 September and 16 October measured by GOME-2A and GOME-2B. The minimum total ozone columns recorded by GOME-2 on 29 September reached around 116 DU. One can see from Fig.

3-2 that the edge of the ozone hole briefly touched the southern tip of the South America continent and affected inhabited places such as Ushuaia and Río Gallegos on 16 October 2013.

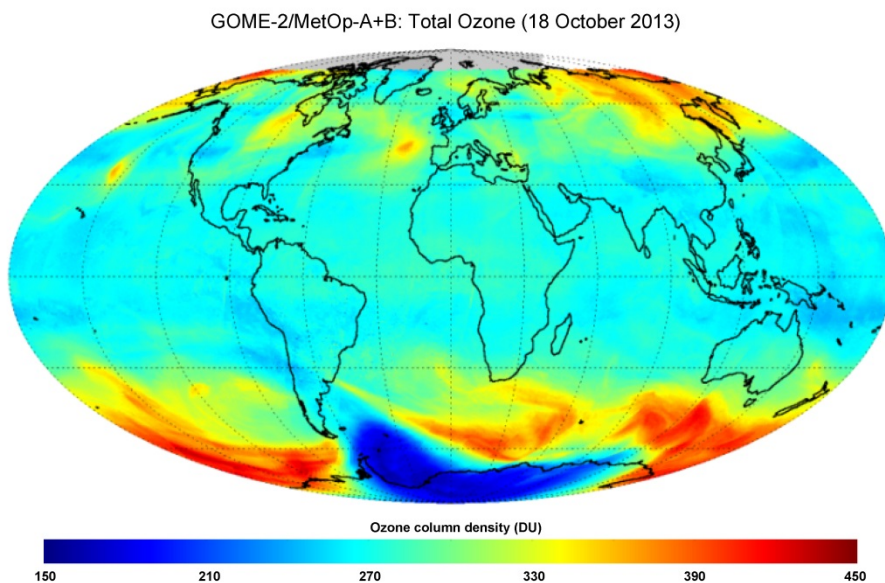


Fig. 3-1 Total ozone column retrieved from GOME-2A and GOME-2B on 18 October 2013.

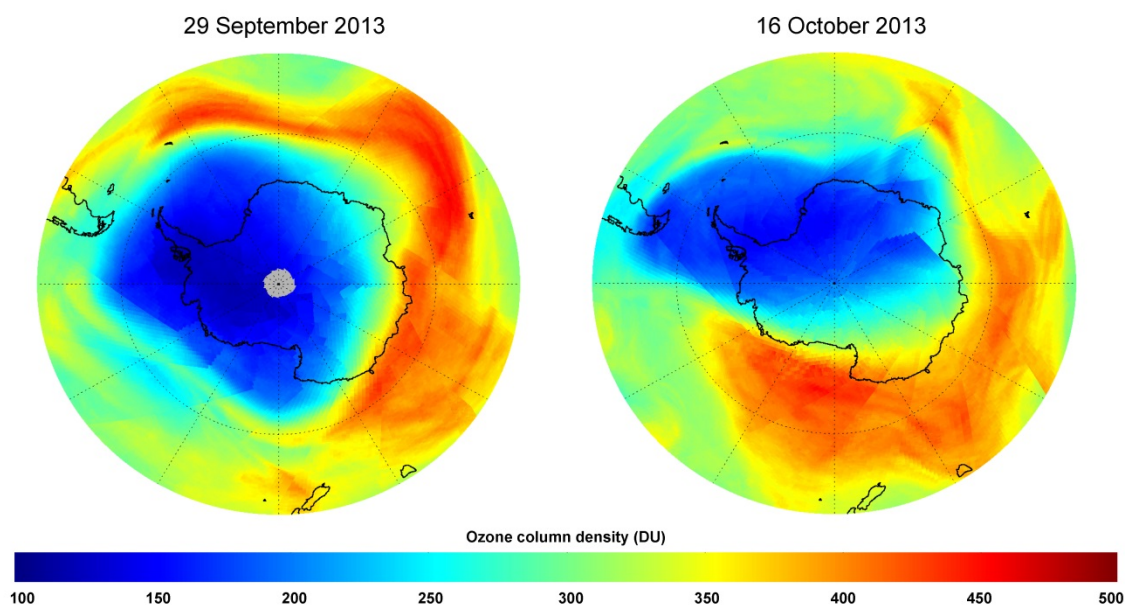


Fig. 3-2 Total ozone maps for 29 September and 16 October 2013 based on data from GOME-2A and GOME-2B.

### References

Hao N., Koukouli M.E., Inness A., Valks P., Loyola D., Zimmer W., Balis D.S., Zyrichidou I., Van Roozendaal M., Lerot C., Spurr R.J.D.: GOME-2 total ozone columns from MetOp-A/MetOp-B and assimilation in the MACC system, *Atmos. Meas. Tech.*, submitted, 2013.

Valks P., Loyola D., Hao N., Rix M., and Slijkhuis S.: Algorithm Theoretical Basis Document for GOME-2 Total Column Products of Ozone, Minor Trace Gases and Cloud Properties (GDP 4.7 for O3M-SAF OTO and NTO), DLR/GOME-2/ATBD/01, Iss./Rev.: 2/H, 2013.

### 3.2 Water Vapour Column Density Time Series from GOME, SCIAMACHY and GOME-2 Instruments

*M. Grossi, P. Valks, D. Loyola, S. Slijkhuis, B. Aberle, S. Beirle (MPIC), T. Wagner (MPIC), R. Lang (EUMETSAT)*

Water vapour is a key component of the Earth’s atmosphere. It plays a major role for both meteorological phenomena and climate via its influence on many physical and chemical processes including the formation of clouds and precipitation, the growth of aerosols and the depletion of the stratospheric ozone layer. Especially relevant to this study is the water vapour’s effect on the energy budget between incoming solar radiation and outgoing heat. As climate warms, the water vapour content in the atmosphere is expected to rise much faster than the total precipitation amount, thus further amplifying the original climate warming. However, it is still unclear what will be the net cooling (or warming) effect of clouds in a changing atmosphere, neither can we currently identify the contributions of natural and anthropogenic induced changes on the water vapour distribution.

Accurate satellite observations of the spatial and temporal variability of water vapour over an extended time period and on global scale are vital, as they may reveal changes in atmospheric dynamics resulting from climate change. We analyzed a long-term (since 1996) record of water vapour vertical distributions obtained from measurements of the GOME, SCIAMACHY and GOME-2 instruments and validated against both model data and independent satellite observations. With the launch of the new GOME-2/MetOp-C sensor in 2018, the GOME-type data record will be further extended to cover a period of at least 25 years of measurements. This unique data set has now reached high accuracy and stability and is expected to provide important information on long-term changes of our atmosphere.

#### **H<sub>2</sub>O total column**

The operational total column water vapour (TCWV) product is developed by us in the framework of EUMETSAT’s O3M-SAF in co-operation with MPIC Mainz, and generated by applying our GOME Data Processor (GDP) algorithm (*Valks et al. 2012*) consistently to GOME/ERS-2, SCIAMACHY/ENVISAT, GOME-2/MetOp-A (GOME-2A) and GOME-2/MetOp-B (GOME-2B) measurements. Table 3-1 summarizes the characteristics of the different GOME-type sensors. It is important to notice that differences in spatial and temporal sampling, in combination with cloud shielding, might determine a bias in the TCWV product derived from the different instruments.

Sensor Satellite	GOME ERS-2	SCIAMACHY ENVISAT	GOME-2 MetOp-A	GOME-2 MetOp-B
<b>Data period</b>	06/1995 - present	08/2002 – 04/2012	01/2007 - present	12/2012 - present
<b>Ground Pixel Size</b>	320 × 40 km <sup>2</sup>	60 × 30 km <sup>2</sup>	40 × 80/40 km <sup>2</sup>	40 × 80 km <sup>2</sup>
<b>Swath width</b>	960 km	960 km	1920/960 km	1920 km
<b>DNX time</b>	10:30 a.m. LT	10:00 a.m. LT	9:30 a.m. LT	9:30 a.m. LT

Table 3-1: Summary of GOME-type instrument characteristics.

The algorithm used for the retrieval of H<sub>2</sub>O Vertical Column Density (VCD) is based on classical Differential Optical Absorption Spectroscopy (DOAS) and employs a combined H<sub>2</sub>O/O<sub>2</sub> retrieval in order to compute the TCWV (*Wagner et al. 2003*). This procedure is robust – it provides similar sensitivity over land and ocean, very fast and, in contrast to other satellite retrieval methods, is independent from a priori assumptions on atmospheric properties, which makes this method especially suited for long-term climatology studies. In the newest version of the retrieval algorithm (GDP 4.7) the quality of the GOME-type H<sub>2</sub>O data has been further enhanced with respect to two major aspects. We investigated and improved the cloud selection criteria used to identify and flag cloudy pixels and we eliminated the dependency on the viewing angle conditions observed in the GOME-2A and GOME-2B measurements by consistently applying a distinct empirical correction for land and ocean surfaces (*Grossi et al. 2013a*).

In order to document the geophysical consistency of our H<sub>2</sub>O column data we collocated and compared TCWV estimates from GOME-type instruments with corresponding model data from the European

Centre for Medium Range Weather Forecast (ECMWF; *Dee et al. 2011*) and SSM/IS satellite F16 measurements (*Wentz 1997*) during the full period 1996-2013. We also performed a validation between the GOME-2A product and the combined SSM/I + MERIS GlobVapour data set in 2007 and 2008 (*Schroeder et al. 2012*). Within our analysis, we found a surprisingly good agreement between GOME-2 type instruments and the four independent data sets analyzed here, with a mean bias within  $\pm 0.035 \text{ g/cm}^2$  for the time interval January 2007 – August 2013 (*Grossi et al. 2013b*). The annual variability over land and coastal areas is low, but over ocean we observe a clear seasonal cycle with highest values during northern hemisphere (NH) summer. Slightly lower than in summer and negative biases are found in the NH winter months. These variations can mainly be related to the impact of clouds on the accuracy of the GOME-2 observations and to the different sampling statistics of the instruments.

Fig. 3-3 shows the mean distribution of TCWV data in August 2008 obtained from daily collocation of ECMWF and GOME-2A data. Overall, we find similar spatial patterns in the  $\text{H}_2\text{O}$  distributions as we can observe a high humidity in the tropics and a low humidity at high latitude. However, for this particular month we can also notice relative large differences between GOME-2A and ECMWF data in some specific regions. For example, the humidity over the Sahara desert is much lower in the GOME-2A data than expected in the ECMWF model data. Moreover, the negative bias in the region that goes from India till the east coast of China is associated to high surface albedo values (in the range 0.3-0.5) and a high TCWV. A possible explanation of the discrepancies is that, because of absorbing aerosols over deserts, the surface albedo we measure is lower than the real value and therefore we underestimate the water vapour content (*Fournier et al. 2006*). However, the determination of the “real” surface albedo over desert is still a field of discussion because of the uplifting of large amounts of dust, which lowers the reflectivity (*Torres et al. 1998*).

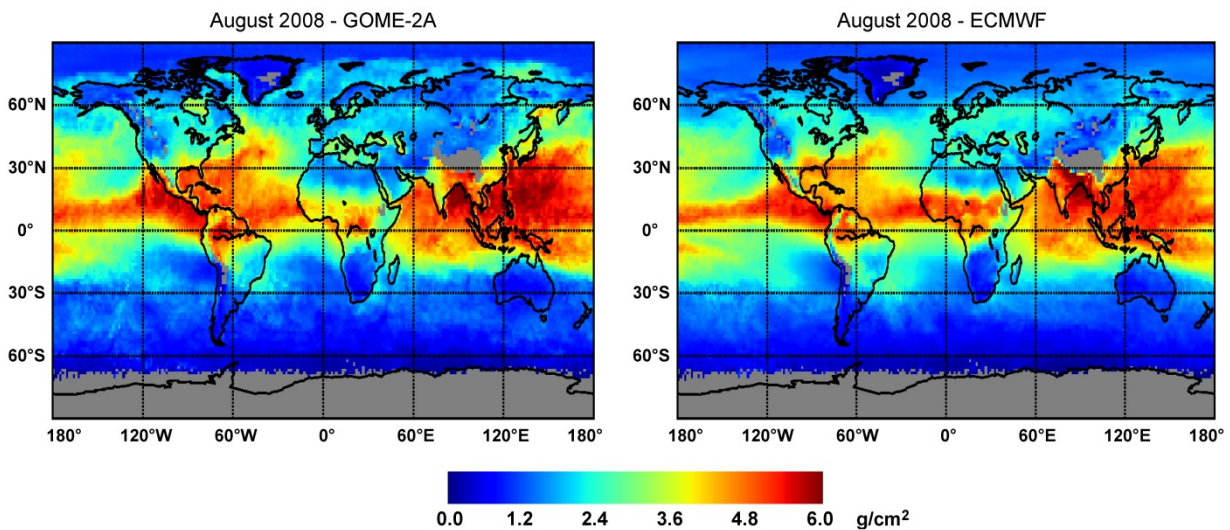


Fig. 3-3: Monthly mean maps of TCWV from GOME-2A (left) and ECMWF (right) co-located data for August 2008. Only cloud-screened data have been used.

### **H<sub>2</sub>O time series**

In Fig. 3-4 we display a time series of globally averaged  $\text{H}_2\text{O}$  vertical column monthly mean values based on the GOME, SCIAMACHY and GOME-2A datasets, covering the period January 1996 – August 2013. The TCWV distribution follows the seasonal cycle of the near surface air temperatures: it exhibits a minimum during the northern hemispheric winter and a maximum in the summer months. To assure the consistency between the results from the three sensors, we followed the method described in *Schroeder et al. (2012)* for the harmonization of the time series. In the first step, the offset between GOME-2A and SCIAMACHY TCWV is determined in the overlapping period January 2007 – December 2007 and added to all SCIAMACHY data in order to achieve consistency with the GOME-2 time series. In a second step, we selected the period August 2002 – June 2003 and computed the offset between the SCIAMACHY corrected data and the GOME results. This method allowed us to correct for systematic differences between the three sensors, like discrepancies in overpass time, spectral resolution and

ground pixel size. In particular, the different resolution of the instruments together with the cloud cover is the most important contributor to the level shift.

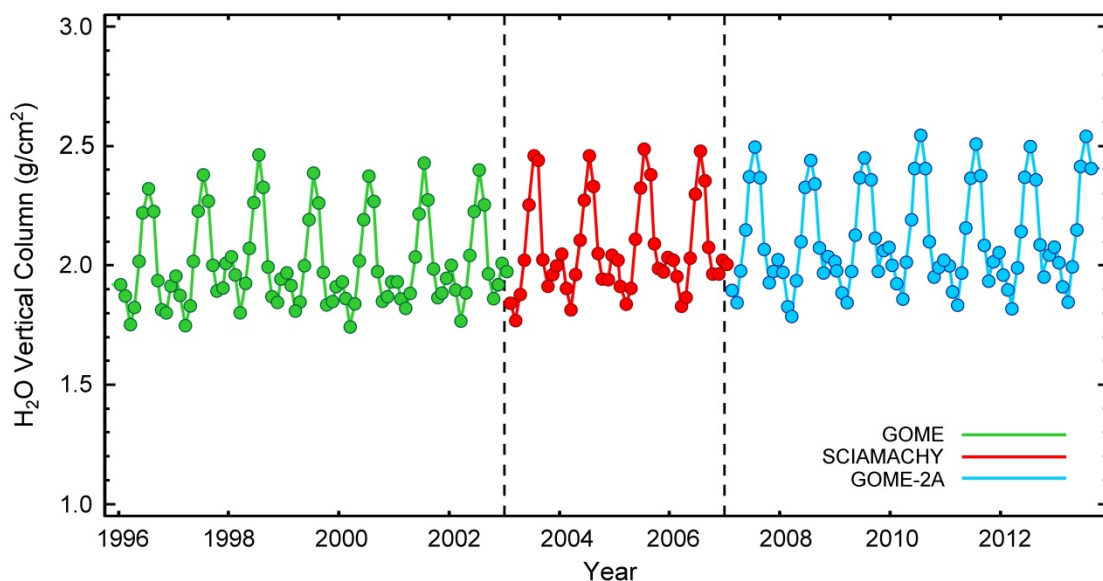


Fig. 3-4: Global monthly mean TCWV values for the merged data set including GOME-2A data (blue), as well as adjusted SCIAMACHY (red) and GOME (green) measurements.

We removed the seasonal cycle from the globally averaged monthly mean results in order to compute the anomaly time series and the spatial distribution of  $H_2O$  global trends. Performing a regression analysis on the GOME-2A data record we found that the TCWV increases at a rate of  $0.0052 \text{ g/cm}^2$  per year (see left panel of Fig. 3-5). However, trends can be influenced by several kinds of effects, such as instrumental changes or natural phenomena. The largest La Niña / El Niño events during the past 6 years are clearly evident as a minimum and a peak in the anomaly time series occurring during 2007-2008 and 2009-2010, respectively.

Even if the length of the GOME-2 data is insufficient to resolve long-term oscillations in the water vapour amount, it can be useful to point out significant  $H_2O$  changes in several regions on Earth. A map of the spatial distribution of the trends in the GOME-2A data set is shown in the right panel of Fig. 3-5. The most striking feature is the upward trend in the equatorial Pacific, very suggestive of the El Niño influences, and in the western coast of Australia (as observed in *Wagner et al. 2006, Mieruch et al. 2008*). An interesting region with decreasing TCWV is the Amazon basin. Currently, about 15% of the Brazilian Amazon region has been deforested and converted to agricultural uses, with a concomitant decrease in water vapour flows which is in line with our observed trends (*Gordon et al. 2005*).

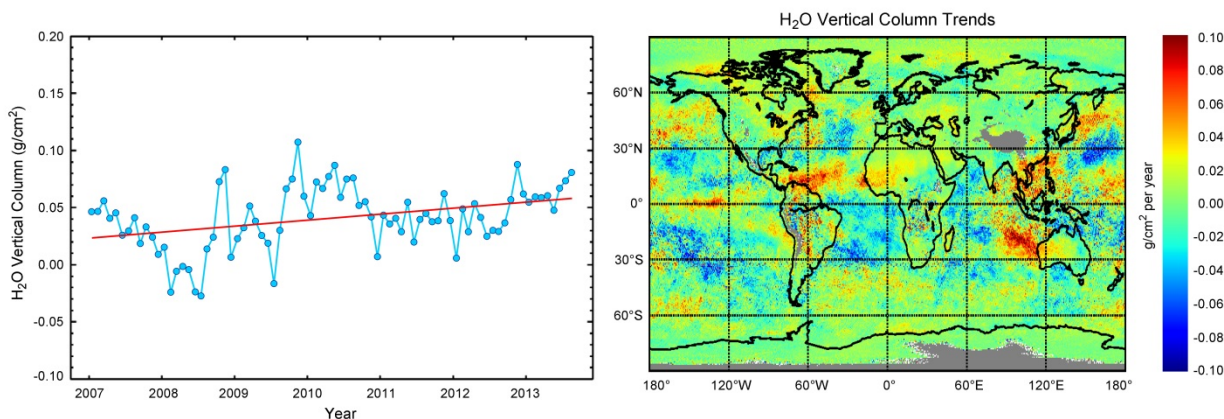


Fig. 3-5: Time series of de-seasonalized monthly mean TCWV (left panel) and global absolute  $H_2O$  vertical column trends (right panel) derived from GOME-2A measurements over the period January 2007 – July 2013.

### References:

- Dee D.P., Uppala S.M. Simmons A.J. Berrisford P., Poli P., et al.: The ERA-Interim reanalysis: Configuration and performance of the data assimilation system, *Quart. J. Roy. Meteor. Soc.*, 137, 553-597, 2011.
- Fournier, N., Stammes P., de Graaf M., van der A R., Piters A., Grzegorski M., Kokhanovsky A.: Improving cloud information over deserts from SCIAMACHY O2 A-band, *Atmos. Chem. Phys.*, 6, 163–172, 2006.
- Gordon L.J., Steffen W., Jönsson B.F., Folke C., Falkenmark M., Johannessen Å.: Human modification of global water flows from the land surfaces, *PNAS* 102, 7612-7617, 2005.
- Grossi M., Kalakovski N., Valks P.: O3M SAF ORR Validation Report, 15 SAF/O3M/DLR/ORR/H2O, Issue 01/2013, 2013a.
- Grossi M., Valks P., Loyola D., Aberle B., Slijkhuis S., Wagner T., Beirle S., Lang R.: Total Column Water Vapour measurements from GOME-2 MetOp-A and MetOp-B, AMT-2013-330, accepted, 2013b.
- Mieruch S., Noël S., Bovensmann H., and Burrows J.P.: Analysis of global water vapour trends from satellite measurements in the visible spectral range, *Atmos. Chem. Phys.*, 8, 491-504, 2008.
- Schroeder M., Slijkhuis S., Wagner T.: DUE GLOBVAPOUR Algorithm Theoretical Baseline Document (ATBD) for L3 GOME+SCIAMACHY+GOME-2, Issue 3, Revision 0, 19 January 2012.
- Torres O., Bhartia P.K., Herman J.R., Ahmad Z., and Gleason J.F.: Derivation of aerosol properties from satellite measurements of backscattered ultraviolet radiation: Theoretical basis, *J. Geophys. Res.*, 103, 17099-17110, 1998.
- Valks P., Loyola D., Hao N., Rix M., Slijkhuis, S.: Algorithm Theoretical Basis Document for GOME-2 Total Column Products of Ozone, Minor Trace Gases and Cloud Properties (GDP 4.5 for O3M-SAF 15 OTO and NTO), DLR/GOME-2/ATBD/01, Iss./Rev.: 2/GG, 2012.
- Wagner T., Heland J., Zöger M., and Platt U.: A fast H2O total column density product from GOME – Validation with in-situ aircraft measurements, *Atmos. Chem. Phys.*, 3, 651–663, 2003.
- Wagner T., Beirle S., Grzegorski M., and Platt U.: Global trends (1996–2003) of total column precipitable water observed by Global Ozone Monitoring Experiment (GOME) on ERS-2 and their relation to near-surface temperature, *J. Geophys. Res.* 111, D12102, doi:10.1029/2005JD006523, 2006.
- Wentz F.J.: A well-calibrated ocean algorithm for SSM/I, *J. Geophys. Res.* 102, C4, 8703-8718, 1997.

### 3.3 The Sentinel 5 Precursor Mission

*D. Loyola, B. Aberle, N. Hao, P. Valks, R. Lutz, S. Gimeno García, P. Hedelt, M. Pedernana, W. Zimmer, H. Bauer*

The Sentinel 5 Precursor (S5P) mission is an integral part of the space component of the European Copernicus initiative. Together with Sentinel 4 (S4) and 5 (S5) it contributes to retrieving knowledge about the state of the Earth's atmosphere during the next decades. S5P carries the absorption spectrometer TROPOMI, the Tropospheric Ozone Monitoring Instrument, which is a joint development of The Netherlands and ESA. TROPOMI covers spectral bands in the ultraviolet (UV), the visible (VIS), the near-infrared (NIR) and the shortwave infrared (SWIR) with an excellent spatial resolution ( $7 \times 7 \text{ km}^2$  at nadir) and a daily global coverage (swath width 2600 km). The launch of S5P is planned for September 2015. We are involved in two parts of two complementary S5P projects: the Payload Data Ground Segment (S5P PDGS) and the level 2 (S5P L2).

#### **S5P PDGS**

The German Remote Sensing Data Center (DFD) is responsible for S5P data processing (level 0-1-2), archiving and product dissemination together with the corresponding quality monitoring tasks. As part of this, we are responsible for developing the product quality monitoring (PQM) for S5P level 0 and level 1 products. Documentation for project management, requirements and architectural design have been prepared. The purpose of the PQM is to check products routinely in the near-realtime operational processing chains. To ensure the generation of quality reports for each product on an operational basis, the PQM has to be integrated into the S5P PDGS. The output of the PQM system should give valuable hints on all kinds of possible issues and effects affecting the quality of the S5P level 0 and level 1 products.

#### **S5P L2**

Here the goal is the development of the operational S5P level 2 products. Funding is provided via complementary ESA contracts, Bayern grants, and DLR internal financing. All development, verification, testing, operational and management tasks are organized in line with three core activities with the overall coordination being shared between three institutes (see Table 3-2).

Product / Processor Component	Development		Operational Processor DLR-MF
	Algorithm Prototyping KNMI	Independent Verification IUP-IFE	
<b>Mandatory Products</b>			
O <sub>3</sub> total column	DLR-MF, BIRA	KNMI	DLR-MF
O <sub>3</sub> profiles (incl. troposphere)	KNMI	RAL, IUP-IFE	KNMI
O <sub>3</sub> tropospheric column	IUP-IFE, DLR-MF	KNMI	DLR-MF
NO <sub>2</sub> total & tropospheric column	KNMI	IUP-IFE, DLR-MF, MPIC	KNMI
SO <sub>2</sub>	BIRA	MPIC, DLR-MF	DLR-MF
HCHO	BIRA	IUP-IFE	DLR-MF
CO	SRON	IUP-IFE	KNMI
CH <sub>4</sub>	SRON	IUP-IFE	KNMI
Clouds	DLR-MF	KNMI, MPIC, IUP-IFE	DLR-MF
Aerosols	KNMI	MPIC, IUP-IFE	KNMI
<b>External Auxiliary Data</b>			
Cloud data from NPP	RAL	n.a.	RAL

Table 3-2: Sentinel 5 Precursor level 1-2 development responsibilities.

#### ***Algorithm Prototyping***

A first version of the algorithm theoretical baseline documents (ATBD) for O<sub>3</sub> total column, O<sub>3</sub> tropospheric column and clouds was successfully reviewed by ESA and external experts in August 2013.

- **$O_3$  total column:** Two algorithms will be used for the generation of S5P total ozone products: DOAS for the near-realtime products and GODFIT for the offline products. Due to the high data rate of TROPOMI, on-line AMF calculation with LIDORT is a big issue even using the fast DOAS algorithm. Therefore, we are investigating the usage of look-up tables (LUT) for AMF calculations. Our method is based on the application of the 2STREAM (2S) model for the approximation of multiple-scatter field and "First-Order" (FO) model originally developed for the acceleration of the LIDORT code. The 2S model is a factor 3-4 faster than LIDORT with 4 discrete ordinates as used operationally for GOME-2. The full LIDORT AMFs are compared with AMFs generated from 2S+FO models to provide AMF correction factors. The AMF correction factors are stored in a LUT as a function of total ozone columns, solar zenith angle ( $\theta_0$ ), viewing zenith angle ( $\theta$ ), relative azimuth angle ( $\varphi-\varphi_0$ ), Lambertian surface albedo ( $A_s$ ), and surface pressure ( $p_s$ ). Figure 3-6 shows the accuracy of the 2S+FO calculation of total ozone AMFs compared to AMFs calculated from full LIDORT as a function of the surface albedo. This new acceleration method leads to time savings of factor 2-3 (depending on the size of LUT) for total ozone AMFs calculation, while maintaining excellent accuracy.

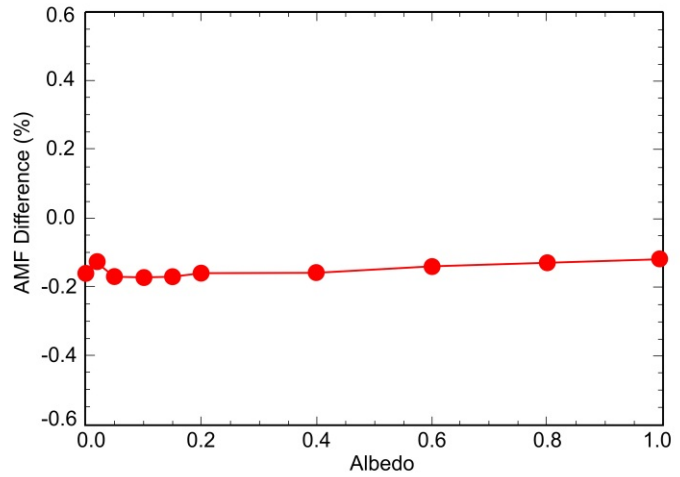


Fig. 3-6.: Accuracy of fast AMF calculation from 2S+FO model against surface albedo ( $\theta_0=50$ ,  $\theta=30$ ,  $\varphi-\varphi_0=75$ ,  $p_s=1021$ hPa and total ozone column 300 DU).

- **$O_3$  tropospheric column:** The retrieval of tropospheric ozone columns from S5P measurements for the tropical region is based on the convective-cloud-differential (CCD) method, and uses cloud and total ozone data provided by the operational S5P L1-to-2 processors. With the S5P/CCD method, weekly and monthly mean tropospheric ozone columns are derived from above-cloud and clear-sky ozone column measurements for the tropical region between 20°N and 20°S. The tropospheric ozone processing for S5P is based on the operational systems used for GOME/ERS-2 and GOME-2/MetOp-A and -B. Thus it extends the long-term record of tropospheric ozone data produced by a reliable, well-established and well-described processing system. Fig 3-7 shows a recent example of the tropospheric ozone columns retrieved with the GOME-2 instrument onboard MetOp-B.

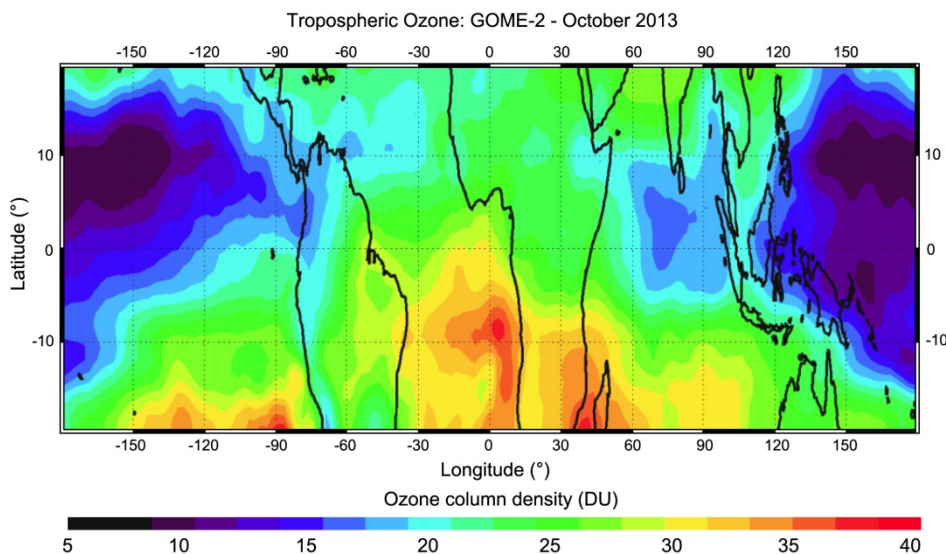


Fig. 3-7: Tropospheric ozone columns as measured by GOME-2/MetOp-B for October 2013.

- Clouds:** The OCRA and ROCINN algorithms will be used for generating the S5P cloud products – cloud fraction, cloud-top height and cloud optical thickness. OCRA computes the cloud fraction taking as input the PMD measurements from GOME-type sensors. TROPOMI does not provide polarization measurements and therefore OCRA is being adapted to work with radiances. Figure 3-8 shows the cloud fractions derived from radiances from the Ozone Monitoring Instrument (OMI) on-board the EOS-Aura satellite for 15 January 2005. The results of OCRA and the two official OMI cloud products are shown. Grey regions indicate unavailable data and the large differences between OMCLDRR and the other two products at high northern and southern latitudes arise from snow/ice flags, for which the cloud fraction in the bottom panel is set to 1.0. ROCINN retrieves cloud optical thickness and the cloud-top height from reflectances in and around the O<sub>2</sub> A-band. Unlike earlier versions of ROCINN, which were based on the treatment of clouds as reflecting surfaces (CRB), the S5P algorithm is based on a more realistic cloud modeled as scattering layers (CAL). Figure 3-9 illustrates that the cloud-top height is systematically underestimated using the CRB model, discrepancies increase as cloud optical depth decreases. This shows that the CRB cloud model may not be appropriate for TROPOMI with a resolution of 7 × 7 km<sup>2</sup>.

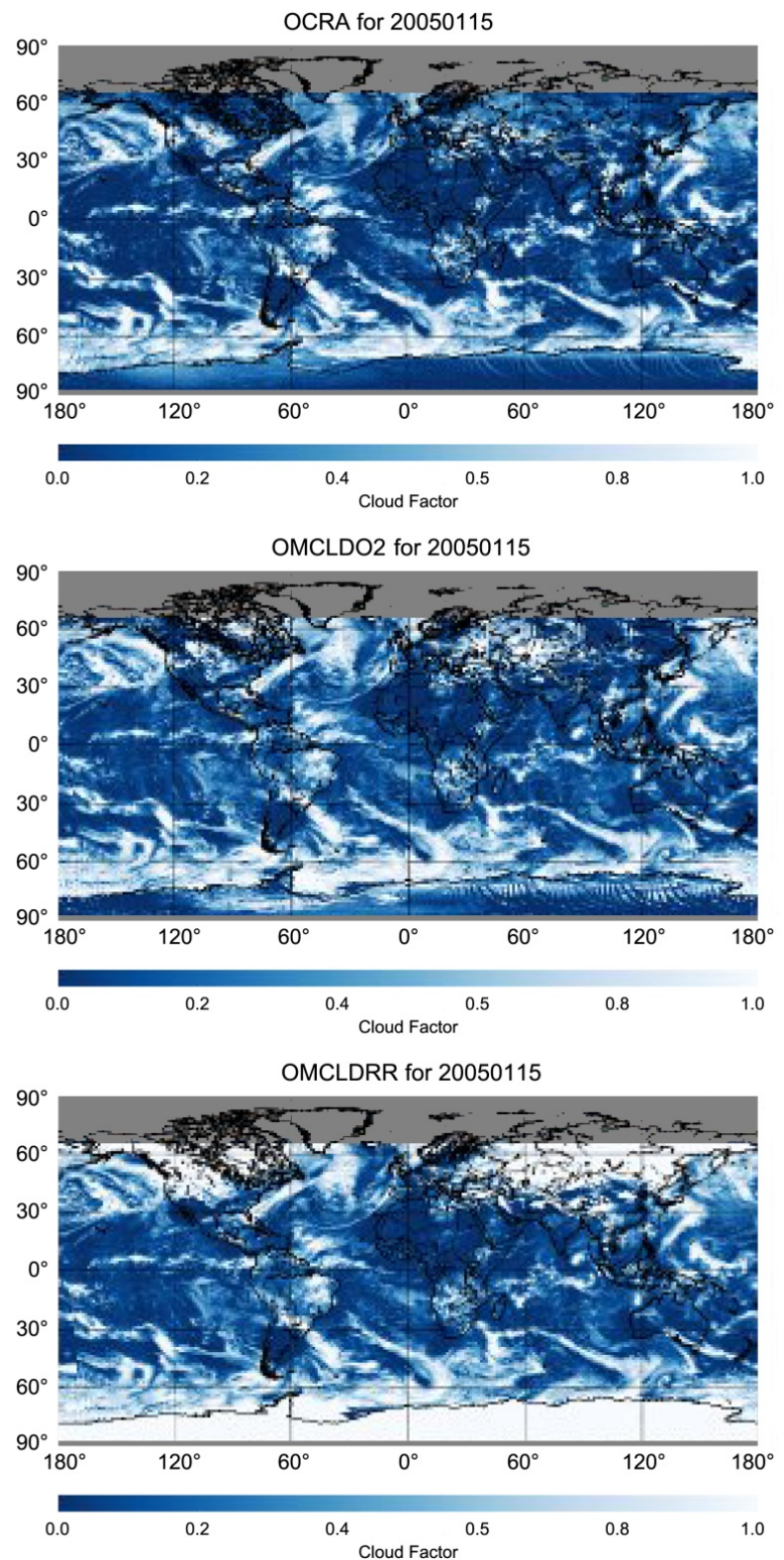


Fig. 3-8: Cloud fraction from the OMI sensor derived with OCRA (top), the official OMI cloud products based on O<sub>2</sub>-O<sub>2</sub> absorption (OMCLDO2, mid) and based on Raman scattering (OMCLDRR, bottom).

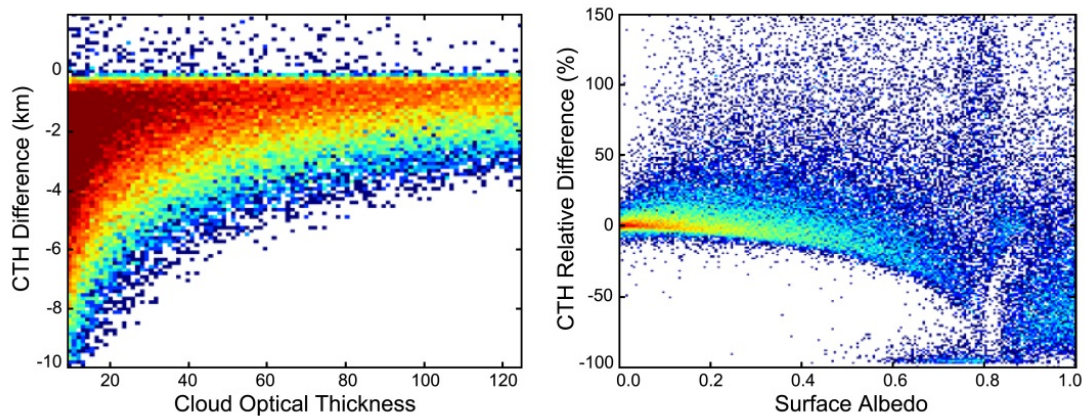


Fig. 3-9: Differences in the cloud-top height retrieved using the CAL and CRB model as function of the cloud optical thickness (left). Cloud-top height error induced by using the CRB model with a fixed cloud albedo of 0.8 (right), errors depend not only on the actual cloud albedo but also on the surface albedo.

### Independent Verification

We are also involved in the verification of the S5P prototype algorithms for NO<sub>2</sub> and SO<sub>2</sub>.

- **NO<sub>2</sub>**: The retrieval of NO<sub>2</sub> total columns can be separated in different parts – the tropospheric NO<sub>2</sub> column and the stratospheric NO<sub>2</sub> column. The total column is then the sum of the two. However, the different quantities are interlinked with each other, and errors in the stratospheric column will lead to errors in the tropospheric and total columns. For the verification, three independent retrievals will be used to evaluate the different aspects of the product (stratospheric, tropospheric and total NO<sub>2</sub> column), which provides additional cross-check opportunities of the S5P prototype NO<sub>2</sub> product. The NO<sub>2</sub> verification activities at IMF will focus on the total NO<sub>2</sub> column retrieval.
- **SO<sub>2</sub>**: The verification of SO<sub>2</sub> slant column will be performed at MPIC using a DOAS fit in the wavelength range from 312-324 nm. For elevated SO<sub>2</sub> columns an alternative fitting window from 326-335 nm will be used. The conversion to total vertical column will be performed by us in two different ways: A priori AMFs for predefined volcanic plume heights will be calculated using LIDORT and stored in the form of a look-up table. This approach is currently also used for the operational GOME-2 SO<sub>2</sub> retrieval and was found to work efficiently for low SO<sub>2</sub> total columns. However, for elevated columns > 30 DU SO<sub>2</sub> this approach underestimates the total vertical column since for the AMF calculation a total SO<sub>2</sub> column of 3 DU was assumed. A new approach is currently under investigation. For this approach, spectra are simulated using LIDORT LRRS for a set of known total vertical SO<sub>2</sub> columns. These spectra are then fitted with the same DOAS retrieval settings as for the operational measurement. In this way the dependency of the slant column on the assumed vertical SO<sub>2</sub> column is resolved and the measured slant column can be interpolated to obtain directly the corresponding total column. A set of volcanic eruptions measured by GOME-2 is currently re-investigated using this approach. First preliminary results already provide much higher total columns, as expected.

### Operational Processor UPAS

Two UPAS versions were delivered during 2013 covering all the external interfaces of the system as identified in Figure 3-10. This high-level chart shows the input (green) and output (orange) of the whole system. This includes the thin layer interface with the PDGS side as well. It is worth noting that UPAS produces five S5P level 2 products: L2 Clouds, L2 Ozone Total Column, L2 SO<sub>2</sub>, L2 HCHO and L2c Ozone Tropospheric. The center of the Fig. 3-10 hosts the processor itself operating in three different modes: near-realtime (NRT), offline (OFL) and reprocessing (REP). Regarding the NRT processing, the L2 NRT products are derived from the L1b NRT products. A pipeline strategy processing is implemented in order to speed up the processing system. The level 0 product is divided in small data units which are sent in the processing and disseminating chain: in this way the level 0, level 1 and level 2 processors can start to work in parallel maximizing the efficiency of the process.

Concerning the OFL mode, the processor generates level 2 OFL product based on the consolidated level 1b orbit products. Finally, the reprocessing mode works in the same manner as the OFL mode, but it

affects the whole data available since the S5P mission had started. The purpose of this task is to reprocess all the acquired orbits with the more updated version of the S5P UPAS processor, level 1b products and auxiliary data. The REP mode is designed with the aim of maximizing the total throughput. Due to the high complexity of the architecture, the system itself is subdivided in three sub-processors which belong to the main framework of UPAS.

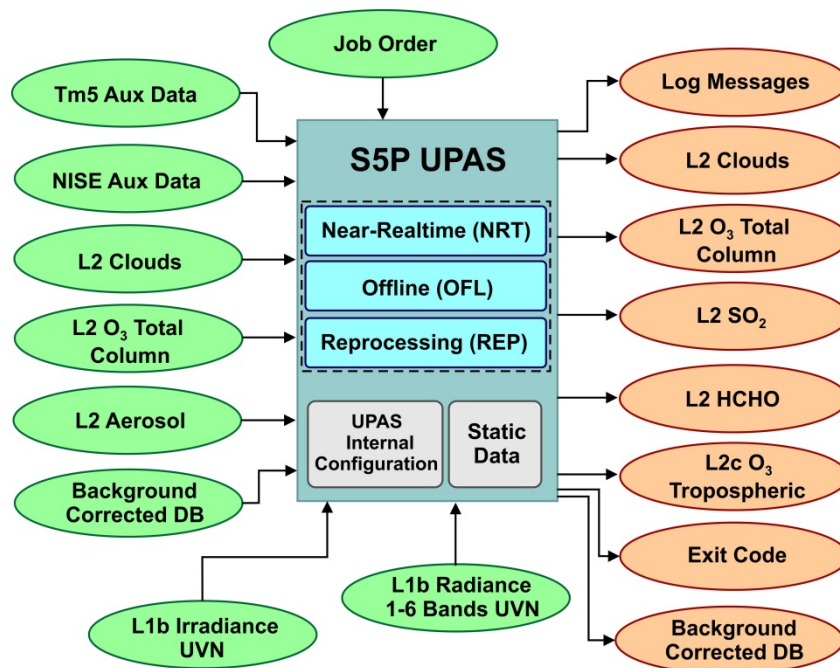


Fig. 3-10: S5P UPAS external interfaces, inputs are in green and outputs in orange.

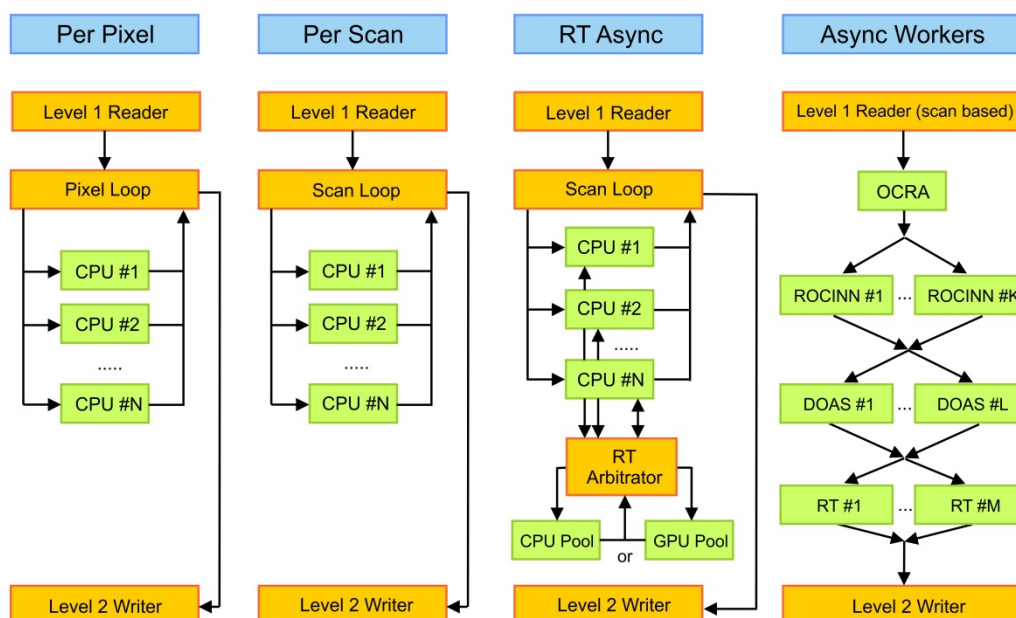


Fig. 3-11: Parallelization scenarios considered for UPAS.

The TROPOMI sensor will provide two orders of magnitude more data than GOME-2 with around 260 measurements per second. Therefore different UPAS parallelization scenarios for the optimal processing of S5P data were analysed. Figure 3-11 shows the four scenarios considered: the leftmost is an augmentation of the current operational processor which processes one pixel at a time. By distributing

these pixel processing workloads to different CPU cores, the multicore capabilities of modern CPUs can be exploited. The second scenario goes one step further: it does not process individual pixels, but all pixels of a complete scan. This provides the possibility for algorithms to consider the properties of the neighbouring pixels without the need to communicate between different threads. Further, it also allows operations to be vectorized over the scan pixel dimension which can be greatly beneficial for performance. The third scenario allows the use of core pools specialized on specific task, e.g. radiative transfer. Each thread would process one scan as in scenario 2, but for that specialized task, it offloads the workload to the pool of specialized worker threads. This scenario allows the inclusion of dedicated computing cores (APU, GPU, MIC) into the processing. In the fourth (rightmost) scenario, each CPU core only runs one specific sub-algorithm, and then forwards the data to another core running the next algorithm in line. This is, from performance side, the optimal configuration, as each core only needs to have the data required for the sub-algorithm in its cache. On the other hand, the impact on program structure and the stability requirements to the asynchronous framework make this scenario much more demanding. Amongst those scenarios, scenario 2 was chosen for the first implementation of the S5P UPAS framework, being confident that it can provide the performance required. In a second step, the processor can then be migrated to scenario 3 for the inclusion of dedicated computing cores to make use of additional computing capabilities.

In addition to the performance considerations, it turns out that modularity is the most important design criteria for the S5P UPAS code. Only when the code is modular enough for modules to be rearranged easily, new requirements can be met with acceptable effort. This is especially helpful in the code optimization phase, where modules might be rearranged to maximize performance.

One of the main retrieval tasks of the UPAS processor is to perform DOAS fits for the computation of trace gas slant columns. Therefore it is of vital importance to optimize the DOAS module to run in parallel on a multi-thread environment. The mock-up version delivered to ESA in December 2013 is already able to run a multi-threaded DOAS fit taking as input GOME-2 level 1 products. Further performance optimizations and other DOAS improvements are ongoing.

### 3.4 Carbon Monoxide Retrievals from Shortwave Infrared Observations of SCIAMACHY

*F. Schreier, S. Gimeno García, G. Lichtenberg, M. Hess*

Remote sensing of atmospheric trace gas concentrations by downlooking space-borne infrared spectroscopy is well established. Nadir spectra observed in the shortwave infrared (SWIR) are especially sensitive to the lower atmosphere. These spectra provide information about greenhouse gases (carbon dioxide – CO<sub>2</sub>, methane – CH<sub>4</sub>, or water vapour – H<sub>2</sub>O) or gases with radiative forcing such as carbon monoxide (CO) and are therefore useful for source and sink analysis.

Three of SCIAMACHY's eight science channels covered the SWIR range, where CH<sub>4</sub> and CO<sub>2</sub> retrievals use channel 6 data while CO retrievals are subject to channel 8. For the analysis of SWIR nadir observations delivered by SCIAMACHY or similar instruments we had developed BIRRA, the Beer InfraRed Retrieval Algorithm. BIRRA performs a least squares fitting of vertical column densities and auxiliary parameters from the radiance spectra, where a separable least squares is utilized to exploit the special structure of the forward model. The forward model, i.e. radiative transfer model, is based on GARLIC, the Generic Atmospheric Radiation Line-by-line IR Code (see chapter 3.9). Analysis of SCIAMACHY's channel 8 spectra is especially challenging. Due to its weak absorption, CO gives only an extremely small signal. Moreover, the retrievals are made even more difficult by an ice layer on the detector, an increasing number of bad or dead pixels, and an imperfect wavelength calibration. Accordingly, a recent upgrade of the BIRRA code has been implemented that allows fitting a wavelength shift as an additional auxiliary parameter. Furthermore, the option to use a Voigt-type slit function is offered.

Fig. 3-12 shows carbon monoxide annual averages as delivered with the most recent BIRRA version. The retrievals were performed with fully calibrated spectra, normalized by SCIAMACHY sun measured spectra. As in previous retrievals, the spectral window 4283-4302 cm<sup>-1</sup> has been considered. The state vector to be fitted was comprised of scaling factors for the three active gases CO, CH<sub>4</sub>, and H<sub>2</sub>O, a

second degree reflectivity polynomial, the half width of the Gaussian slit function (accounting for the unknown ice layer), and the wavelength shift. The graphs confirm the high quality of the CO product in the first three years of the mission. The remaining years have less valuable data, but the retrieval code upgrade still allowed to derive some CO information. In particular, fitting the wavelength shift lead to a significant improvement, that even allowed CO retrievals for the very last years. Note that due to the additional fit of the wavelength shift the number of retrievals passing the quality flags has been significantly increased. In conclusion we expect that further efforts in level 1 data along with refinements in the retrieval code could improve the overall quality of the carbon monoxide product.

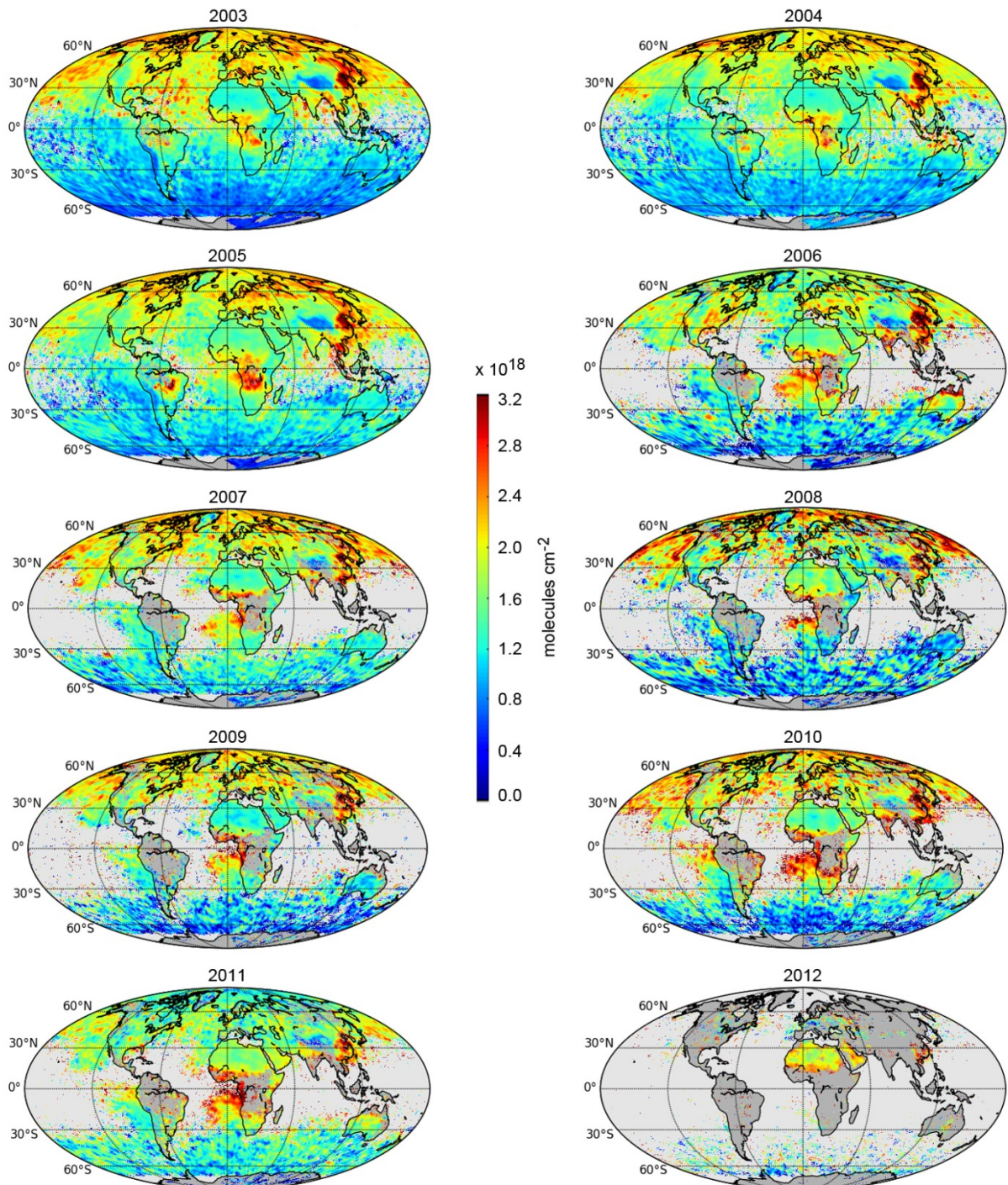


Fig. 3-12: Annual average of carbon monoxide vertical column density from 2003 (top left) to 2012 (bottom right). Note that the 2012 CO global distribution covers only the first three months till the end of the mission in April 2012.

### 3.5 Retrieval of Stratospheric HCl in Activated Arctic Air from TELIS Far-Infrared Data

*J. Xu, F. Schreier, T. Trautmann, P. Vogt (MF-EXV), M. Birk (MF-EXV), G. Wagner (MF-EXV)*

TELIS (Terahertz and Submillimeter Limb Sounder) is a balloon-borne cryogenic heterodyne spectrometer. It was designed to monitor the vertical distribution of stratospheric constituents associated with ozone depletion and climate change. The instrument employs two 1.8 THz (far-infrared) and 480-650 GHz microwave channels and monitors the vertical distribution of stratospheric species over an altitude range of 10-32.5 km with 1.5-2 km sampling. Three scientific campaigns took place in Kiruna, Sweden in the winters of 2009-2011. Here we present the hydrogen chloride (HCl) retrieval of the 2010 data as the flight occurred in the Arctic polar vortex that was fully chlorine activated.

The employed retrieval code PILS (Profile Inversion for Limb Sounding) comprises a line-by-line forward model built on GARLIC (Generic Atmospheric Radiation Line-by-line Infrared Code) and a nonlinear least squares framework coupled with adaptive multi-parameter regularization methods. We used the iteratively regularized Gauss-Newton method and the regularized iterative solution is given by (see *Xu et al. 2013*)

$$x_{i+1} = x_a + (K_i^T K_i + \lambda_i L^T L)^{-1} K_i^T (y - F(x_i) + K_i(x_i - x_a))$$

In this case, the regularization parameter is defined as a decreasing sequence and the number of iteration steps is determined by the stopping criterion

$$\|F(x_{i^*}) - y^\delta\|^2 \leq \chi \|r^\delta\|^2 < \|F(x_i) - y^\delta\|^2 \quad \text{with } 0 \leq i < i^*$$

where  $\chi > 1$  and  $\|r^\delta\|$  is the residual vector at the last iteration step.

HCl is one of the most important molecules measured by both THz and GHz channels of the TELIS instrument. In the case of the 1.8 THz channel, one  $\text{H}^{37}\text{Cl}$  line at the transition frequency of 1873.40 GHz ( $62.49 \text{ cm}^{-1}$ ) is observed. For the 2010 flight, the tangent heights range from 10 or 16 km to 32.5 km discretized in 1.5 km. In addition to the target molecule and the instrument baseline offset, a "greybody" profile was taken into account in order to account for the broad continuum-like contributions at lower altitudes that cannot be accurately depicted by current continuum models. Furthermore, the radiometric calibration procedure has to be modeled in the forward model at each iteration and the cold spectrum was simulated with one up-looking spectrum with zenith angle of  $25^\circ$ . Uncertainties in the potential error sources were identified in the TELIS consortium and have been considered in an error analysis.

In Fig. 3-13, the HCl profile retrieved from the far-infrared data is firstly compared to that from the microwave data (provided by the SRON team). Because the signal detected by the THz channel is rather strong compared to that in the GHz channel, the uncertainty of the nonlinearity effect is estimated to contribute more to the error budget, especially above 30 km. Different a priori profiles lead to the discrepancy between the two retrievals below 23 km, as the information loss at lower altitudes is due to regularization. For an external comparison, two SMILES and one MLS profiles were taken in terms of close geolocation and measuring time. A good agreement is found above 23 km and the SMILES and the MLS profiles fall well within the accuracy range of the TELIS retrieval. As Fig. 3-13 and Fig. 3-14 illustrate, the full depletion of HCl around 23 km was observed by both TELIS and the two spaceborne instruments, HCl was converted into active chlorine species, e.g. ClO.

First retrieval results of HCl from TELIS's far infrared observations have been successfully validated against the profile by other sensors. The differences at lower altitudes stem from the regularization effect, and the overall accuracy at higher altitudes is mainly determined by the nonlinearity effect in the calibration procedure. TELIS provides a better vertical resolution than that of space-borne instruments, and thus, future comparisons will take into account a convolution of the corresponding averaging kernels.

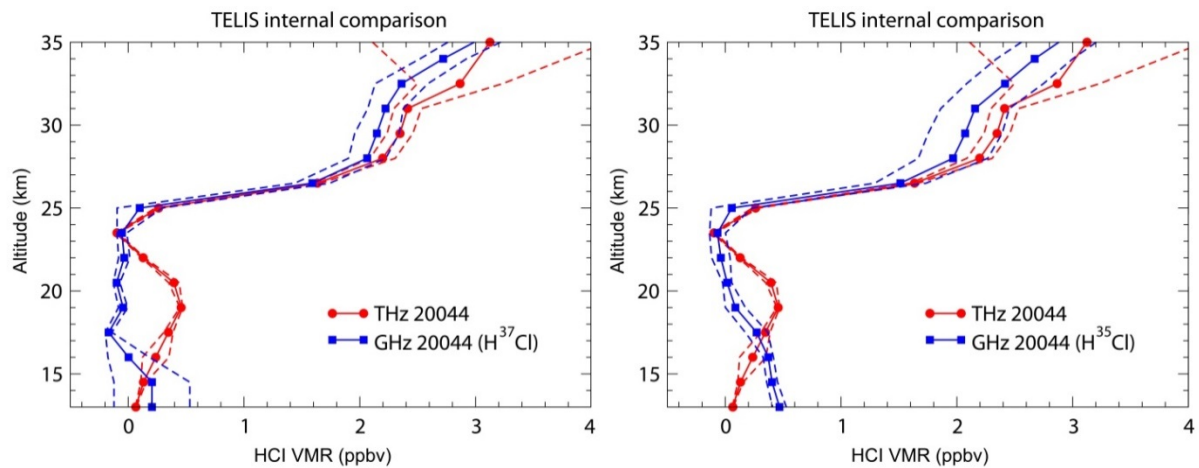


Fig. 3-13: Internal comparison of HCI retrieval between the 1.8 THz channel data and the 480-650 GHz channel data. The dashed lines indicate the estimated overall accuracy of the both retrievals. In case of the GHz channel, the HCI profile retrieved from both isotopes are included.

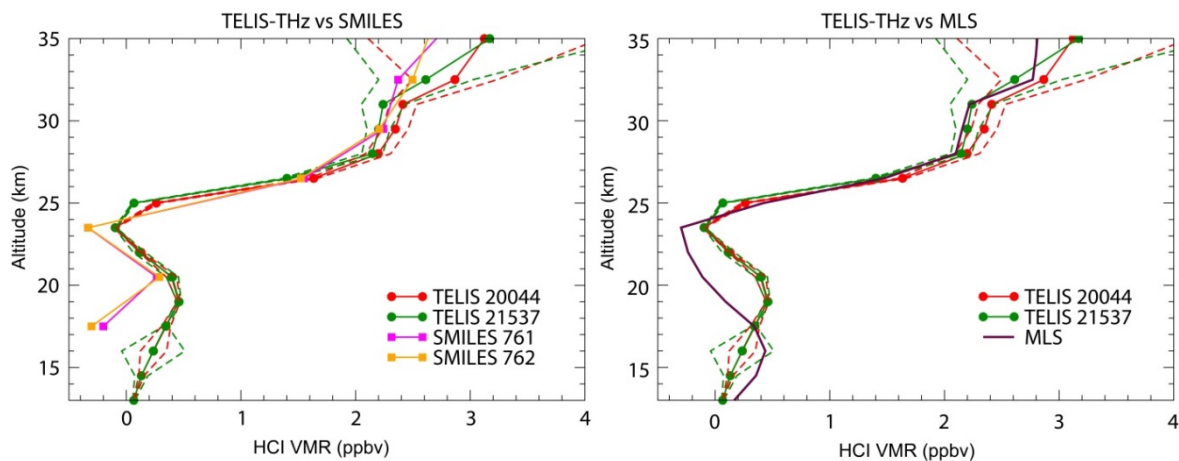


Fig. 3-14: External comparison of HCI retrieval between the TELIS far infrared measurements and the space-borne measurements by SMILES and MLS. The dashed lines indicate the estimated overall accuracy of the TELIS retrievals.

## References

Xu J., Schreier F., Vogt P., Doicu A., Trautmann T.: A sensitivity study for far infrared balloon-borne limb emission sounding of stratospheric trace gases. *Geoscientific Instrumentation, Methods and Data Systems Discussions (GID)*, 3, 251-303, Copernicus DOI: 10.5194/gid-3-251-2013, 2013.

## 3.6 A First Look at Temperature Retrieval by the Microwave Temperature Profiler

*J. Xu, F. Schreier, T. Trautmann*

Atmospheric temperature is one of the most important geophysical parameters related to fields such as meteorology, climatology, or photochemistry. In the case of infrared/microwave remote sensing, the vertical temperature profile can be estimated from thermal emission lines such as CO<sub>2</sub> or O<sub>2</sub>. In the case of microwave radiation, a standard approach is to derive the temperature profile by analyzing spectra of oxygen molecules. On the one hand, oxygen molecules are highly absorptive and emissive between 50 and 1 THz (see the left panel of Fig. 3-15). As the molecular abundances of oxygen are well-known and constant, we can deduce the physical temperature of the molecules that generates this emission. On the other hand, microwave temperature sensing techniques have the advantage that they are nearly unaffected by the presence of clouds and aerosols.

The Microwave Temperature Profiler (MTP) instrument is an airborne sensor system developed at the Jet Propulsion Laboratory (JPL). It has been used on hundreds of flights, including on DLR's Falcon aircraft. The instrument was designed to deliver altitude-dependent temperature profiles throughout an altitude range in the upper troposphere and lower stratosphere (UTLS). MTP consists of a passive microwave radiometer which measures the thermal radiation emitted by oxygen molecules at frequencies ranging from 55 to 60 GHz (see the right panel of Fig. 3-15). The instrument probes the atmosphere from near-zenith to near-nadir in the flight direction by using a scanning mirror to change the viewing angle.

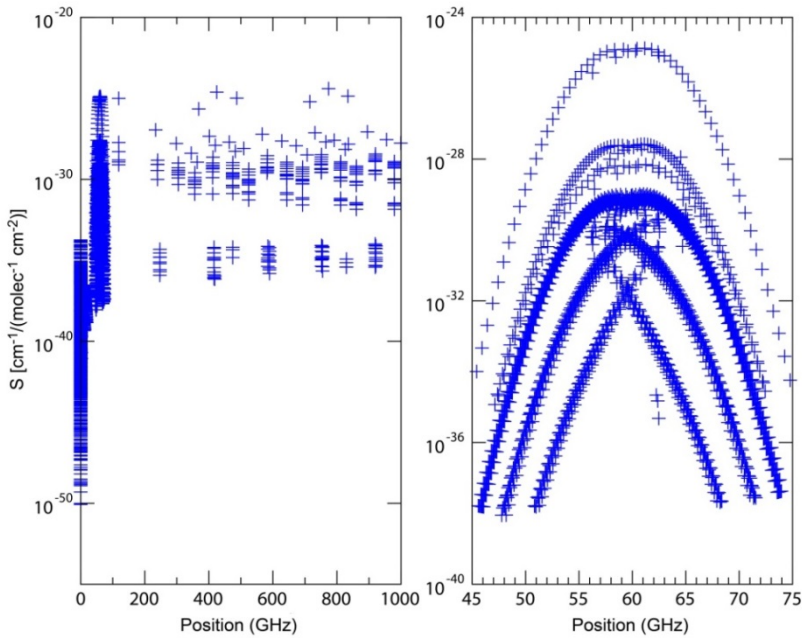


Figure 3-15: Oxygen lines in the spectral ranges of 0-1 THz (left) and 45-75 GHz (right).

For our future research we selected a typical microwindow of 56-58 GHz including one of three local oscillator frequencies (56.66 GHz) operated by MTP. The weighting functions, characterizing the sensitivity of the transmission at two different frequencies with respect to changes of altitude levels, are displayed in Fig. 3-16. Our work will focus on the development of a new retrieval algorithm dedicated to the temperature retrieval from microwave airborne measurements. To achieve this, the derivatives of radiance with respect to temperatures, utilizing automatic differentiation and further sensitivity studies, will be resolved.

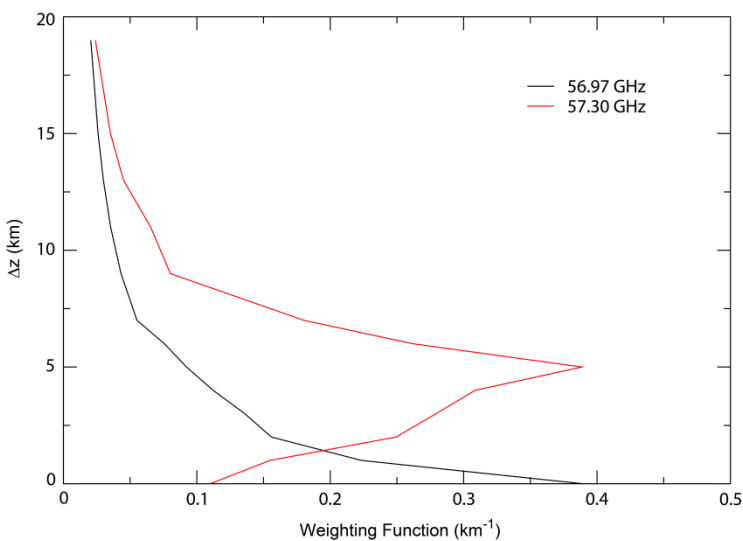


Fig. 3-16: Weighting functions  $\partial T_v / \partial(\Delta z)$  for two different frequencies (56.97 GHz for line center, 57.30 GHz for line wing) with respect to changes of altitude levels.

### 3.7 Scattering Simulations for the ADM-Aeolus Mission

K. Schmidt, D. Huber (DoRIT), T. Trautmann

The ESA ADM-Aeolus mission – tentative launch date is currently 2015 – shall acquire global vertical wind profiles for improving the accuracy of weather and climate predictions. ADM-Aeolus will carry the laser Doppler wind lidar *Aladin* which will probe the lowermost 30 km of the atmosphere at a wavelength of 355 nm. It measures Doppler shifts of moving scattering particles such as aerosols, cloud particles, and air molecules. Thus line-of-sight wind velocities can finally be derived.

To achieve this goal, the End-to-End Simulator (E2S) system has been developed. It consists of the Aeolus satellite simulator and the Aeolus level 1b processor. The former is used to construct simulation scenarios from which downlink data can be generated. The extinction and backscattering altitude profiles of different aerosol and cloud particles are basic inputs for such simulations. They can be extracted either from measurements or from computations for scatterer ensembles with predefined size, shape, permittivity, and altitude distributions. Once specified, the second step in the E2S, the Aeolus level 1b processor, ingests and processes the downlink data and produces line-of-sight wind velocities.

As part of the current ADM-Aeolus III project we investigate whether the given particle shapes – spherical or nonspherical – in computing extinction and backscattering profiles impact the derived Mie channel wind velocities. In order to estimate effects arising from nonspherical particles, spheroids have been considered. Oblate and prolate spheroids represent the simplest deviation from spheres. In doing so, the scattering database for spheroidal particles (*Schmidt et al. 2009*) has been used. If we observe significant effects caused by the spheroids, then more realistic and complex particle shapes can be taken into account. Our simulations assume, in each altitude layer, an ensemble of spherical and spheroidal particles with a given refractive index and averaged over a size distribution. Randomly oriented oblate and prolate spheroids with equally distributed aspect ratios have been considered. Realistic refractive indices, size distributions, and number density altitude profiles for various aerosols and cloud particles have been taken from the literature. Figs. 3-17 and 3-18 illustrate an example of such simulations.

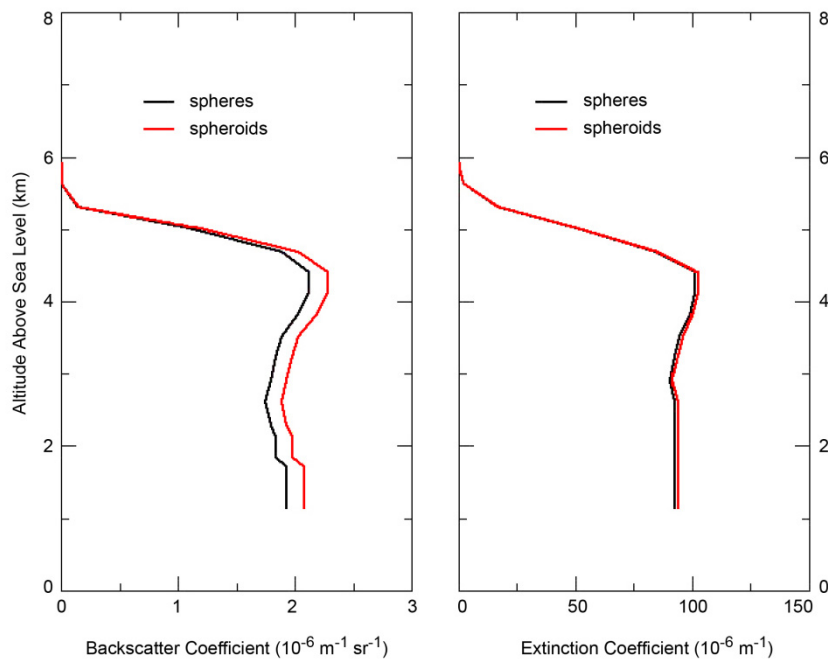


Fig. 3-17: Backscattering and extinction altitude profiles of mineral dust aerosols (accumulation mode) computed using the size distribution and the refractive index reported in *Gasteiger et al. (2011)* for ensembles of spheres and spheroids, respectively. The profiles of the spheres have been adjusted to the HSRL-FALCON measurements on 19 May 2006, 11:09 UTC, over Ouarzazate (Morocco) as reported by *Esselborn et al. (2009)*.

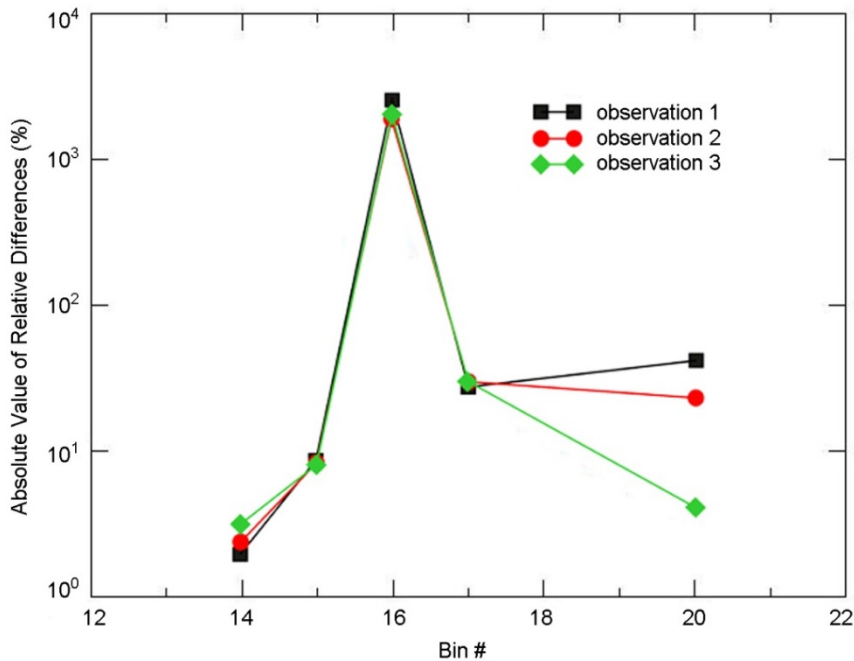


Fig. 3-18: Differences between the valid Mie channel wind velocities obtained by using the ADM-Aeolus E2S software for the spherical and spheroidal aerosol particles of Fig. 3-17 at cloudless conditions. Lower bin numbers correspond to higher altitudes while larger bin numbers represent altitudes near the ground. Note that three observations have been recorded during the chosen 30 s observation time. Every observation is an average over 30 single measurements.

The results obtained can be summarized as follows:

- No significant relation between the particle shapes (spherical or spheroidal) and the wind velocities derived has been observed.
- The differences between the wind velocities obtained for spherical and spheroidal particles decrease if the absolute values of the wind velocities increase. Vice versa, the differences increase if the absolute values of the wind velocities tend to zero.
- Near ground, the differences between the wind velocities obtained for spherical and spheroidal particles vary strongly.
- The cross-polarized backscattering cross sections of the spheroidal particles can be of the order of the co-polarized ones. This results in linear depolarization ratios, i.e. the ratio between the cross-polarized to the co-polarized backscattering cross section, of about 0.11-0.42.
- Particle shape information, however, can become important when deriving aerosol and cloud properties by means of the Aeolus level 2 processor.

Note that the scattering database for spheroidal particles, used for our simulations, has been extended to compute expansions of the phase matrix elements in terms of generalized spherical functions. This facilitates the coupling of the database with a number of existing radiative transfer and lidar programs such as VDISORT (*Schulz et al. 1999, 2000*) for future applications. The corresponding work has been performed by J. Wauer (theoretical physics & scientific software, Neustrelitz) in cooperation with M. Kahnert (SMHI Schweden) and T. Rother.

### References

*Esselborn M., Wirth M., Fix A., Weinzierl B., Rasp K., Tesche M., Petzold A.*: Spatial distribution and optical properties of Saharan dust observed by airborne high spectral resolution lidar during SAMUM 2006. *Tellus 61B*, 131-143, 2009.

*Gasteiger J., Wiegner M., Gross S., Freudenthaler V., Toledano C., Tesche M., Kandler K.*: Modelling lidar-relevant optical properties of complex mineral dust aerosols, *Tellus 63B*, 725-741, 2011.

*Schmidt K., Wauer J., Rother T., and Trautmann, T.*: Scattering database for spheroidal particles. *Appl. Optics 48*, 2154-2164, 2009.

Schulz F. M., Stamnes K., and Weng, F.: VDISORT: An improved and generalized discrete ordinate method for polarized (vector) radiative transfer. *J. Quant. Spectrosc. & Radiat. Transfer*, 61, 105-122, 1999.

Schulz F. M. and Stamnes K.: Angular distribution of the Stokes vector in a plane-parallel, vertically inhomogeneous medium in the vector discrete ordinate radiative transfer (VDISORT) model. *J. Quant. Spectrosc. & Radiat. Transfer*, 65, 609-620, 2000.

### 3.8 Scattering Data Base for Ice Particles to Study the Scattering Greenhouse Effect of CO<sub>2</sub> Ice Clouds

*T. Rother, D. Kitzmann (TU Berlin)*

The temperatures of a planet's surface and atmosphere usually depend on the planet's distance from the host star for a given spectral type. With increasing distance both parameters are expected to decrease due to the lower stellar insolation. In this respect the classical concept of a habitable zone for an Earth-like planet is determined by the orbital distance from the central star with its outer limit being reached when the surface temperature falls below the freezing point of water.

With lower surface temperatures the removal of CO<sub>2</sub> from the atmosphere by the carbon-silicate cycle, which controls the amount of CO<sub>2</sub> in the atmosphere, becomes less efficient. Thus, if a terrestrial planet is still geologically active, CO<sub>2</sub> can accumulate in the atmosphere by volcanic outgassing. With decreasing atmospheric temperatures, CO<sub>2</sub> will condense at some point to form clouds composed of CO<sub>2</sub> ice crystals.

Like in the case of water clouds, the presence of CO<sub>2</sub> clouds will result in an increase of the planetary albedo by scattering incident stellar radiation back to space. In contrast to water, CO<sub>2</sub> ice is almost transparent in the infrared with respect to absorption. Thus, a classical greenhouse effect by absorption and re-emission of thermal radiation is unlikely to occur for a cloud of CO<sub>2</sub> ice particles.

However, CO<sub>2</sub> ice particles can efficiently scatter thermal radiation back to the planetary surface, thereby creating a so called "scattering greenhouse effect". Depending on the cloud properties this scattering greenhouse effect can outweigh the albedo effect and can, in principle, increase the surface temperature above the freezing point of water, i.e. alter the location of the habitable zone.

All previous studies on this effect assumed a spherical particle geometry (*Kitzmann et al. 2013*) which, however, is unlikely to be the case, as known from the multitude of different water ice crystal shapes in the Earth atmosphere. Moreover, it is well-known that the light scattering properties of particles are strongly dependent on the particle shape. To gain first insights into such geometrical scattering effects we have considered light scattering on CO<sub>2</sub> ice particles with a regular but non-spherical boundary surface (spheroidal boundary) and a small-scale surface irregularity (small-scale Chebyshev surface of order  $n_0=43$  impressed on a spherical surface; *Rother et al. 2006*) at a size parameter of  $kr_{\text{eff}}=12$ . Scattering calculations have been performed for CO<sub>2</sub> ice particles without (refractive index:  $m=n$ ) and with absorption (refractive index:  $m=n + 0.001i$ ). Thus we could demonstrate that the small-scale surface irregularity has the largest impact on the asymmetry parameter, for example, if compared to corresponding spherical particles. This result is independent on whether absorptivity is taken into account or not (see Fig. 3-19 for details). We have therefore established a first scattering data base for CO<sub>2</sub> particles with a small-scale Chebyshev surface. This data base will be used in subsequent radiative transfer studies to estimate the scattering greenhouse effect of such particles. It is planned to add other particle geometries to the data base and to enlarge its size parameter range.

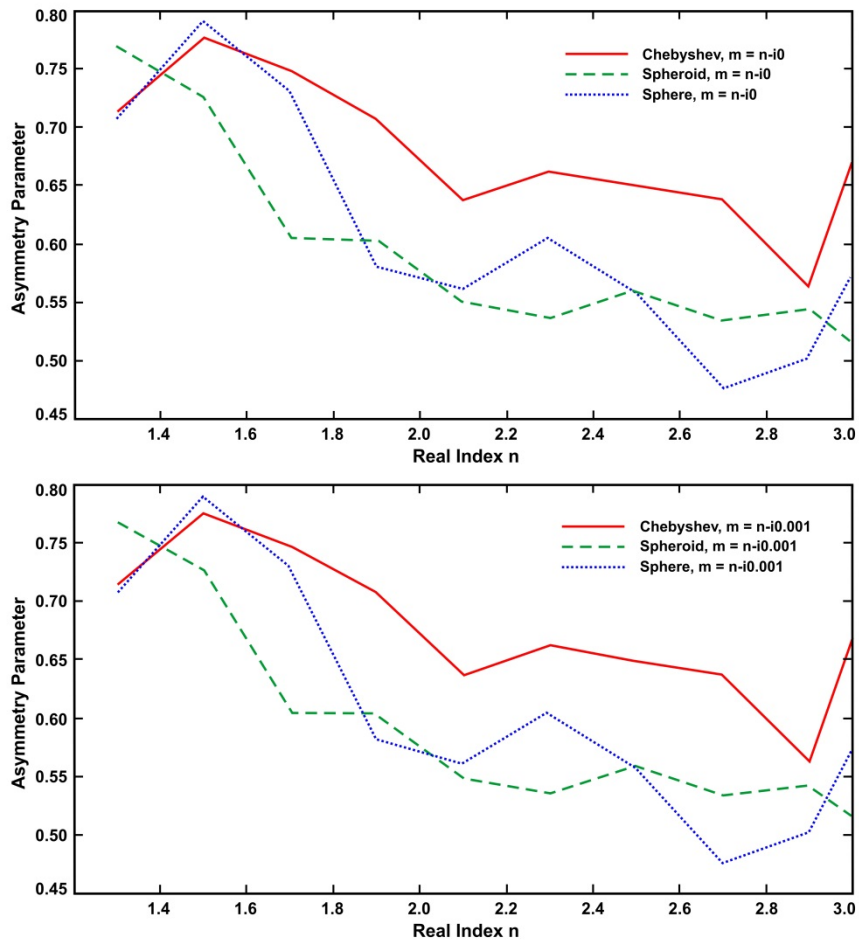


Fig. 3-19: Asymmetry parameter of different shapes of CO<sub>2</sub> ice particles, and at different refractive indices (real part n).

References:

Kitzmann D., Patzer B. and Rauer H.: Clouds in the atmosphere of extrasolar planets, *Astron. & Astrophys.* 557, A6, DOI: 10.1051/0004-6361/201220025, 2013.

Rother T., Schmidt K., Wauer J., Shcherbakov V. and Gayet J.-F.: Light scattering on Chebyshev particles of higher order, *Applied Optics* 45, pp. 6030-6037, 2006.

### 3.9 GARLIC – Generic Atmospheric Radiation Line-by-Line Infrared Code

*F. Schreier, S. Gimeno García, P. Hedelt, M. Hess, M. Vasquez, J. Xu, J. Mendrok (Division of Space Technology, Lulea University of Technology)*

For the simulation and analysis of high resolution infrared (IR) and microwave spectra, line-by-line (LbL) modeling of atmospheric radiative transfer (RT) is mandatory. Although in non-scattering atmospheres RT is straightforward to model – essentially two nested integrals according to Beer's and Schwarzschild's equation – LbL-RT is computationally challenging because accurate description of molecular absorption requires special function evaluations for many thousands of spectral lines, some dozen atmospheric levels, and thousands to millions of spectral grid points.

We have developed a suite of programs for high resolution infrared-microwave atmospheric radiative transfer modeling with emphasis on efficient and reliable numerical algorithms and a modular approach appropriate for simulation and/or retrieval in a variety of applications. GARLIC, the modern-Fortran re-implementation of MIRART, can deal with arbitrary observation geometries, instrumental field-of-view (FoV), and spectral response functions (SRF). A core of GARLIC's subroutines constitutes the basis of forward models used to implement inversion codes for retrieving atmospheric state parameters, e.g. BIRRA for the analysis of near-infrared nadir space-borne observations as performed by SCIAMACHY, or PILS in the case of far-infrared limb observations as executed by the balloon-borne TELIS. GARLIC and its descendants utilize an optimized Voigt function algorithm (*Schreier 2011*) combined with a two-grid approach (*Schreier 2006*) to accelerate the LbL modeling of molecular cross sections. Jacobians, i.e. derivatives with respect to the unknowns of the atmospheric inverse problem, are implemented by means of automatic differentiation.

A standard approach to code verification relies on cross-checking against similar codes developed independently, and in the last decade MIRART has participated in two extensive intercomparisons. Here a re-analysis of some of these test cases using GARLIC is presented; these tests also offered an opportunity to evaluate the performance of the different quadrature schemes implemented in GARLIC (for further details see *Schreier et al. 2014*).

#### **AMIL2DA**

In order to assess the consistency of geophysical data (level 2) generated by the MIPAS Fourier transform limb emission spectrometer onboard ENVISAT, the AMIL2DA (Advanced MIPAS level 2 Data Analysis) project aimed at carefully comparing and characterizing algorithms and data analysis strategies used by different European groups (*von Clarmann et al. 2003*). An essential step of this project was a cross comparison of the radiative transfer to be used as forward models of the group's MIPAS data processing. The intercomparison was organized as a series of exercises, starting from simple settings proving basic functionalities and proceeding to more complex and realistic scenarios. Exercise 20 has been set-up to test the integration of the radiative transfer equations along with the FoV and SRF convolutions. The intercomparison was based on a limb view with tangent altitude 40 km, an apodized FTS instrument line shape, a finite field-of-view and absorbers H<sub>2</sub>O, CO<sub>2</sub>, O<sub>3</sub>, N<sub>2</sub>O, and CH<sub>4</sub>. Fig. 3-20 shows

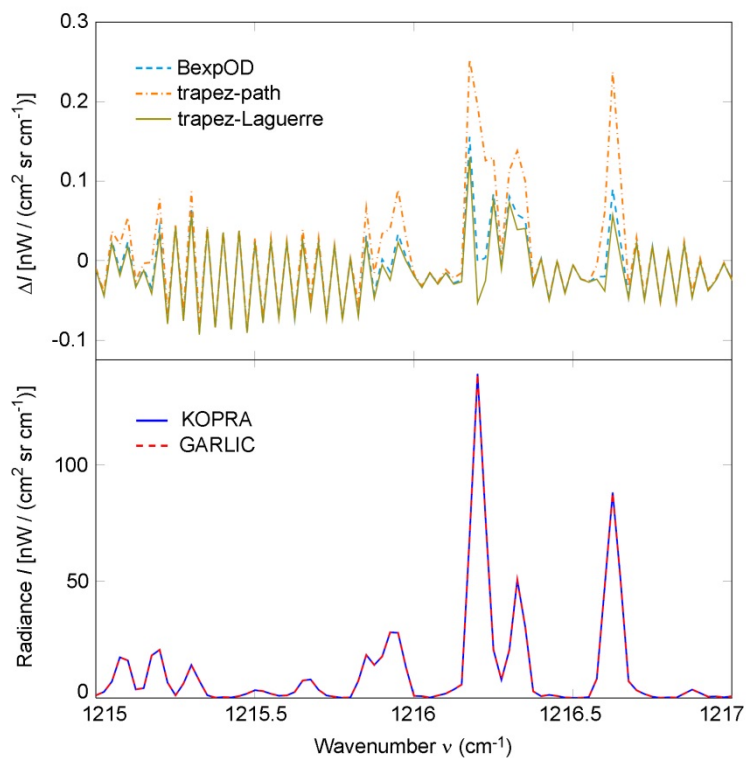


Fig. 3-20: AMIL2DA Forward model intercomparison (exercise 20): The bottom panel shows KOPRA versus GARLIC radiances while the top display illustrates the differences between both.

a comparison of KOPRA and GARLIC limb emission spectra, revealing deviations well below 1%. KOPRA (Karlsruhe Optimized and Precise Radiative transfer Algorithm) is a LbL, layer-by-layer model for forward calculation of infrared atmospheric transmittance and radiance spectra for various geometries and was specifically developed for the analysis of mid infrared limb emission sounder data, particularly MIPAS (Stiller *et al.* 2002).

### **IRTMW01**

A major objective of the Third International Radiative Transfer Modeling Workshop 2001 (IRTMW01) was the intercomparison of eight radiative transfer codes in the microwave spectral domain (Melsheimer *et al.* 2005). Similar to the AMIL2DA intercomparison, it was organized in a series of progressively more sophisticated “cases”, starting with an assessment of Voigt line shape and molecular absorption coefficient calculations. The purpose of case 3 was to check the correct implementation of the radiative transfer algorithm, n.b. the solution of the Beer and Schwarzschild integrals. In order to allow the discrimination of different sources of possible deviations between the models, absorption coefficients were precalculated with ARTS and used as common input. ARTS (Atmospheric Radiative Transfer Simulator) is a public domain project initiated and developed jointly by the University of Bremen and Chalmers University, Gothenburg (Bühler *et al.* 2005, Eriksson *et al.* 2011, see also <http://www.sat.ltu.se/arts/>) with an original focus on microwave applications). Case 3 *downlooking* essentially mimicked a microwave temperature sounder like AMSU-B (Advanced Microwave Sounding Unit) with three absorbers (O<sub>2</sub>, H<sub>2</sub>O, and N<sub>2</sub>), whereas case 3 *uplooking* corresponded to an airborne trace gas sounder (with two active species, O<sub>3</sub> and O<sub>2</sub>). Fig. 3-21 illustrates monochromatic spectra for the downlooking geometry, indicating differences to ARTS in the sub-Kelvin range except for overlapping parabola quadrature and trapezoid path-distance quadrature.

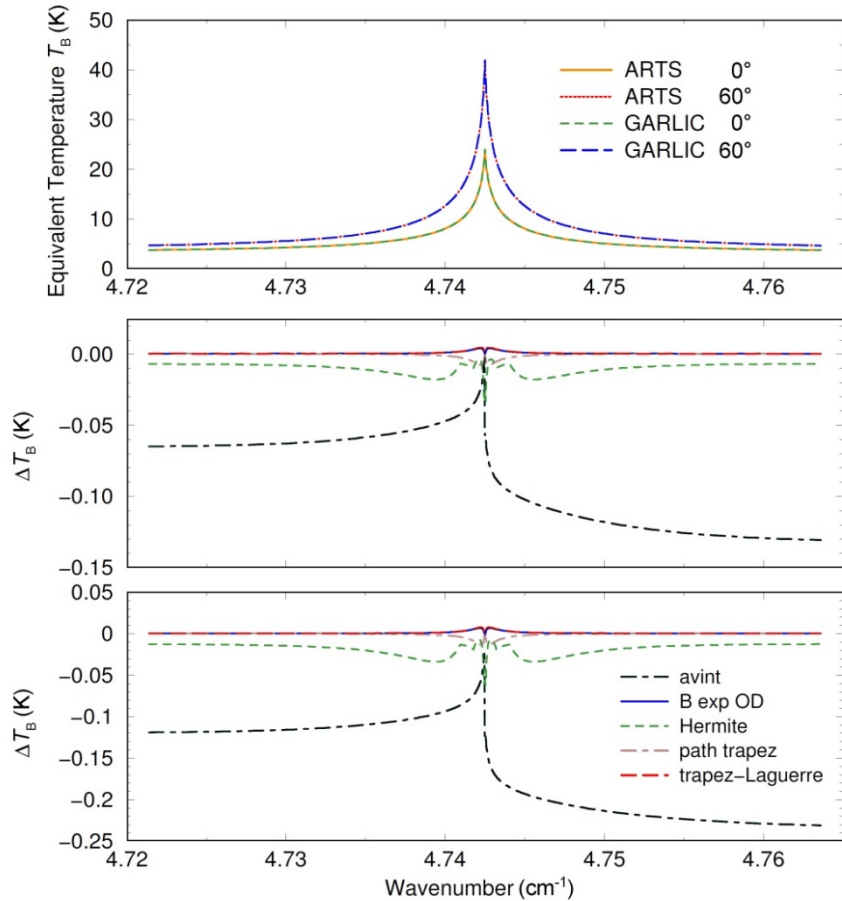


Fig. 3-21: IRTMW01 intercomparison ARTS vs. GARLIC (case 3): Equivalent temperatures for a downlooking geometry (top) with brightness temperature differences for 180° (middle) and 130° (bottom), respectively. The legend indicates the 5 different quadrature rules used by GARLIC.

The results of the two intercomparisons indicate the superiority of the trapezoid-Laguerre quadrature scheme using optical depth as integration variable. Accordingly, GARLIC uses this “Planck-linear-in-opticalDepth” approximation as the default quadrature scheme.

The results of the two intercomparisons indicate the superiority of the trapezoid-Laguerre quadrature scheme using optical depth as integration variable. Accordingly, GARLIC uses this “Planck-linear-in-opticalDepth” approximation as the default quadrature scheme.

### **References:**

Bühler S.A., Eriksson P., Kuhn T., von Engeln A., and Verdes C.: ARTS, the atmospheric radiative transfer simulator, *J. Quant. Spectrosc. & Radiat. Transfer*, 91:65–93, 2005.

Eriksson P., Bühler S.A., Davis C., Emde C., and Lemke O.: ARTS, the atmospheric radiative transfer simulator, version 2, *J. Quant. Spectrosc. and Radiat. Transfer*, 112(10):1551–1558, 2011.

Melsheimer C., Verdes C., Buehler S., Emde C., Eriksson P., et al.: Intercomparison of general purpose clear sky atmospheric radiative transfer models for the millimeter/submillimeter spectral range, *Radio Science*, 40:RS1007, 2005.

Schreier F.: Optimized evaluation of a large sum of functions using a three-grid approach, *Comp. Phys. Comm.*, 174, 783–802, doi: 10.1016/j.cpc.2005.12.015. 2006.

Schreier F.: Optimized implementations of rational approximations for the Voigt and complex error function, *J. Quant. Spectrosc. & Radiat. Transfer*, doi:10.1016/j.jqsrt.2010.12.010, 2011.

Schreier F., Gimeno García S., Hedelt P., Hess M., Mendrok J., Vasquez M., Xu, J.: GARLIC – A General Purpose Atmospheric Radiative Transfer Line-by-Line Infrared-Microwave Code: Implementation and Evaluation, *J. Quant. Spectrosc. & Radiat. Transfer*, 137, 29-50, doi: 10.1016/j.jqsrt.2013.11.018, 2014.

Stiller, G.P.: Sensitivity of trace gas abundances retrievals from infrared limb emission spectra to simplifying approximations in radiative transfer modelling, *J. Quant. Spectrosc. & Radiat. Transfer*, 72, 249–280, 2002.

von Clarmann, T., Hoepfner M., Funke B., Lopez-Puertas M., Dudhia A., et al.: Modeling of atmospheric mid-infrared radiative transfer: The AMIL2DA algorithm intercomparison experiment, *J. Quant. Spectrosc. & Radiat. Transfer* 78, 381-407, 2003.

### 3.10 A New Version of the OPAC Software

*M. Hess, F. Schreier*

OPAC (Optical Properties of Aerosols and Clouds) was released in 1998 as a climatological database of Mie calculations for typical aerosol components and clouds at 60 wavelengths and 8 relative humidities (Hess, Koepke and Schult 1998). It was complemented by a FORTRAN program giving access to the data and allowing to create mixtures of the given aerosol components and their optical properties. However, due to its architecture, software or data modifications and extensions were rather impossible. To permit further use of OPAC and especially improvements of the aerosol component data base, our goal was a refurbishment of the software and thus enabling the addition of any desired new aerosol components.

The OPAC database consists of text files containing the radiative properties of aerosol components and clouds. There is one such file for each component at each available humidity. These files are stored in a dedicated subdirectory. Furthermore, there is a configuration file containing the microphysical properties of all these components, i.e. the size distribution parameters, including the size limits, and the change of these parameters with relative humidity. The mixing ratios of a number of predefined typical mixtures of aerosol components are stored in this configuration file, too. The software OPAC allows the extraction of optical properties of aerosol components and clouds and of aerosol mixtures. The parameters to be extracted from the data base are selected in an input file.

The new software version OPACN is written in Python and uses object oriented programming for a modular structure. Input and output formats and files are identical or at least similar to the original version, i.e. the new software can be used to replace the original one without the need to modify other external software code. The original database remains unchanged and additions and modifications are handled in an extra configuration file. The Mie calculations for new components are now stored in a separate subdirectory (to maintain consistency, the data of the original OPAC version may not be modified).

As an example, the influence of very large particles on the extinction coefficient of desert dust is displayed in Fig. 3-22. Two new aerosol components are added, describing the size range of large desert dust particles (upper and lower envelope of airborne measurements), as they have been found during the SAMUM campaigns (Weinzierl et al. 2009). With these size distributions and refractive indices from OPAC, Mie calculations have been performed and included in the new OPACN database. These new components are used in the desert aerosol mixture instead of the original OPAC desert coarse mode. Fig. 3-23 shows a comparison between both illustrating the strong impact of the large particle mode of desert aerosols on their radiative properties.

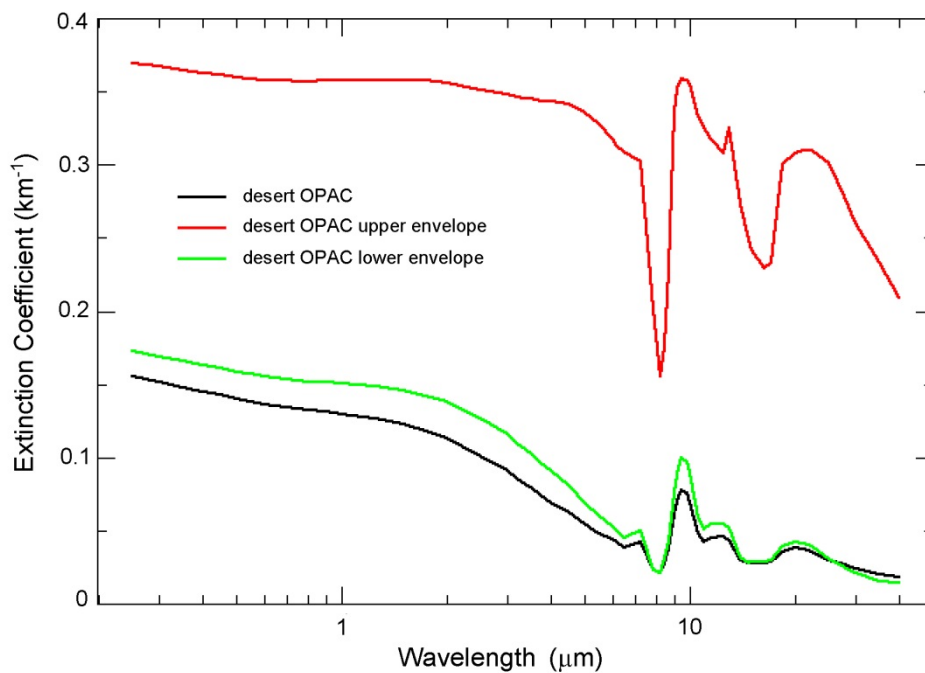


Fig. 3-22: Comparison of extinction coefficient of original OPAC desert aerosol and aerosol models with large particle mode from SAMUM data.

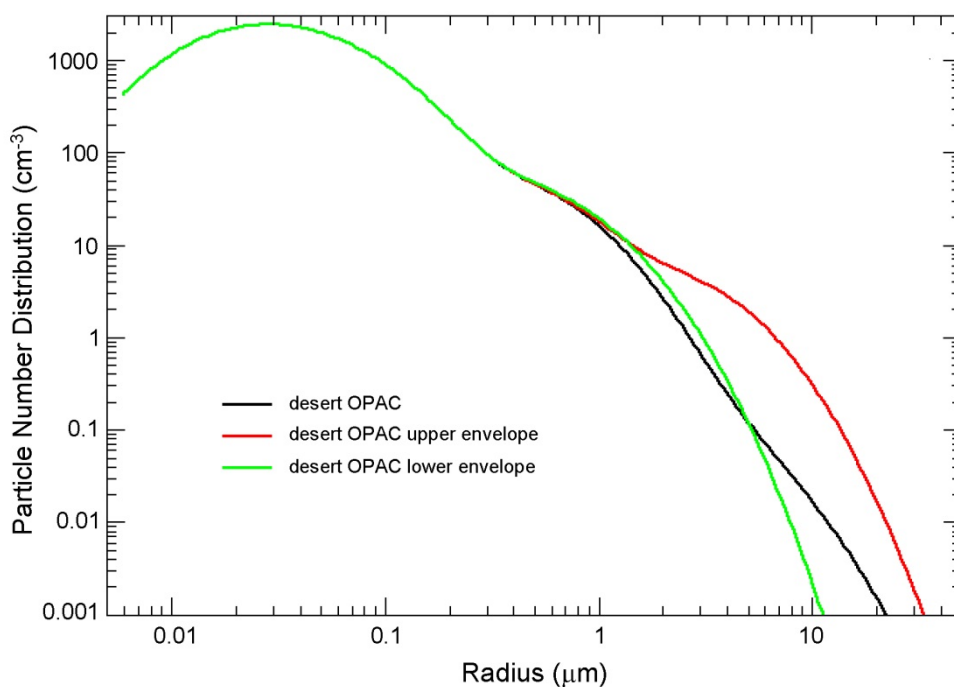


Fig. 3-23: Size distributions of the original OPAC desert aerosol and two modified versions with different large particle mode.

References:

Hess M., Koepke P., and Schult I.: Optical Properties of Aerosols and Clouds: The software package OPAC, Bull. Am. Met. Soc., 79, 831-844, 1998.

Weinzierl B., Petzold A., Esselborn M., Wirth M., Rasp K., Kandler K., Schütz L., Koepke P., Fiebig M.: Airborne measurements of dust layer properties, particle size distribution and mixing state of Saharan dust during SAMUM 2006. Tellus 61B, 96-117 doi: 10.1111/j.1600-0889.2008.00392.x, 2009.

### 3.11 Three-dimensional Radiative Transfer: Effects of Cloud Variability on TROPOMI Reflectivity Spectra

*S. Gimeno García, D. Loyola, T. Trautmann, R. Heinze, T. Riechelmann (both Hannover University)*

In order to guarantee high signal-to-noise ratios, the design of spectrometers aboard space-borne platforms is a tradeoff between spectral and spatial resolution. Since molecular absorption is highly spectrally dependent, atmospheric composition instruments favor spectral over spatial resolution.

The TROPOMI instrument onboard Sentinel 5 Precursor (S5P) will have a spatial resolution of about  $7 \times 7 \text{ km}^2$  at nadir, which clearly outperforms the resolution of previous atmospheric missions ( $320 \times 40 \text{ km}^2$  for GOME/ERS-2, about  $120 \times 30 \text{ km}^2$  for SCIAMACHY/ENVISAT and  $80 \times 40 \text{ km}^2$  for GOME-2/Metop-A and -B). However, although rather small, inside a TROPOMI ground pixel there may still be a considerable amount of unresolved cloud variability.

Therefore we performed a sensitivity study of reflectivities as a function of the unresolved cloud variability. For this purpose, we have simulated virtual measurements by a TROPOMI-like instrument in a cloudy scene at different spatial resolutions. Traditionally, the cloud parameter retrieval algorithms using atmospheric composition instruments have exploited the spectral region around the oxygen A-band centered at 760 nm, i.e. we also focus on this region. The cloud microphysical properties were provided by the Parallelized Large-Eddy-Simulation Model (PALM) at a spatial resolution of  $10 \times 10 \text{ m}^2$  covering a  $6.4 \times 6.4 \text{ km}^2$  domain. The cloud field used in our study corresponds to one snapshot of a cumulus formation run using the "bulk" approach. Running in this mode, the PALM model delivers three-dimensional (3D) distributions of liquid water content (LWC). The original PALM 3D LWC field was n-fold coarsened at different resolutions which were used as base for the resolution study.

We assumed that the cloud droplet size distribution in each cloud grid cell was represented by a gamma distribution with size parameter  $\alpha = 7$  and that the total number density of droplets was  $100 \text{ cm}^{-3}$ . Then, by means of the Mie scattering theory, the cloud optical properties were computed. Monochromatic line-by-line absorption coefficients were calculated for oxygen and water vapour molecules based on the US standard atmospheric profile and the HITRAN 2008 spectroscopic database. Rayleigh scattering was considered whereas aerosols were left out. The surface albedo was set to 0.1.

The synthetic spectra were calculated by means of the MoCaRT (Monte Carlo Radiative Transfer) 3D model. The solar zenith angle was set to  $30^\circ$ , the viewing zenith angle to  $15^\circ$  and the relative azimuth to  $45^\circ$ . This configuration is appropriate for highlighting the shadows under the clouds. The observer was located at top-of-the-atmosphere. The RT simulations were performed monochromatically and convolved with the TROPOMI-like instrumental slit function.

The spatially resolved reflectivities in Fig. 3-24 correspond to one spectral pixel at the beginning of the A-band. The spectra (top right) are calculated by averaging the spatially resolved reflectivities over the whole spatial domain at every spectral pixel (62 in total). Note that the instrumental slit functions (bottom right) are asymmetric and slightly differ from spectral pixel to pixel. The simulated reflectivity spectra are manifestly affected by the resolution at which we define the cloud properties: the coarser the resolution the higher the reflectivity. This is due to two principal reasons: the non-linear relationships between both the microphysical and optical properties, and between optical and radiative properties.

Although 3D effects are well known to affect the radiation transport and, by extension, the signal measured by any spectrometer, the RT models used in the retrieval algorithms do not account for them leading to errors in the interpretation of the data.

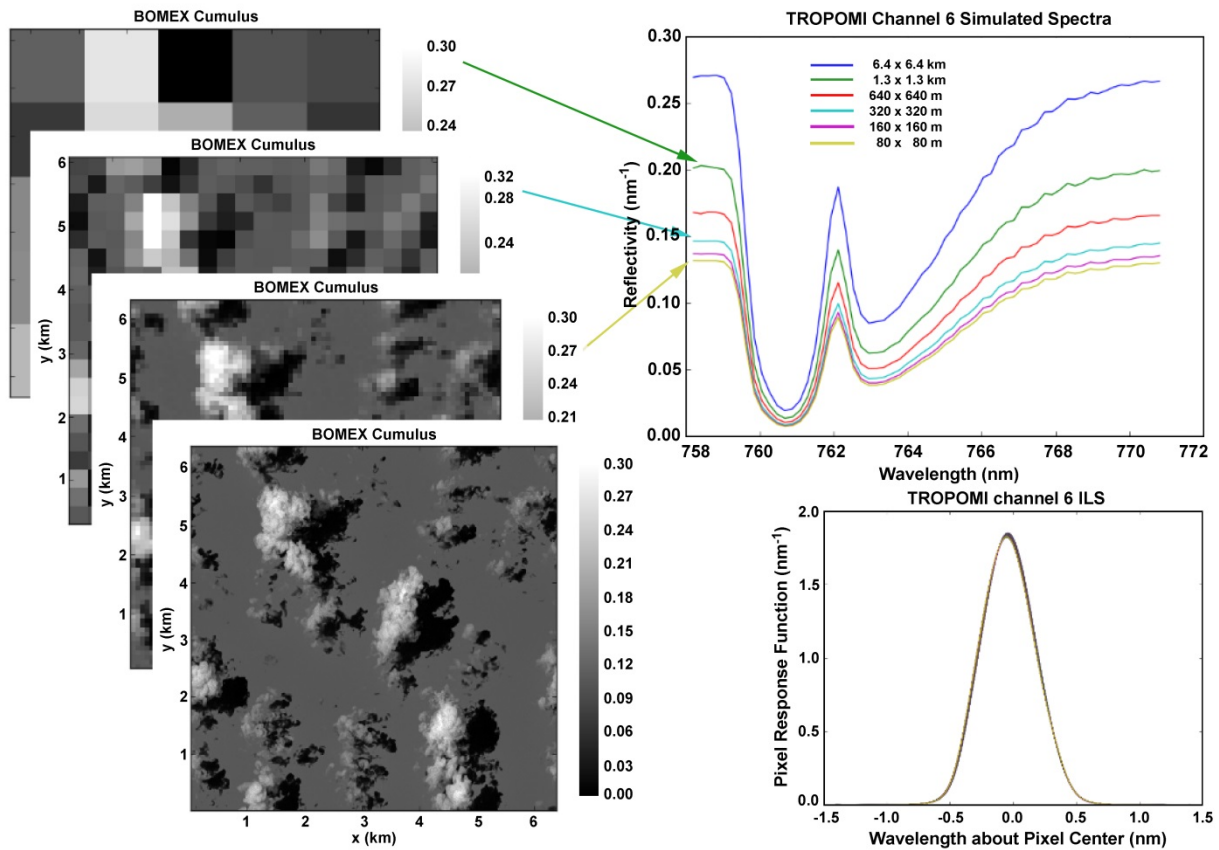


Fig. 3-24: Effect of spatial resolution on reflectivity. Left: Spatially resolved reflectivity fields calculated at different spatial resolutions. Top (right): Reflectivity spectra. Each point corresponds to the average over the whole domain. Bottom (right): Instrumental slit functions.

References:

*Gimeno García S., Trautmann T. and Venema V.:* Reduction of radiation biases by incorporating the missing cloud variability via downscaling techniques: a study using the 3-D MoCaRT model. *Atmospheric Measurement Techniques*, 5, 2261-2276, 2012.

*Heinze R., Raasch S. and Etling D.:* The structure of Karman vortex streets in the atmospheric boundary layer derived from large eddy simulation. *Meteorol. Z.*, 21, 221-237, 2012.

*Riechelmann T., Noh Y. and Raasch S.:* A new method for large-eddy simulations of clouds with Lagrangian droplets including the effects of turbulent collision. *New J. Phys.*, 14, 065008, 2012.

### 3.12 Discrete Ordinate Method with Matrix Exponential for Stochastic Radiative Transfer in Broken Cloud Fields

A. Doicu, D.S. Efremenko

Trace gas retrievals from nadir sounding instruments are hindered by the presence of clouds. For satellite instruments with a high spatial resolution, it is important to account for the sub-pixel cloud inhomogeneities, or at least, to assess their effect on the radiances at the top of the atmosphere, and in particular, on the retrieval results. This assessment is probabilistic since the detailed structure of the clouds is unknown and only a small number of statistical properties are given. In this regard, we have designed a stochastic model for the solar radiation problem and a molecular atmosphere with its underlying surface (Doicu *et al.* 2014). The model allows the computation of the mean radiance at the top of the atmosphere as it is intended to be used for trace gas retrievals.

By representing the radiance and the geometric fields as the sum of their mean values and their random fluctuations,

$$f = \bar{f} + f', \quad I = \bar{I} + I', \quad e^{-\tau_{\text{ext}}^{\odot}} = \overline{e^{-\tau_{\text{ext}}^{\odot}}} + (e^{-\tau_{\text{ext}}^{\odot}})'$$

we derived an  $n^{\text{th}}$ -order stochastic model for the solar radiation problem and arbitrary statistics:

$$\begin{aligned} & \Omega \cdot \nabla \overline{f^m I'} \\ &= \overline{(\Omega \cdot \nabla f^m) I'} - \sigma_{\text{ext}}^0 \overline{f^m I'} - \sigma_{\text{ext}}^{\text{1d}} \left( \overline{f'^{(n+1)} \bar{I}} - \overline{f^m f' I'} + \overline{f f^m I'} + \overline{f'^{(n+1)} I'} \right) \\ &+ \frac{1}{4\pi} \int_{4\pi} \left[ \sigma_{\text{sct}}^0 P_0 \overline{f^m I'} + \sigma_{\text{sct}}^{\text{1d}} P_1 \left( \overline{f'^{(n+1)} \bar{I}} - \overline{f^m f' I'} + \overline{f f^m I'} + \overline{f'^{(n+1)} I'} \right) \right] \\ &+ \frac{F_{\odot}}{4\pi} \left\{ \sigma_{\text{sct}}^0 P_0 \overline{f^m (e^{-\tau_{\text{ext}}^{\odot}})'} \right. \\ &\left. + \sigma_{\text{sct}}^{\text{1d}} P_1 \left[ \overline{f'^{(n+1)} e^{-\tau_{\text{ext}}^{\odot}}} - \overline{f^m f' (e^{-\tau_{\text{ext}}^{\odot}})'} + \overline{f f^m (e^{-\tau_{\text{ext}}^{\odot}})'} + \overline{f'^{(n+1)} (e^{-\tau_{\text{ext}}^{\odot}})'} \right] \right\}. \end{aligned}$$

where  $f$  is the random geometric function, such that the cloud scattering field is given by

$$\sigma_{\text{sct}}^{\text{1d}}(\mathbf{r}) = \sigma_{\text{sct}}^{\text{1d}}(\mathbf{r}) f(\mathbf{r})$$

with indices 0 and 1 referring to the clear sky and cloud, respectively. The stochastic model is expressed in matrix form, and is equipped with appropriate closure relations for the higher-order covariance terms. For broken clouds, the  $n^{\text{th}}$ -order stochastic model reduces to a first-order stochastic model for a two-dimensional radiance vector

$$\mathbf{I} = [ \bar{I}, \overline{f' I'} ]^T$$

whose entries are the mean radiance field and the covariance of the radiance and the indicator fields. This stochastic model is given by

$$\begin{aligned} \Omega \cdot \nabla \mathbf{I}(\mathbf{r}, \Omega) &= \mathbf{I}_{\nabla}(\mathbf{r}, \Omega) - \mathbf{\Sigma}(\mathbf{r}) \mathbf{I}(\mathbf{r}, \Omega) + \frac{1}{4\pi} \int_{4\pi} \mathbf{S}(\mathbf{r}, \Omega, \Omega') \mathbf{I}(\mathbf{r}, \Omega') d\Omega' \\ &+ \frac{F_{\odot}}{4\pi} \mathbf{S}(\mathbf{r}, \Omega, \Omega_{\odot}) \mathbf{I}_{\odot}(\mathbf{r}) \end{aligned}$$

This stochastic model is equivalent to a model based on Levermore-Pomraning equations (Levermore *et al.* 1988, Pomraning 1989), which is formulated in terms of the mean radiances in each material. Thus, the  $n^{\text{th}}$ -order stochastic model effectively generalizes the Levermore-Pomraning equations to arbitrary statistics.

To derive an estimate for the covariance of the radiance field and the gradient of the indicator field, we employed the standard assumption of the Levermore model, but used a limit representation of the Dirac

delta function. The same technique, which is conceptually simple, has been applied to two- and one-dimensional cloud fields. For computational purposes, we particularized the stochastic model for broken clouds to homogeneous three-, two- and one-dimensional cloud fields, discretized the resulting stochastic model in the discrete ordinate space, and solved it very efficiently by the matrix exponential formalism. The discrete ordinate method with matrix exponential is a very powerful tool which we also used to solve the stochastic equation in the framework of a two- and a fourth-order stochastic model for a bounded cascade cloud model.

The stochastic model deals with the solar radiation problem for a molecular atmosphere with its underlying surface, treats homogeneous three-, two- and one-dimensional broken clouds, and can be simply particularized to completely cloudy and clear skies. In Fig. 3-25 the numerical simulations have shown that the accuracy of the stochastic model is at least two times better than the accuracy of a linear mixing model (LMM). The reference solution is computed by ensemble averaging of multidimensional SHDOM solutions (Evans 1998). Obviously, the efficiency of the stochastic model is lower, because we have to solve a two-dimensional problem instead of two independent one-dimensional problems. For this reason, the stochastic model is not recommended for operational trace gas retrieval systems, but it can be integrated in "scientific" systems to analyze the effect of cloud inhomogeneities on the retrieval results.

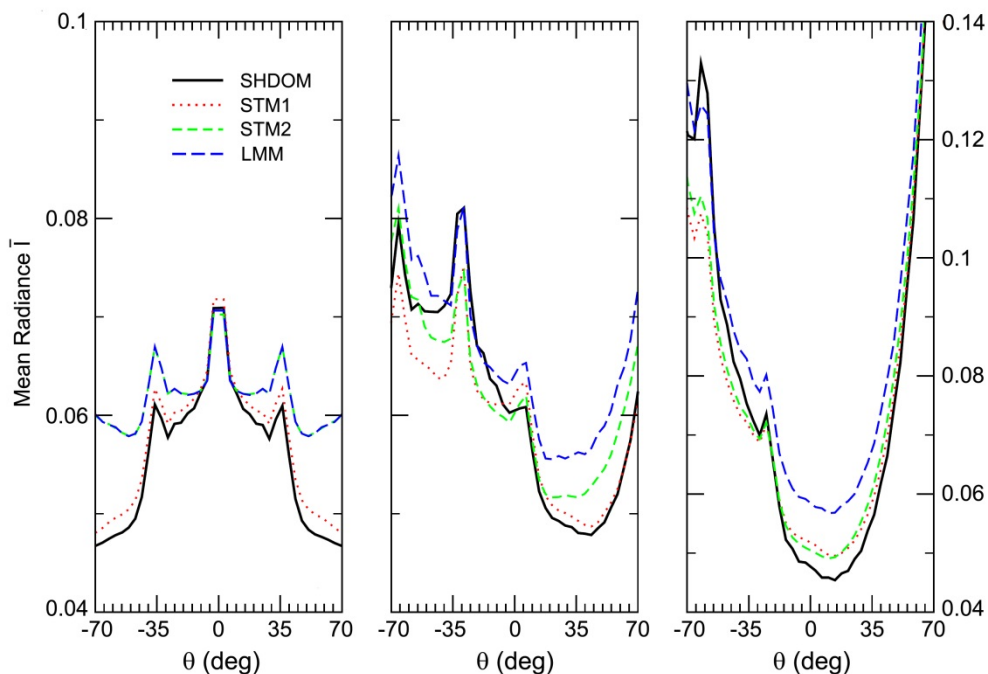


Fig.3-25: The mean radiance at the top of the atmosphere as a function of the scattering zenith angle  $\theta$  and for three values of the solar zenith angle:  $\theta_{\text{sun}}=0^\circ$  (left),  $\theta_{\text{sun}}=30^\circ$  (middle) and  $\theta_{\text{sun}}=60^\circ$  (right). The occupation probability is  $p=0.5$ . STM1 stands for a stochastic model using the first iteration solution, while STM2 stands for a stochastic model, in which we neglect the covariance vector  $l_v$  depending on the gradient of  $f'$ .

### References

Doicu A., Efremenko D.S., Loyola D., Trautmann T.: Discrete ordinate method with matrix exponential for stochastic radiative transfer in broken cloud fields. *J. Quant. Spectrosc. & Radiat. Transfer*, 138, 1-16, 2014.

Evans K.F.: The spherical harmonic discrete ordinate method for three-dimensional atmospheric radiative transfer. *J. Atmos. Sci.*, 55, 429-446, 1998.

Levermore C.D., Wong J., Pomraning G.C.: Renewal theory for transport processes in binary statistical mixtures. *J. Math. Phys.*, 29, 995-1004, 1988.

Pomraning G.C.: Statistics, renewal theory and particle transport. *J. Quant. Spectrosc. & Radiat. Transfer*, 42, 279-293, 1989.

### 3.13 Dimensionality Reduction Techniques for Trace Gas Retrieval: Principal Component Analysis and Alternatives

*D.S. Efremenko, A. Doicu, D. Loyola, T. Trautmann*

As a massive amount of spectral information is expected from the new generation of European atmospheric sensors Sentinel 5 Precursor, Sentinel 4 and Sentinel 5, a fast processing of the data in the UV-VIS spectral domain, is required. A principal component analysis (PCA, *Pearson 1901*) of the optical parameters of an atmospheric system has been proposed as an efficient and accurate method to perform radiative transfer calculations in an absorbing and scattering atmosphere (*Natraj et al. 2010*). The performance of this method is remarkable; e.g. the oxygen A-band spectrum was reproduced with an accuracy of 0.3%, while achieving an order of magnitude speed improvement. A linearized version of this PCA-based radiative transfer model and its application to the direct fitting of total ozone columns from GOME-type sensors have been provided by *Spurr et al. (2013)*. The authors found that the accuracy of the results is better than 0.5%, and that the performance enhancement amounts to a factor of 3.5-4.

We have extended this technique by introducing several dimensionality reduction techniques for the optical parameters (*Efremenko et al. 2014*). Besides the principal component analysis, these techniques include local linear embedding methods (locality pursuit embedding (LPE), locality preserving projection (LPP), locally embedded analysis (LEA)), and discrete orthogonal transforms (cosine, Legendre, wavelet). These locally linear methods can better produce the non-linearity of the data, while they have an inverse transformation, unlike non-linear projections. By linearizing the corresponding radiative transfer model, we developed a code for a practical problem of the total ozone column retrieval from GOME measurements.

The PCA-based radiative transfer model includes the following steps:

1. For each spectral point an approximate solution  $I_a$  based on the two-stream model is computed.
2. The principal component analysis is performed over the matrix  $\mathbf{X}$ , which contains wavelength-dependent parameters, so that its column  $\mathbf{x}_w$  refers to the specific wavelength. As a result we get a new basis vector  $\mathbf{a}_k$  and coordinates  $\mathbf{y}_{wk}$  of  $\mathbf{x}_k$  in a new basis, so that
- 3.

$$\mathbf{x}_w \approx \bar{\mathbf{x}} + \sum_{k=1}^M y_{wk} \mathbf{a}_k$$

where  $M$  is the number of principal components. Usually, two principal components are enough to compute a spectrum with an error of 0.1%.

4. The correction factor is then computed for each wavelength according to the formula given below:

$$f(\mathbf{x}_w) \approx f(\bar{\mathbf{x}}) + \frac{1}{2} \sum_{k=1}^M [f(\bar{\mathbf{x}} + \mathbf{a}_k) - f(\bar{\mathbf{x}} - \mathbf{a}_k)] y_{wk} + \frac{1}{2} \sum_{k=1}^M [f(\bar{\mathbf{x}} + \mathbf{a}_k) - 2f(\bar{\mathbf{x}}) + f(\bar{\mathbf{x}} - \mathbf{a}_k)] y_{wk}^2$$

For such computations one has to call a multi-stream model and a two-stream model  $2M+1$  times.

5. Finally, the correction is applied to the approximate spectrum:

$$\ln \frac{I(\lambda, \boldsymbol{\xi})}{I_a(\lambda, \boldsymbol{\xi})} = f_I(\lambda, \boldsymbol{\xi})$$

The design of a linearized radiative transfer model has been established in a natural way, without specializing the linearization approach to a specific dimensionality reduction method.

$$f_{\xi_i}(\lambda_w) = \ln \left[ \frac{\partial I}{\partial \xi_i}(\lambda_w) / \frac{\partial I_a}{\partial \xi_i}(\lambda_w) \right]$$

The relative differences in the radiance for the Huggins band corresponding to the exact radiative transfer model and the radiative transfer models with linear embedding methods are shown in Fig. 3-26. The numerical analysis, dealing with the retrieval of the total ozone column from the GOME instrument, has revealed the following conclusions:

- The maximum relative difference in the total ozone column retrieved by the PCA-based radiative transfer model is less than 0.006, while the speed improvement is of about 6.24-8.06.
- The local linear embedding methods are more accurate than PCA, and have comparable efficiencies. For example, the RMS relative difference of LPP is a factor 2 smaller than that of PCA, while the increase in computational time is of about 1.05-1.08.
- The discrete orthogonal transforms suffer from a lower accuracy and a lower computational efficiency as compared to the linear embedding methods. However, the differences are not considerable. For example, the accuracy of DWT is comparable to that of PCA, and the growth in the computational time amounts to about 1.22-1.30. In fact, the great merit of the discrete orthogonal transforms consists in the simplicity of their construction, e.g., the discrete cosine basis functions have a closed form representation, which does not depend on the statistic of the data set.

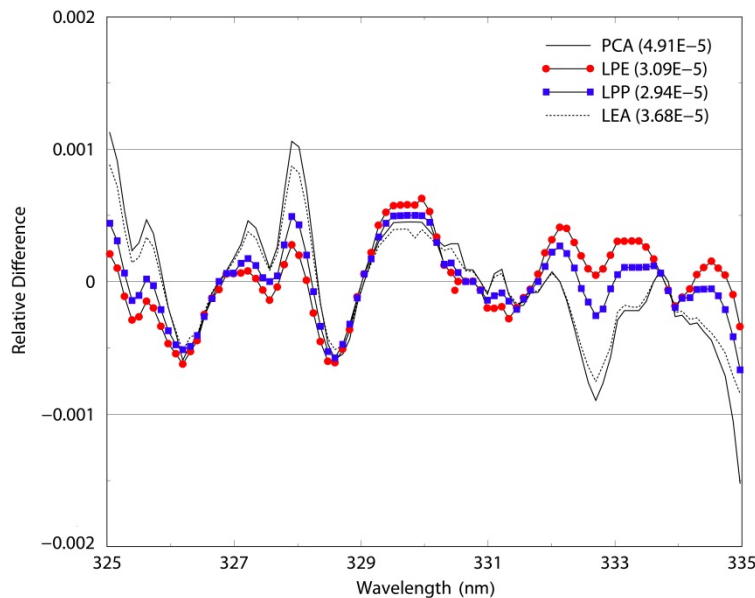


Fig.3-26: Relative differences in the radiance corresponding to the exact radiative transfer model and the radiative transfer models with linear embedding methods, with 2 principal components retained. The numbers in parentheses indicate the RMS of the relative difference.

### References

Natraj V., Shia R.L., Yung Y.L.: On the use of principal component analysis to speed up radiative transfer calculations. *J. Quant. Spectrosc. & Radiat. Transfer*, 111, 810-816, 2010.

Pearson K.: On lines and planes of closest fit to systems of points in space. *Phil. Mag*, 2, 559-572, 1901.

Spurr R., Natraj V., Lerot C., Van Roozendaal M., Loyola D.: Linearization of the Principal Component Analysis method for radiative transfer acceleration: Application to retrieval algorithms and sensitivity studies. *J. Quant. Spectrosc. & Radiat. Transfer*, 125, 1-17, 2013.

Efremenko D., Doicu A., Loyola D., Trautmann T.: Optical property dimensionality reduction techniques for accelerated radiative transfer performance: Application to remote sensing total ozone retrievals. *J. Quant. Spectrosc. & Radiat. Transfer*, 133, 128-135, 2014.

## 4. Atmospheric Remote Sensing – Applications

### 4.1 The Ozone\_CCI Project

*D. Loyola, M. Coldewey-Egbers, W. Zimmer*

The Ozone\_CCI is one of twelve projects of ESA's *Climate Change Initiative* (CCI). It delivers the Essential Climate Variable (ECV) Ozone in line with the requirements for satellite-based products for climate as defined by GCOS (Global Climate Observing System). The Ozone\_CCI includes data products for total ozone columns, ozone profiles from nadir sensors and stratospheric ozone profiles from limb and occultation sensors (see <http://www.esa-ozone-cci.org>).

The Ozone\_CCI project is led by BIRA-IASB, whereas we head the science team responsible for the GOME-type total ozone GTO-ECV CCI. DLR is further involved by leading the climate research group (Institut für Physik der Atmosphäre – IPA) and the system engineering team (Deutsches Fernerkundungsdatenzentrum – DFD) in Ozone\_CCI.

The baseline algorithm for total ozone retrieval from backscatter UV sensors is the GOME-type direct-fitting (GODFIT) algorithm jointly developed at BIRA-IASB, DLR-MF and RT-Solutions for implementation in version 5 of the GOME Data Processor (GDP) operational system. In contrast to previous versions of the GDP, which were based on the DOAS method, GODFIT uses a least-squares fitting inverse algorithm including direct multi-spectral radiative transfer simulation of earthshine radiances and Jacobians with respect to total ozone, albedo closure and other ancillary fitting parameters. A detailed description of the algorithm can be found in *Lerot et al. (2014)*.

Within the Ozone\_CCI project an algorithm has been developed by us for the creation of a level 3 merged monthly mean homogeneous total ozone product which combines measurements from the three sensors GOME/ERS-2, SCIAMACHY/ENVISAT and GOME-2/METOP-A. Individual GOME, SCIAMACHY, and GOME-2 level 2 total ozone data, processed with GODFIT V3.0, are the input to the level 3 processing. An inter-satellite calibration approach is used to create the merged total column product from the three sensors. In order to minimize the differences between the individual sensors, SCIAMACHY and GOME-2 data are adjusted to the GOME measurements during overlap periods (*Loyola et al. 2009, Loyola and Coldewey-Egbers 2012*). The correction factors for SCIAMACHY and GOME-2 with respect to GOME depend on latitude and time.

$1^\circ \times 1^\circ$  monthly mean total ozone gridded data are computed for GOME, adjusted SCIAMACHY, and adjusted GOME-2. The merged GTO-ECV data record then contains GOME data from April 1996 to March 2003, adjusted SCIAMACHY data from April 2003 to March 2007, and adjusted GOME-2 data from April 2007 to June 2011. Fig. 4-1 shows an example with data from October 2010.

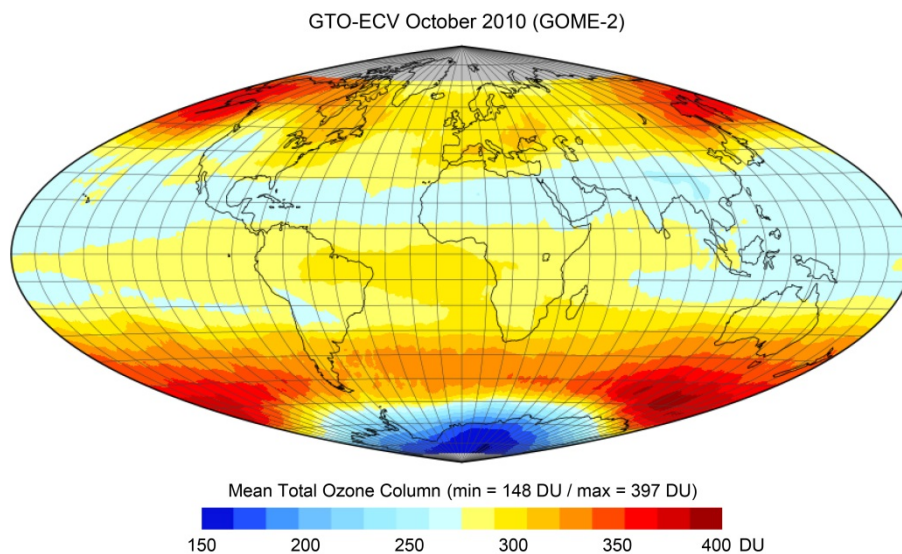


Fig. 4-1: GTO-ECV CCI mean total ozone from October 2010 (GOME-2 time period).

GTO-ECV October 2010 (GOME-2)

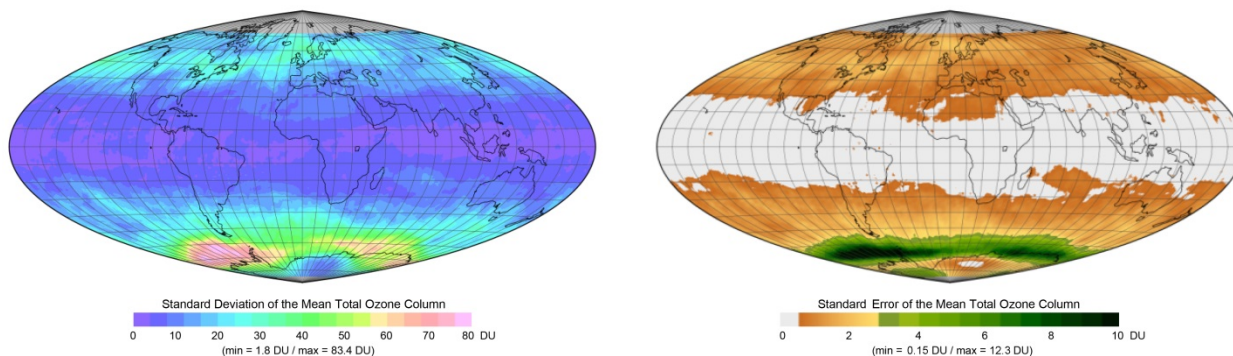
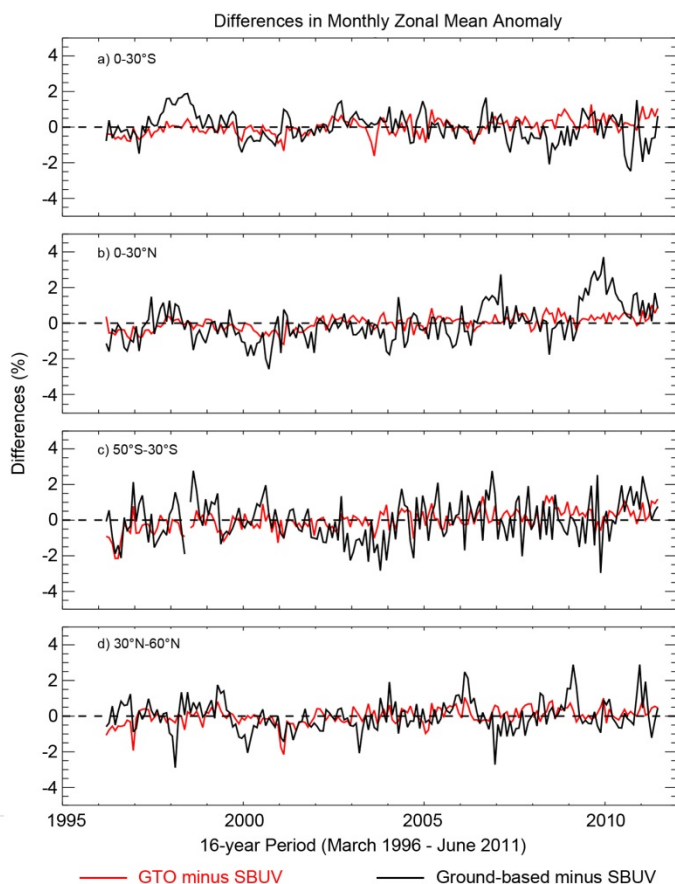


Fig. 4-2: GTO-ECV CCI standard deviation and standard error of the mean total ozone from October 2010 (GOME-2 time period).

The GTO-ECV dataset contains additionally the standard deviation and the standard error for each grid point, see example in Fig. 4-2. It is important to note that the standard error quantifies the spatial-temporal sampling errors inherent to the satellite measurements, the larger GTO-ECV errors correspond to the time periods where SCIAMACHY is used because of the lower sampling due to its alternating nadir/limb measurement mode.



*Chiou et al. (2013)* presents a comparison between GTO-ECV CCI total ozone data and the satellite SBUV(v8.6) profile total ozone and ground-based total ozone data records covering the 16-year overlap period (March 1996 through June 2011). It has been found that on average, the differences in monthly zonal mean total ozone vary between -0.32% to 0.76% and are well within 1%. The trends of the differences "GTO-ECV minus SBUV" are found to vary between -0.04% and 0.12% per year. These negligibly small trends have provided strong evidence that there are no significant time dependent differences among these multi-year total ozone data records.

Fig. 4-3: Differences in monthly zonal mean anomaly between GTO-ECV CCI, SBUV and ground-based data (Fig. 8 from *Chiou et al. 2013*).

During the second phase of the CCI project (2014-2016), the GTO-ECV data record will be extended with OMI/EOS-Aura and GOME-2/MetOp-B measurements. We will concentrate on (a) the development of novel merging algorithms that reduce the satellite sampling errors and (b) the creation of a homogeneous tropical tropospheric ozone product from GOME, SCIAMACHY and the two GOME-2 sensors. The two versions of the GTO-ECV data (GDP and CCI) can be downloaded from <http://atmos.eoc.dlr.de/gome/gto-ecv.html>.

### References:

Chiou E.W., Bhartia P.K., McPeters R.D., Loyola D.G., Coldewey-Egbers M., Fioletov V.E., Van Roozendaal M., Lerot C., Spurr R., Frith S.M.: Comparison of profile total ozone from SBUV(v8.6) with GOME-type and ground-based total ozone for 16-yr period (1996 to 2011), *Atmos. Meas. Tech. Discuss.* 6, 10081-10115, 2013.

Lerot C., Van Roozendaal M., Spurr R., Loyola D., Coldewey-Egbers M., Kochenova S., van Gent J., Koukouli M., Balis D., Lambert J.-C., Granville J., Zehner C.: Homogenized total ozone data records from the European sensors GOME/ERS-2, SCIAMACHY/Envisat and GOME-2/MetOp-A, *J. Geophys. Res.*, Accepted, 2014.

Loyola, D., Coldewey-Egbers M., Dameris, M., Garny, H., Stenke, A., Van Roozendaal M., Lerot C., Balis D., Koukouli M.: Global long-term monitoring of the ozone layer – a prerequisite for predictions, *Int. J. Remote Sensing* 30, 4295–4318, 2009.

Loyola D., Coldewey-Egbers M.: Multi-sensor data merging with stacked neural networks for the creation of satellite long-term climate data records, *EURASIP Journal on Advances in Signal Processing*, 2012.

## **4.2 Detection and Monitoring of Volcanic Eruptions with the GOME-2 Instrument**

*P. Hedelt, P. Valks, D. Loyola*

Volcanic eruptions pose a major threat not only to the local population and environment but also to aviation. Huge amounts of volcanic ash and SO<sub>2</sub> can be emitted into the atmosphere where it may be transported over long distances. The volcanic ash melts in the airplane engines thus leading to total engine failures in the worst case. Furthermore it is very abrasive and can quickly cause significant wear on propellers. When chemically converted into acid rain (H<sub>2</sub>SO<sub>4</sub>), also volcanic SO<sub>2</sub> poses a risk for aviation since it is very corrosive and may cause respiratory problems.

However only a very low number of active volcanoes are monitored from ground although more than 50 active volcanoes erupt every year. Satellite measurements allow for the monitoring of volcanic sites on a regular basis, even in remote regions (Fig. 4-4). These measurements are furthermore ideal for investigating global volcanic activity and, in combination with atmospheric dispersion models, to track and forecast volcanic plumes (*Flemming and Inness 2013*).

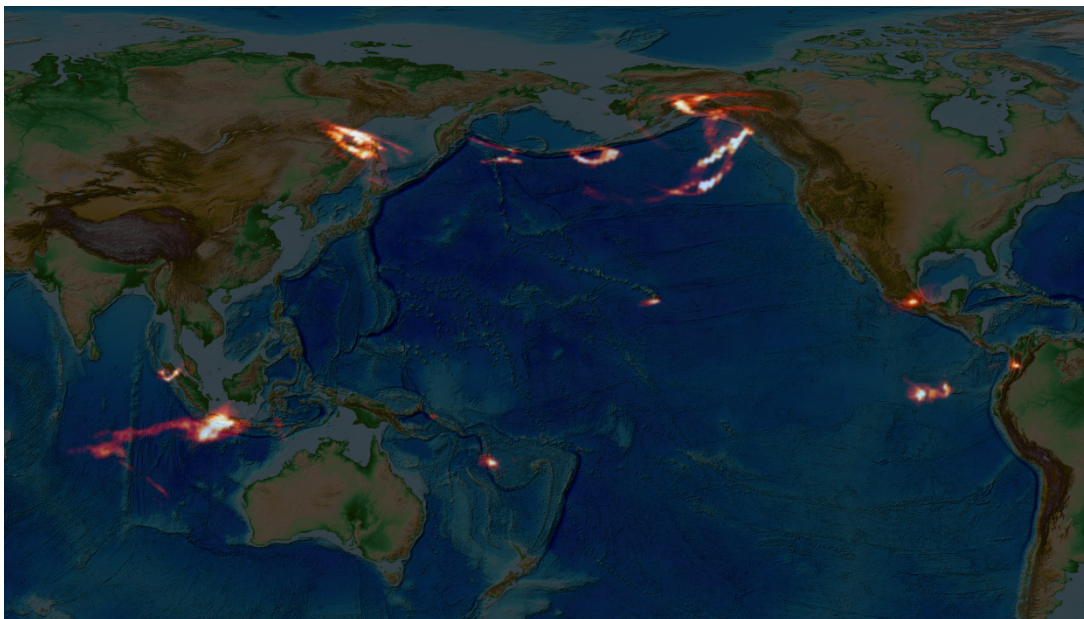


Fig. 4-4: Major volcanic eruptions detected by the GOME-2 instrument since 2007. The volcanos are related to Earth's tectonic activity and form the so-called "Ring of Fire" in the basin of the Pacific Ocean. The underlying elevation model is NOAA's ETOPO1 model.

Since volcanic SO<sub>2</sub> was found to be a good proxy for volcanic ash in some volcanic eruptions, we have developed an operational retrieval algorithm to detect and monitor volcanic eruptions based on measured total SO<sub>2</sub> columns. This algorithm has been developed in the framework of EUMETSAT's O3M-SAF and is since 2007 successfully applied to MetOp-A/GOME-2 data.

Since June 2013 also the retrieval of GOME-2 data from the MetOp-B satellite (launched in September 2012) is operational, after a 6 months' testing phase. In addition, the ongoing retrieval of MetOp-A/GOME-2 data was significantly improved with the implementation of the newest retrieval algorithm version GDP 4.7. It uses a modified offset correction scheme as well as a new algorithm – no longer based on empirical correction factors – to remove interference between SO<sub>2</sub> and O<sub>3</sub> in the standard fitting window. With the start of the operational retrieval of MetOp-B/GOME-2 data, the MetOp-A/GOME-2 instrument was switched to a smaller swath mode to compensate for the degradation of the instrument. The smaller swath width provided a higher spatial coverage of 40 km × 40 km per ground pixel, instead of the nominal 80 km × 40 km. Since both MetOp satellites operate in the same orbital plane with a phase shift of about 90°, using data from both instruments now allows for a global coverage on a daily scale.

The retrieved SO<sub>2</sub> columns are used by several projects, including SACS, a project to support aviation control based on satellite observations from instruments including GOME-2. The data is further exploited in the projects SMASH (Study of an end-to-end system for the monitoring of volcanic ash), EVOSS (European Volcanic Observatory System) as well as in MACC (Monitoring Atmospheric Composition and Climate). The MACC system forecasts volcanic plumes, which is essential for local stakeholders as well as for aviation control.

One of the first detections of a volcanic eruption using both instruments was achieved already in the preoperational phase of the MetOp-B/GOME-2 retrieval, thus allowing for an optimal test case in order to validate the retrieval results of the new sensor. On 22 December 2012 the Copahue volcano in the Chilean Andes erupted. Its eastward drifted SO<sub>2</sub> plume was detected by both instruments on 23 December 2012 and could be followed even two weeks after the eruption (Fig. 4-5).

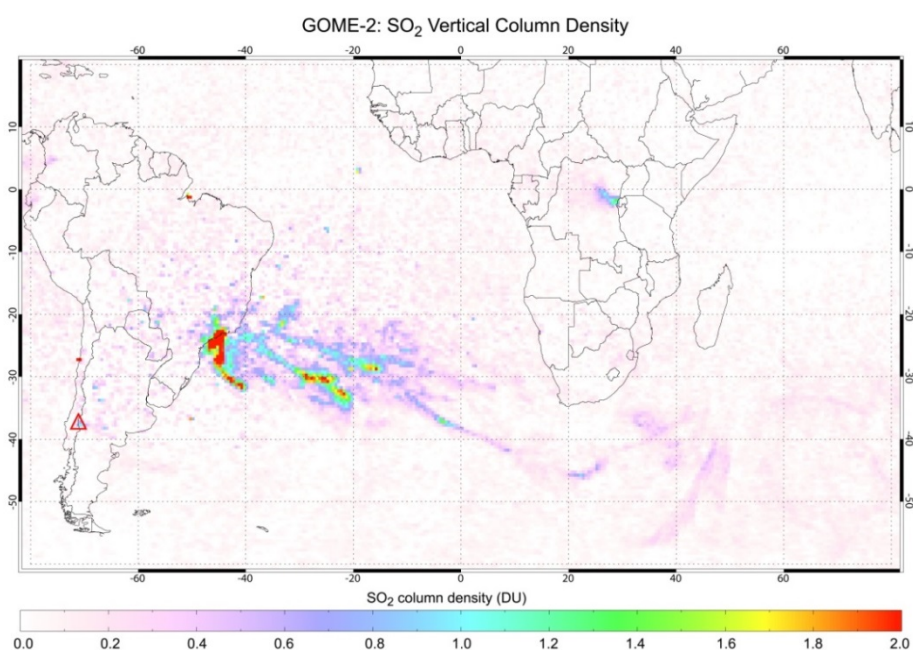


Fig. 4-5: SO<sub>2</sub> distribution over the Atlantic Ocean after the eruption of the Copahue volcano in the Chilean Andes (red triangle) on 22 December 2012. The image is an eight days composite of GOME-2 SO<sub>2</sub> data from the MetOp-B satellite.

### References

Flemming J., Inness A.: Volcanic sulfur dioxide plume forecasts based on UV satellite retrievals for the 2011 Grímsvötn and the 2010 Eyjafjallajökull eruption, *J. Geophys. Res. Atmos.*, 118, 10, 172–189, doi:10.1002/jgrd.50753, 2013

### 4.3 Dragon 3: Impact of the East Asian Monsoon on Tropospheric Ozone over Hong Kong

*N. Hao, A. Ding (ICGCR, Nanjing University)*

The impact of the East Asian monsoon (EAM) on climatology and interannual variability of tropospheric ozone over the coastal South China was investigated by analyzing 11 years of ozonesonde data over Hong Kong with the aid of Lagrangian dispersion modeling of carbon monoxide and calculation of an EAM index (*Zhou et al. 2013*). It was found that the seasonal cycle of ozone in the lower troposphere is highly related to the EAM over the study region. Ozone enhancements in the free troposphere are associated with the monsoon-induced transport of pollutants of continental anthropogenic and biomass burning origins.

#### **Background**

Tropospheric ozone plays an important role in air quality, tropospheric chemistry, and climate change. With a lifetime from several days to few weeks in the troposphere, O<sub>3</sub> can be transported over a long distance via large-scale circulations like monsoon. Also, ozone precursors, e.g. carbon monoxide (CO), nitrogen oxides (NO<sub>x</sub>) and hydrocarbons, can be transported by multi-scale circulations and produce more O<sub>3</sub> during the transport period. The subtropical East Asia is a region with an increasing trend in levels of tropospheric O<sub>3</sub> and its precursors, as well as a complex monsoon climate. The latter is manifested through strong seasonal and interannual variabilities of monsoon circulations. Located in coastal South China, Hong Kong is influenced by distinct winter and summer monsoons. The main purposes of our study were to quantify the vertical distribution of tropospheric O<sub>3</sub> in this region from a climatological perspective and to assess the impact of the EAM on the climatology and interannual variability of tropospheric O<sub>3</sub> mixing ratios over Hong Kong.

#### **Data and Methodology**

Within the Dragon 3 project, we utilized 11 years of ozonesonde data recorded at the Hong Kong Observatory (HKO) during 2000-2010. Each sounding was launched on a weekly basis at local time 13:00-14:00 at the King's Park Meteorological Station (114.17° E, 22.31° N, 66 m above sea level) of the HKO. We used level 3 monthly averaged MOPITT CO data during the 11-year study period to help interpret the possible causes for the observed variability in O<sub>3</sub> mixing ratios. This dataset has a spatial resolution of 1° × 1° in latitude and longitude and 10 layers from the surface to the 100-hPa level.

To gain insights into the origins of tropospheric O<sub>3</sub>, Lagrangian particle dispersion modeling (LPDM) simulations of CO were carried out for each ozonesonde profile based on a method developed and evaluated by *Ding et al. (2013)* using the Hybrid Single-Particle Lagrangian Integrated Trajectory (HYSPPLIT) model. For each profile, 3000 particles were released from layers with increments of 500 m from surface to 8 km altitude over the site and were traced backward for a 7-day period. The "footprint" residence time, i.e. retroplumes, of each sample was calculated and multiplied by emission to estimate potential source contributions to CO levels. Since our study focused on the lower troposphere, the domain of the LPDM simulation was 100° × 80° in longitude and latitude, centered over Hong Kong. We used the 1.25° × 1.25° data from the Japanese reanalysis project from the Japan Meteorological Agency to drive the model. Based on the calculated retroplumes and an emission inventory of anthropogenic CO in Asia prepared for INTEX-B and the GFEDv3 monthly CO emission inventory, the CO profiles attributed to anthropogenic and biomass burning emissions were calculated corresponding to each profile of O<sub>3</sub>. Retroplume at an altitude of 300 m was used to calculate CO mixing ratios to consider the plume rise effect of fires, while retroplume at an altitude of 100 m was used for anthropogenic emission.

In this study, we used a revised dynamical normalized seasonality monsoon index (DNSMI) to investigate the relationship between O<sub>3</sub> and EAM. The DNSMI is defined as:

$$\delta = 2 - \frac{\|\bar{V}_1 - V_i\|}{\|\bar{V}\|},$$

where  $V_i$  is the monthly mean wind vector in month  $i$ ,  $\bar{V}_1$  is the climatological mean wind vector in January, and  $\bar{V}$  is the climatological mean wind vector of January and July. According to this definition, the index gives the monthly intensity of monsoon, with a reference to the wind climatology in January and July, i.e. summer monsoon and winter monsoon. We calculated the DNSMI using monthly

NCEP/NCAR reanalysis data. To make the index represent a relatively large region, the data at five grids next to Hong Kong in each of the four directions were used.

### Results

Fig. 4-6a displays the seasonal variation of the averaged vertical distribution of tropospheric  $O_3$  from ground surface to the altitude of 16 km during 2000-2010 as a function of months in a year. A tongue-shaped  $O_3$  enhancement ( $> 65$  ppbv) extended from the lower stratosphere down to 6-7 km altitudes over the April-June timeframe. A similarly shaped low  $O_3$  ( $< 40$  ppbv) band extended from the surface to the 6 km altitude from April to August. An isolated area of  $O_3$  enhancement appeared around 3 km altitude in March. In addition, two moderate  $O_3$  enhancements (50-65 ppbv) were observed in the mid- to upper-troposphere from June to October and in the upper planetary boundary layer (PBL) in September and October, isolated by an area of low  $O_3$  values at 2-3 km altitudes in October and November. Fig. 4-6b exhibits the vertical distribution of monthly averaged MOPITT CO retrievals. It was shown that 120-150 ppbv CO was observed from the mid- to upper-troposphere throughout the whole year with altitude changes from about 4 km in winter to over 8 km in spring, and to around ground surface in summer. A low CO center (with CO mixing ratio below 100 ppbv) appeared at altitudes between 1-6 km in July and August. The distinct seasonal variation of lower troposphere CO shows a linkage with the  $O_3$  seasonal pattern. An area of high PBL CO levels in winter (up to 400 ppbv around the surface in December) corresponded to a low  $O_3$  layer in the PBL, where the  $O_3$  generally showed a negative correlation with CO in cold seasons. The summertime CO valley between altitudes of 1-6 km correlates with the low  $O_3$  air in low troposphere in summer.

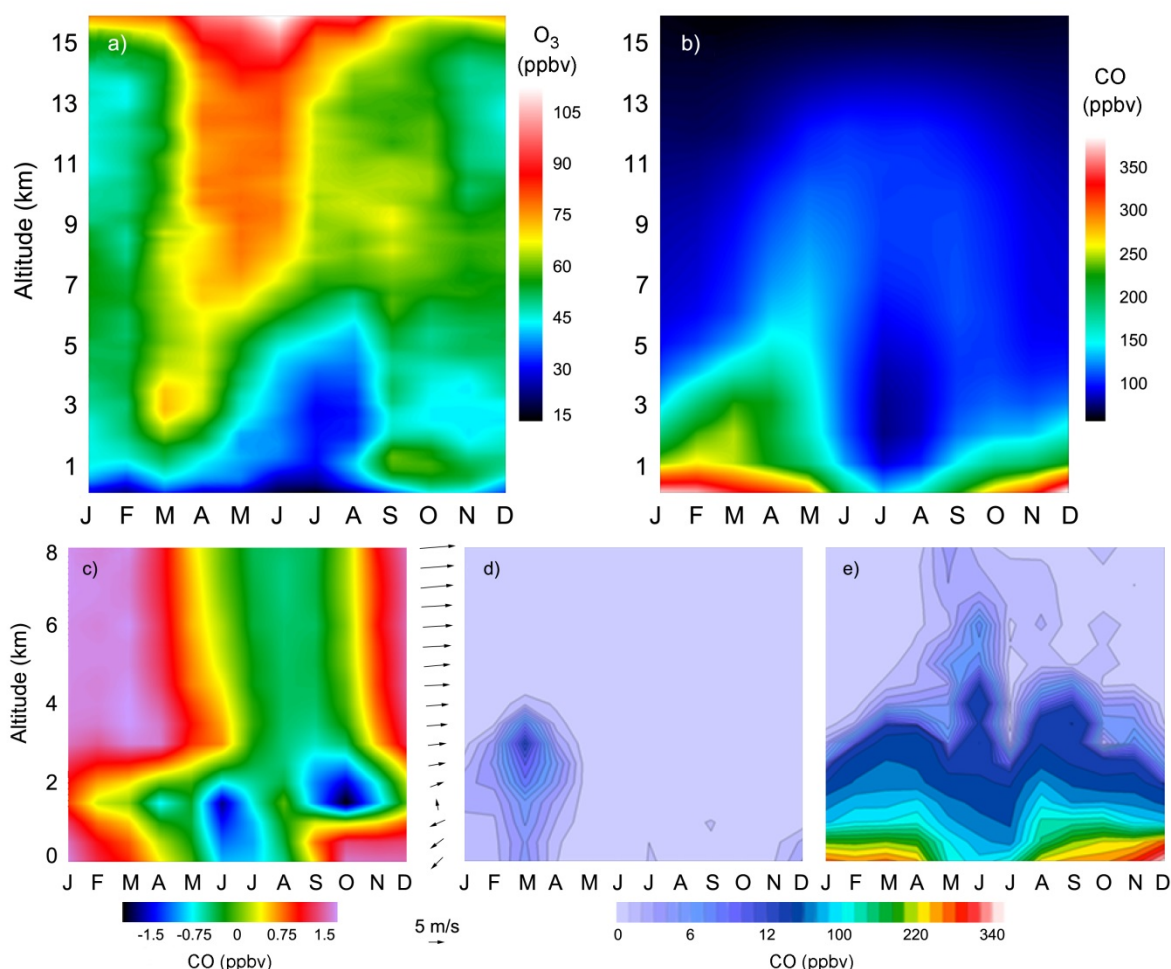


Fig. 4-6: Climatologically vertical distributions of  $O_3$  concentration from the ozonesonde measurement (a), CO concentration from MOPITT retrievals (b), DNSMI (c) and LPDM simulated CO concentrations from biomass burning emissions (d) and anthropogenic sources (e) as a function of month of a year during 2000-2010. Note: Arrows at the right-hand side of (c) show the averaged wind vectors at different layers in January during 2000-2010, which was used as reference in the DNSMI calculation (adapted from Fig. 1 in Zhou *et al.* 2013).

To identify the influence of the EAM on tropospheric O<sub>3</sub>, the distribution of DNSMI was examined for the period of 2000–2010 (Fig. 4-6c). Because the DNSMI relies on the wind in the reference month, i.e. January, we also present the climatological mean wind vectors around Hong Kong for different vertical layers in the right-hand side of Fig. 4-6c. It shows a northeasterly wind in the PBL and westerlies over 2 km altitude. The winter and summer EAMs were clearly distinguished by negative and positive values, respectively. In the PBL, the high positive DNSMI value (> 1) represents strong northeasterly winter wind. The summer monsoon extended to 3 km altitude with a negative DNSMI at 1.5 km altitude (~850 hPa), which matched with the summertime low O<sub>3</sub> and CO centers suggested in Fig. 4-6a and 4-6b, respectively. Another low DNSMI center at 2-3 km altitudes existed in autumn (Fig. 4-6c), corresponding to a low O<sub>3</sub> center. These results further corroborated that the seasonal variation in lower tropospheric O<sub>3</sub> mixing ratios were linked intimately to the winter and summer EAMs.

The CO vertical distribution was further simulated using LPDM. Fig. 4-6d and 4-6e show the simulated CO mixing ratios using a sum of emission from biomass burning and anthropogenic sources, respectively. These results shed new insights into mechanisms controlling the distribution of CO in the lower and mid-troposphere. In these simulations, only the emissions during a 7-day backward period were accounted for, and the model results in these figures are based on simulations for the 453 ozonesonde profiles. Higher values aside, simulated anthropogenic CO concentrations showed a pattern somewhat similar to that of the MOPITT retrievals. The lofted springtime CO plumes in March and the middle tropospheric CO enhancements during May-June and August-September were also well characterized by the model. With biomass burning emissions, the simulations did suggest a notable enhancement (up to 15 ppbv) at 2-4 km altitudes in March, although the total amount was much smaller than that from continental fossil fuel pollution (20-50 ppbv). These results further confirmed that the frontal lifting in spring, which is generally associated with a strong winter monsoon, is very important for lower and middle tropospheric CO and O<sub>3</sub>.

The time series of averaged PBL O<sub>3</sub> mixing ratios from ozonesonde data were compared with that from surface measurements at Hok Tsui, a regional station about 15 km southeast to the King's Park station, to examine whether weekly ozonesonde data could capture interannual variability of tropospheric O<sub>3</sub>. As shown in Fig. 4-7, a very good agreement between the two datasets is found.

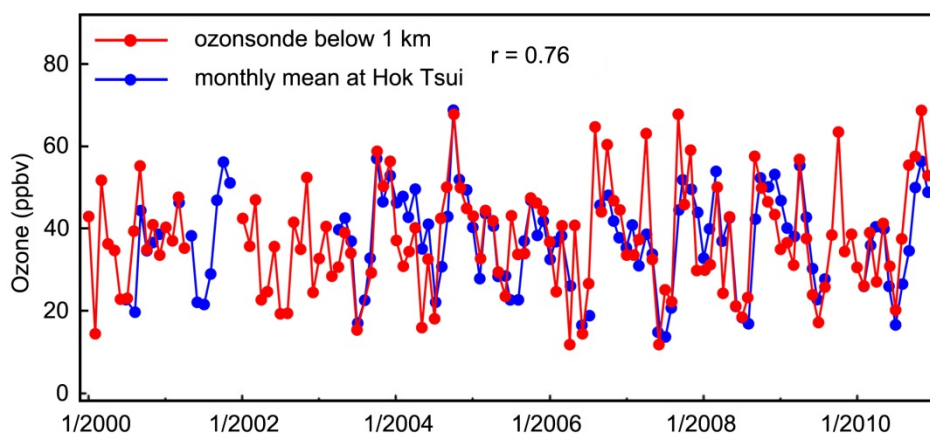


Fig. 4-7: Time series of monthly averaged surface O<sub>3</sub> at Hok Tsui site and averaged PBL (below 1 km) O<sub>3</sub> concentration from the ozonesonde data (adapted from Fig. 4A in Zhou *et al.* 2013).

The amplitude of interannual variability of tropospheric O<sub>3</sub> shown in Table 4-1 suggests that O<sub>3</sub> had a strong interannual variability in the lower troposphere, with annual amplitude of ~49% below 3 km altitude and 30% at 3-8 km altitudes. This pattern is consistent with the DNSMI distribution shown in Fig. 4-6c. In the PBL (< 1 km altitude), the interannual variability of O<sub>3</sub> levels was particularly high, with an annual rate about 61% and over 70% in spring and summer. The high amplitude in summer might be related to relatively low mean O<sub>3</sub> levels under the influence of summer monsoon but a strong year-to-year variability in frequency of occurrence of the Northwest Pacific Typhoon, which has been found to be the main synoptic pattern causing photochemical pollution in South China.

Altitude (km)	Winter (%)	Spring (%)	Summer (%)	Autumn (%)	Annual (%)
0-1	39	71	78	55	61
0-3	31	53	65	47	49
3-8	28	27	35	32	30

Table 4-1: Mean amplitude of interannual variability of tropospheric O<sub>3</sub> over Hong Kong. Note: the amplitude of each month is defined as (maximum + 2<sup>nd</sup> maximum – minimum - 2<sup>nd</sup> minimum) × 0.5/monthly mean during 2000-2010 (adapted from Table 1 in Zhou et al. 2013).

Ozone concentrations in Fig. 4-8 suggest a strong interannual variation with varying degree of correlation with the DNSMI. Good correlation was observed in the PBL, with  $r = 0.69$  and  $-0.82$  for spring and autumn, respectively. A weak correlation ( $r = 0.35$ ) existed at 2-4 km altitudes in March

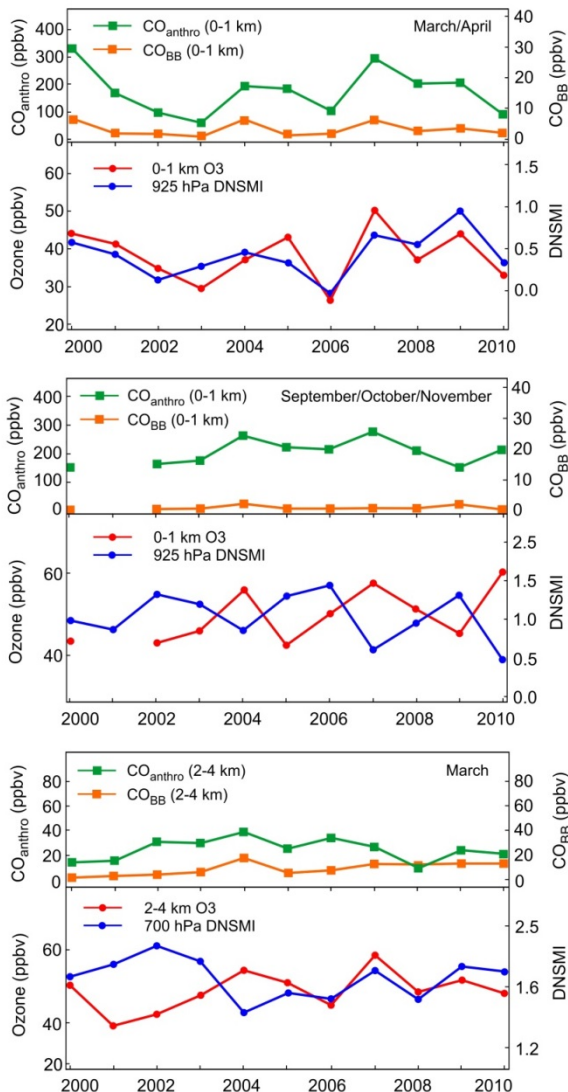


Fig. 4-8. Time series of averaged PBL O<sub>3</sub>, 925-hPa DNSMI, and LPDM simulated CO from anthropogenic and biomass burning emissions for March-April (top) and for September-November (middle) during 2000-2010. The bottom panel shows the same but for 2-4 km altitude in March during 2000-2010 (adapted from Fig. 2 in Zhou et al. 2013).

during the entire period because the correlation changes from negative to positive after 2005. According to the definition of DNSMI introduced before, the DNSMI depends on the difference in mean wind vector with that in the reference month, i.e. January. In winter, a higher DNSMI means a stronger winter monsoon, while in summer a lower DNSMI represents a stronger summer monsoon. Here in South China, the mean wind autumn is the same as that in January but is different in spring (southeasterly). This could be the main causes for the different PBL DNSMI-O<sub>3</sub> correlation in the two seasons.

LPDM simulations showed clearly that O<sub>3</sub> mixing ratios correlated positively with CO mixing ratios that were simulated using anthropogenic emissions. In the PBL, the contribution from biomass burning emissions was 1-2 orders of magnitude smaller than that from anthropogenic emissions (Fig. 4-8 top and middle). Because we used a constant anthropogenic emission rate for the entire 11-year period and monthly emission rates for biomass burning, a simulated strong interannual variability in the anthropogenic contribution suggested that the interannual variability in the EAM was a dominant factor controlling levels of O<sub>3</sub> and its precursors in the lower troposphere over South China. In March, at 2-4 km altitudes, a positive correlation between O<sub>3</sub> and DNSMI was found over 2005-2010 but not over 2000-2004, possibly due to more influence from the interannual variation in biomass burning and anthropogenic emissions.

Our results indicate that the DNSMI can potentially be a useful index for predicting interannual variations in lower tropospheric O<sub>3</sub> levels in South China. In spring and autumn, the transition seasons when annual peaks of O<sub>3</sub> occurred, changes of intensity, time of occurrence, and/or duration of large-scale monsoon circulation could significantly influence the interannual variation in mean O<sub>3</sub> levels and frequency of O<sub>3</sub> nonattainment in this region.

## References

Zhou D.R., Ding A.J., Mao H.T., Fu C.B., Wang T., Chan L.Y., Ding K., Zhang Y., Liu J., Lu A., Hao N.: Impacts of the East Asian monsoon on lower tropospheric ozone over coastal South China. *Environ. Res. Lett.*, 8, 044011, 2013.

Ding A.J., Wang T. and Fu C. B.: Transport characteristics and origins of carbon monoxide and ozone in Hong Kong, South China. *J. Geophys. Res.*, 118, 9475–88, 2013.

## 4.4 Textbook on Mathematical Chemistry and Chemoinformatics and its Relevance to Astrobiology

M. Meringer E.L. Schymanski (Eawag)

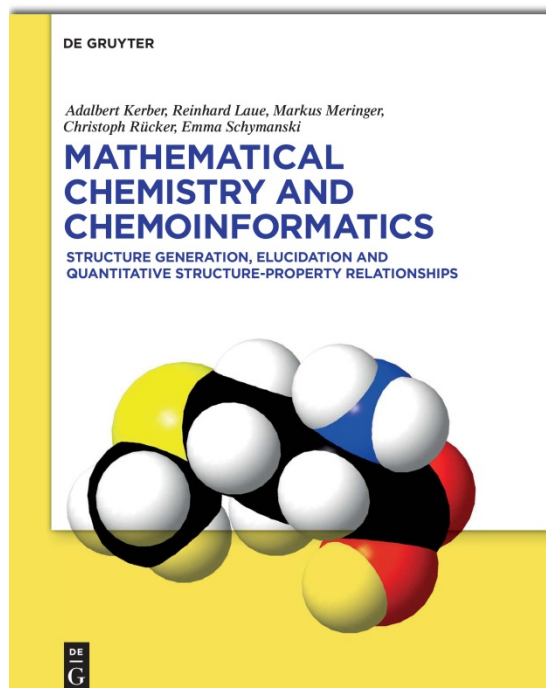
The textbook *Mathematical Chemistry and Chemoinformatics* was published by De Gruyter in 2013, written by a group of authors originating from multiple disciplines, including mathematics, computer sciences and chemistry (Kerber *et al.* 2013). It is based on more than 20 years of experience in molecular structure generation, from conceptualization through to software-technical implementation.

The book provides an introduction to mathematical modeling of molecules and the resulting applications (structure generation, structure elucidation and quantitative structure-property relationships). A central topic is the generation of molecular structures on constitutional level. Structure generation is the only way to systematically create molecules that are not present in a database, i.e. have neither been found in nature nor been synthesized yet. For these reasons such *in silico* methods are ideally suited to support astrobiology research, in particular biomolecular foundations and the origin of life.

The idea to use structure generation for astrobiology research is not new. Already in the mid 1960's Nobel laureate and exobiologist Joshua Lederberg initiated the well known DENDRAL project (Lindsay *et al.* 1980). Its aim was the automated structure elucidation of organic compounds by mass spectrometry (MS). Interestingly, even NASA was among the founders of this pioneering project, with the ambitious intention to supply future Mars missions with such software, to enable analysis and interpretation of MS samples onboard a space probe and to broadcast only identified structural formulas back to Earth instead of huge MS data sets. DENDRAL is described in many computer science books as the first expert system and it can be considered as one of the roots of chemoinformatics and as an indirect predecessor of the work presented in this new textbook.

The book starts with the mathematical theory behind representing molecules, explaining chemical concepts in mathematical terms and providing exercises that can be completed online. **Chapter 1** introduces basics of graphs and molecular graphs, as well as group actions to describe chemical compounds as unlabeled molecular graphs. **Chapter 2** continues with advanced properties of molecular graphs, including substructures, molecular descriptors, mesomerism and graphical representations of chemical reactions. **Chapters 3** and **Chapter 4** discuss mathematical treatment of phenomena beyond constitutional level, namely chirality and stereoisomerism.

**Chapter 5** describes different strategies and important aspects of molecular structure generation. Structure generation problems are classified by their input, e.g. a molecular formula combined with structural constraints, a set of reactions and reactants, or a generic structural formula. Methods from



discrete mathematics, such as orderly generation or the homomorphism principle are introduced and applied to construct chemical compound spaces and combinatorial libraries. Principles for canonizing molecular graphs are applied to avoid isomorphic duplicates. Corresponding algorithms are described in detail. The chapter is completed by remarks on efficient data structures for molecular graphs.

The later chapters cover applications that reach beyond the generation of structures. This means to link molecular structures with physical, chemical or biological properties. **Chapter 6** describes important tools for this purpose, principles of supervised statistical learning, including linear models, neural networks, support vector machines and decision trees. **Chapter 7** shows how to establish quantitative structure property relationships (QSPR). Such QSPRs are used if a physico-chemical property has to be predicted for a given molecular structure. The opposite direction, predicting structures from given properties is also part of chemoinformatics. This situation typically occurs in molecular structure elucidation, when physical properties are supplied by spectroscopic measurements of an unknown compound, and the corresponding molecular structure has to be determined. **Chapters 8** and **Chapter 9** are devoted to such problems, particularly originating from mass spectrometry.

A number of interesting applications in astrobiology can be accessed with the methods described in this book. A first pilot study on the amino acid structural space in cooperation with NASA's Astrobiology Institute and Tokyo Tech's Earth Life Science Institute has been completed recently (*Meringer, Cleaves and Freeland 2013*). A similar project, now focusing on nucleotides, is scheduled for spring 2014. Other classes of biomolecules could be subject of future *in silico* generation and analysis, for instance to examine their abilities to resist harmful UV radiation, or the light absorbing behavior of pigments that might supply energy harvesting mechanisms for life on exoplanets orbiting stars of different spectral classes (*de Vera and von Paris 2013*).

Concerning structure elucidation, thus far human experts are still superior to computer programs (*Meringer and Schymanski 2013*). However, applying complementary, automated methods in addition to manual analysis could be a beneficial add-on for the interpretation of MS data originating from sources of astrobiological interest. For instance, such spectra will be recorded by ESA's ROSETTA space probe when reaching its destination, comet 67P/Churyumov-Gerasimenko, in 2014.

#### References:

Kerber A., Laue R., Meringer M., Rücker C., Schymanski E.: Mathematical Chemistry and Chemoinformatics. Structure Generation, Elucidation and Quantitative Structure-Property Relationships. De Gruyter, 2013.

Lindsay R.K., Buchanan B.G., Feigenbaum E.A., Lederberg J.: Applications of Artificial Intelligence for Organic Chemistry: The DENDRAL Project. McGraw-Hill Book Company, 1980.

Meringer M., Cleaves H.J., Freeland S.J.: Beyond Terrestrial Biology: Charting the Chemical Universe of  $\alpha$ -Amino Acid Structures. J. Chem. Inf. Model., 53(11), 2851-2862, 2013.

Meringer M., Schymanski E.L.: Small Molecule Identification with MOLGEN and Mass Spectrometry. Metabolites., 3(2), 440-462, 2013.

De Vera J.-P., von Paris P.: Private communication. Rundgespräch "Astrobiologie", Berlin-Adlershof, 24 May 2013.

## 4.5 Jacobian Matrix of the Atmospheres of Earth-like Planets

*M. Vasquez, F. Schreier, T. Trautmann*

We intend to extend our previous research on the radiative transfer of Earth-like planets with clouds, for which the spectral appearance of exoplanets was investigated from calculations with a detailed analysis to identify the sources and sinks of the radiation. Since, in reality, there is limited information in the measured spectra of distant planets, it is essential to determine which atmospheric parameters can be retrieved in preparation to characterize the atmospheres of small size planets.

Sensitivity analysis based on the Jacobian can reveal which parameters can be retrieved independently and which parameters have to be set a priori, depending on the type of observation and spectral domain. This also allows to determine which atmospheric parameters can be considered to be more reliable for retrievals. A sensitivity study was performed – supported by students P. Hochstaffl (University Innsbruck), S. El Sayed, O. Pimenova, D. Schmidt (all TU Munich) – for different molecular species that were previously determined to be important in the atmospheres of Earth-like planets along with the atmospheric temperatures corresponding to various altitudes. Fig. 4-9 displays the Jacobians  $\partial I / \partial \vec{x}$  calculated for a planet around an M type of star and the different parameters that were perturbed. Here the state vector  $\vec{x}$  of parameters to be retrieved from the radiance spectrum  $I(o, \vec{x})$  comprises scaling factors for molecular densities, the temperatures at the ground, tropopause and stratopause together with the ground pressure, i.e.  $\vec{x} = (\alpha_{H_2O}, \alpha_{CO_2}, \alpha_{O_3}, T_g, T_t, T_s, p_g)$ .

First results indicate that the atmospheric parameters are more suitable to be retrieved from different spectral regions. For example, in case of  $O_3$ , the Jacobians show that its molecular concentrations in the atmosphere could be estimated from roughly  $1041 \text{ cm}^{-1}$  ( $9.6 \mu\text{m}$ ), where the molecule presents strong absorption. In case of  $CO_2$ , it is more reliable to derive its mixing ratios from about  $700 \text{ cm}^{-1}$  ( $15 \mu\text{m}$ ).

The future step in this study is directed to use the modeled and observed spectra to obtain the true atmospheric properties values by applying the knowledge gained behind this sensitivity study. This will be done through an inverse model that allows repetitive interactions between the spectra until a solution is found, i.e. an estimate of the true state of the atmosphere.

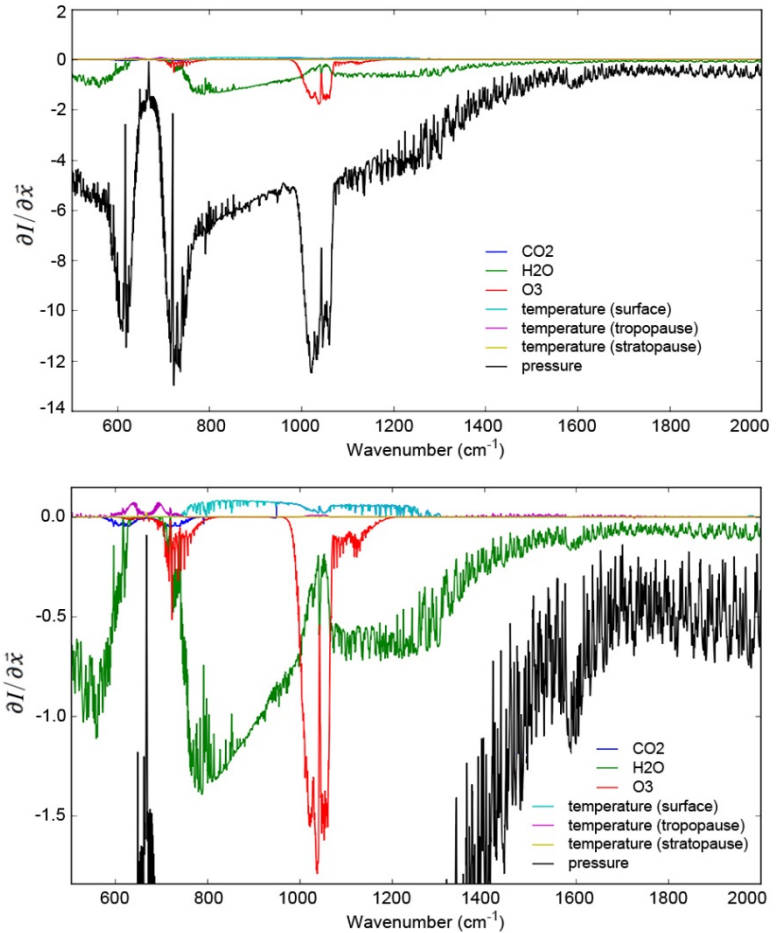


Fig. 4-9: Columns of the Jacobian matrix of the M star planet for all atmospheric parameters considered (top) and with a zoom in the y-axis (bottom).

## 4.6 Earth and Space Science Outreach Activities in the Dominican Republic

*M. Vasquez, S. Gimeno García*

With the remote sensing activities concerning the interpretation of the spectra of exoplanets our research has meanwhile expanded into space science and astronomy. Therefore, one of us participates in GalileoMobile (<http://www.galileo-mobile.org/>), an initiative inspired by the International Year of Astronomy 2009 (IYA2009) when it became a designated IYA2009 Special Project. Today, this initiative has been established to continue the efforts pursued during the IYA2009 and is actively planning and undertaking new expeditions. The GalileoMobile project is a purely non-profit activity run by astronomers, educators, and science communicators with support being provided by various research centers, including DLR. The project is conceived as a travelling science education program that brings astronomy closer to young people around the world, and mainly across regions that have little or no access to outreach actions. By organizing astronomy-related activities in schools and villages, we try to excite them about the wonders of our Universe. The places involved are provided with educational material as well as on-going support, so that educators can pursue astronomy activities after our visits.

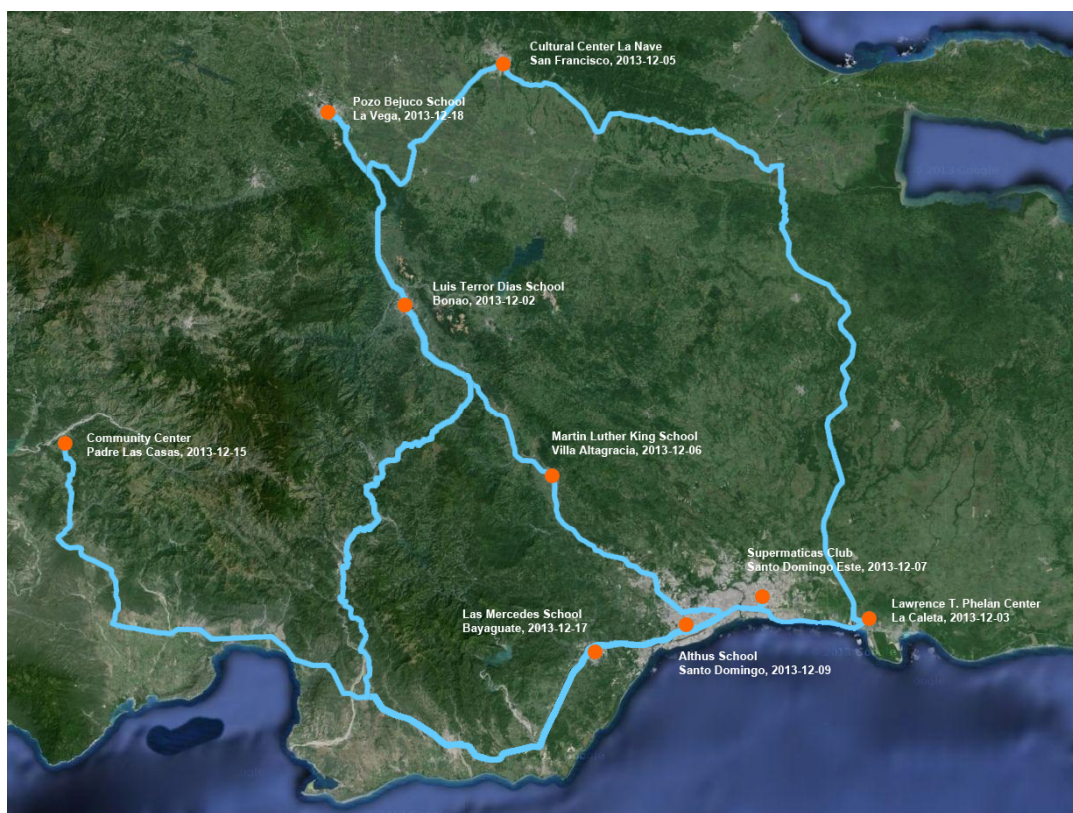


Fig. 4-10: Our GalileoMobile tour through the Dominican Republic.

In December 2013, we stayed for a month in the Dominican Republic and had enough time and motivation to also perform astronomical activities in the framework of a GalileoMobile-type campaign. The Caribbean region, including the Dominican Republic, has not yet been reached by GalileoMobile and has usually very little access to astronomy programs. Before travelling to the Caribbean, we contacted different organizations in Europe looking for material to be donated to the schools for the continuation of astronomical activities. DLR-EOC collaborated with posters and printed copies of the activities handbook and organized shipment of the entire package to the Caribbean.

On our tour between 2-18 December, we visited various towns and villages in different regions of the country. The schools shown in Fig. 4-10 educate children from less wealthy families. They all treated us in a really unique way. For example, when we went to the Cultural Center *La Nave* in San Francisco, we did what is called "pasacalles" by walking around the streets with an instrumental band while inviting people with a loudspeaker to join the activities. Many young and old people followed us.



Fig. 4-11: We both explaining the Solar System (left) and doing the “pasacalles” in San Francisco (right).

All centers visited were very interested in Earth and space sciences with some young students being particularly outstanding during our inaugural presentation and activity sections. What impressed the students a lot was our home planet’s relative small size in the universe, e.g. demonstrated by a photo of Earth as seen from Saturn. They got even more surprised when presenting an image of our galaxy and showing where the Solar System is located and how small our Sun is in comparison. We also addressed the atmosphere with the ozone layer and its importance for life on Earth. DLR’s posters were useful for explaining curious views of our home planet as seen from space.

We also had the chance to come out in two local newspapers (*El Nacional* and *Hoy*). This was very important in order to motivate other locals to continue with such activities. Two TV interviews were given – one in a studio and the other in a school during our presentation. They were aired on the news of the local channel 7 on 13 and 20 December, respectively. Finally we visited the technical university INTEC where we gave a lecture about astronomy in general and the activities that were initiated by GalileoMobile. We hope to have inspired some students in the audience to perform similar activities at local schools.



Fig. 4-12: One of us addressing the Earth’s atmosphere (left) and the other catching Sun spots (right).

Our tour was an extraordinary experience and we felt the community in general responded in a very enthusiastic way. We certainly try to organize an official expedition with the rest of the members of GalileoMobile. Next time we take holidays in the Dominican Republic, we will definitely conduct more activities. This was time worthy!



## 5. Documentation

### 5.1 Books and Book Contributions

- Afanas'ev, V., Efremenko, D., Lubenchenko, A.: On the application of the invariant embedding method and the radiative transfer equation codes for surface state analysis. In: *Light Scattering Reviews*, Springer, 363-423, ISBN 978-3-642-32105-4, 2013
- Ferrucci, F., Theys, N., Clarisse, L., Hirn, B., Laneve, G., Valks, P., Van Der A, R., Tait, S., Di Bartola, C., Brenot, H.: Operational integration of space borne measurements of Lava discharge rates and Sulphur Dioxide concentrations for Global Volcano Monitoring. In: F. Wensel and J. Zschau (eds.) *Early Warning for Geological Disasters – Scientific Methods and Current Practice*, ISBN: 978-3-642-12232-3, Springer Berlin Heidelberg New York, 2013
- Kerber, A., Laue, R., Meringer, M., Rücker, C., Schymanski, E.L.: *Mathematical Chemistry and Chemoinformatics*. De Gruyter, ISBN 978-3-11-025407-5, 2013
- Rother, T., Kahnert, M.: *Electromagnetic Wave Scattering on Nonspherical Particles: Basic Methodology and Simulations*. Springer Series in Optical Sciences, 145 (2<sup>nd</sup> edition), Springer, ISBN 978-3-642-00703-3, 2013

### 5.2 Journal Papers

- Afanas'ev, V., Efremenko, D., Ivanov, D., Kaplya, P., and Lubenchenko, A.: Photoelectron emission for layers of finite thickness. *Surface Investigation X-Ray, Synchrotron and Neutron Techniques*, 7 (2), 382-387, SP MAIK Nauka/Interperiodica, DOI: 10.1134/S1027451013020274, 2013
- Afanas'ev, V., Efremenko, D., and Lubenchenko, A.: Experimental verification of the technique for calculating light scattering in turbid media and determination of the single-scattering albedo based on the spectroscopy of elastically reflected electrons. *Surface Investigation X-Ray, Synchrotron and Neutron Techniques*, 7 (2), 285-289, SP MAIK Nauka/Interperiodica, DOI: 10.1134/S102745101302002X, ISBN 1027-4510, 2013
- Brenot, H., Theys, N., Clarisse, L., van Geffen, J., van Gent, J., Van Roozendael, M., van der A, R., Hurtmans, D., Coheur, P.-F., Clerbaux, C., Valks, P., Hedelt, P., Prata, F., Rason, O., Sievers, K., Zehner, C.: Support to Aviation Control Service (SACS): an online service for near real time satellite monitoring of volcanic plumes. *Nat. Hazards Earth Syst. Sci. Discuss.*, 1, 5935-6000, 2013
- Doicu, A., Efremenko, D., Trautmann, T.: A multi-dimensional vector spherical harmonics discrete ordinate method for atmospheric radiative transfer. *Journal of Quantitative Spectroscopy and Radiative Transfer*, 118, 121-131, DOI: 10.1016/j.jqsrt.2012.12.009, 2013
- Doicu, A., Efremenko, D., Trautmann, T.: An analysis of the short-characteristic method for the spherical harmonic discrete ordinate method (SHDOM). *Journal of Quantitative Spectroscopy and Radiative Transfer*, 114-127, DOI: 10.1016/j.jqsrt.2012.12.024, 2013
- Efremenko, D., Doicu, A., Loyola, D., Trautmann, T.: Acceleration techniques for the discrete ordinate method. *Journal of Quantitative Spectroscopy and Radiative Transfer*, 114, 73-81, DOI: 10.1016/j.jqsrt.2012.08.014, 2013
- Efremenko, D., Doicu, A., Loyola, D., Trautmann, T.: Small-angle modification of the radiative transfer equation for a pseudo-spherical atmosphere. *Journal of Quantitative Spectroscopy and Radiative Transfer*, 114, 82-90, DOI: 10.1016/j.jqsrt.2012.08.013, 2013
- Fioletov, V.E., McLinden, C.A., Krotkov, N., Yang, K., Loyola, D., Valks, P., Theys, N., Van Roozendael, M., Nowlan, C., Chance, K., Liu, X., Lee, C. and Martin, R.V.: Application of OMI, SCIAMACHY and GOME-2 satellite SO<sub>2</sub> retrievals for detection of large emission sources. *Journal of Geophysical Research*, DOI: 10.1029/2013JD019967, 2013

- Hedelt, P., von Paris, P., Godolt, M., Gebauer, S., Grenfell, J.L., Rauer, H., Schreier, F., Selsis, F., Trautmann, T.: Spectral features of Earth-like planets and their detectability at different orbital distances around F, G, and K-type stars. *Astronomy & Astrophysics*, 553, 1-14, DOI: 10.1051/0004-6361/201117723, 2013
- Kasai, Y., Sagawa, H., Kreyling, D., Suzuki, K., Dupuy, E., Sato, T.O., Mendrok, J., Baron, P., Nishibori, T., Mizobuchi, S., Kikuchi, K., Manabe, T., Ozeki, H., Sugita, T., Fujiwara, M., Irimajiri, Y., Walker, K.A., Bernath, P.F., Boone, C., Stiller, G., von Clarmann, T., Orphal, J., Urban, J., Murtagh, D., Llewellyn, E.J., Degenstein, D., Bourassa, A.E., Lloyd, N.D., Froidevaux, L., Birk, M., Wagner, G., Schreier, F., Xu, J., Vogt, P., Trautmann, T., Yasui, M.: Validation of stratospheric and mesospheric ozone observed by SMILES from International Space Station. *Atmospheric Measurement Techniques (AMT)*, 6 (2), 2643-2720, DOI: doi:10.5194/amt-6-2643-2013, 2013
- Khan, A., Trautmann, T., Blaschke, Majid, H.: (2013) Aerosol optical and radiative properties during summer and winter seasons over Lahore and Karachi. *Atmospheric Environment*, 50, 234-245, Elsevier, DOI: 10.1016/j.atmosenv.2011.12.027, 2013
- Meringer, M., Cleaves, H.J., Freeland, S.J.: Beyond Terrestrial Biology: Charting the Chemical Universe of  $\alpha$ -Amino Acid Structures. *Journal of Chemical Information and Modeling*, 53 (11), 2851-2862, DOI: 10.1021/ci400209n, 2013
- Meringer, M., Schymanski, E.L.: Small Molecule Identification with MOLGEN and Mass Spectrometry. *Metabolites*, 3 (2), 440-462, DOI: 10.3390/metabo3020440, ISSN 2218-1989, 2013
- von Paris, P., Grenfell, J.L., Hedelt, P., Rauer, H., Selsis, F., Stracke, B.: Atmospheric constraints for the CO<sub>2</sub> partial pressure on terrestrial planets near the outer edge of the habitable zone. *Astronomy and Astrophysics*, 549, DOI: 10.1051/0004-6361/201219684, 2013
- von Paris, P., Hedelt, P., Selsis, F., Schreier, F., Trautmann, T.: Characterization of potentially habitable planets: Retrieval of atmospheric and planetary properties from emission spectra. *Astronomy & Astrophysics*, 551, 1-14, EDP Sciences, DOI: 10.1051/0004-6361/201220009, ISBN 0004-6361, 2013
- von Paris, P., Gebauer, S., Godolt, M., Grenfell, J.L., Hedelt, P., Kitzmann, D., Patzer, A.B.C., Rauer, H., Stracke, B.: The extrasolar planet Gliese 581 d: a potentially habitable planet? (Corrigendum) *Astronomy & Astrophysics*, Volume 552, id.C1, 2013
- Safieddine, S., Clerbaux, C., George, M., Hadji-Lazaro, J., Hurtmans, D., Coheur, P.-F., Wespes, C., Loyola, D., Valks, P., Hao, N.: Tropospheric ozone and nitrogen dioxide measurements in urban and rural regions as seen by IASI and GOME-2. *Journal of Geophysical Research*, DOI: 10.1029/2013JD019660, 2013
- Spurr, R., Natraj, V., Lerot, C., Van Roozendael, M., Loyola, D.: Linearization of the Principal Component Analysis method for radiative transfer acceleration: Application to retrieval algorithms and sensitivity studies. *Journal of Quantitative Spectroscopy and Radiative Transfer*, 125, 1-17, DOI: 10.1016/j.jqsrt.2013.04.002, 2013
- Vasquez, M., Gottwald, M., Gimeno García, S., Krieg, E., Lichtenberg, G., Schreier, F., Slijkhuis, S., Snel, R., Trautmann, T.: Venus observations from ENVISAT-SCIAMACHY: Measurements and modeling. *Advances in Space Research*, 51, 835-848, DOI: 10.1016/j.asr.2012.09.046, 2013
- Vasquez, M., Schreier, F., Gimeno García, S., Kitzmann, D., Patzer, B., Rauer, H., Trautmann, T.: Infrared radiative transfer in atmospheres of Earth-like planets around F, G, K, and M stars - I. Clear-sky thermal emission spectra and weighting functions. *Astronomy and Astrophysics*, 549 (A26), 1-13, DOI: 10.1051/0004-6361/201219898, 2013
- Vasquez, M., Schreier, F., Gimeno García, S., Kitzmann, D., Patzer, B., Rauer, H., Trautmann, T.: Infrared radiative transfer in atmospheres of Earth-like planets around F, G, K, and M stars. II. Thermal emission spectra influenced by clouds. *Astronomy and Astrophysics*, 557 (A46), 1-14, DOI: 10.1051/0004-6361/201220566, 2013

- Xu, J., Schreier, F., Vogt, P., Doicu, A., Trautmann, T.: A sensitivity study for far infrared balloon-borne limb emission sounding of stratospheric trace gases. *Geoscientific Instrumentation, Methods and Data Systems Discussions (GID)*, 3, 251-303, Copernicus DOI: 10.5194/gid-3-251-2013, 2013
- Zhou, D.R., Ding, A.J., Mao, H.T., Fu, C.B., Wang, T., Chan, L.Y., Ding, K., Zhang, Y., Liu, J., Lu, A., Hao, N.: Impacts of the East Asian monsoon on lower tropospheric ozone over coastal South China. *Environmental Research Letters*, 8 (044011), 1-7, DOI: 10.1088/1748-9326/8/4/044011. 2013

### 5.3 Conference Proceeding Papers and Presentations

- Coldewey-Egbers, M., Loyola, D., Van Roozendaal, M., Zimmer, W.: Total Ozone Trend Patterns from a Homogenized European Satellite Sensor Data Base. *ESA Living Planet Symposium*, Edinburgh, United Kingdom, 2013
- Coldewey-Egbers, M., Loyola, D., Aberle, B., Zimmer, W.: Long-term Degradation Analysis of GOME, SCIAMACHY, and GOME-2 Measured Radiances. *ACVE Workshop*, Frascati, Italy, 2013
- Delcloo, A., Loyola, D., Tuinder, O., Valks, P.: Validation of GOME-2 Tropospheric Ozone Column Products, using Balloon Sounding Data. *ACVE Workshop*, Frascati, Italy, 2013
- Delcloo, A., Loyola, D., Tuinder, O., Valks, P.: Validation of GOME-2/MetOp-A and GOME-2/MetOp-B tropospheric ozone column products, using balloon sounding data. *EUMETSAT Meteorological Satellite Conference*, Vienna, Austria, 2013
- Efremenko, D., Doicu, A., Loyola, D., Trautmann, T.: Accelerations of the Discrete Ordinate Method for Nadir Viewing Geometries. *AIP Conference Proceedings*, 1531, 55-58, DOI: 10.1063/1.4804706, 2013
- Efremenko, D., Doicu, A., Loyola, D., Trautmann, T.: Generalization of three-dimensional scalar model of the radiation transfer SHDOM on the vector case. *X All-Russian Open conference Current problems of remote sensing*, Moscow, Russia, 2013
- Efremenko, D., Doicu, A., Loyola, D., Trautmann, T.: On the implementation of the discrete ordinate method with small-angle approximation for a pseudo-spherical atmosphere. *EGU 2012*, Vienna, Austria, 2013
- Efremenko, D., Doicu, A., Loyola, D., Trautmann, T.: Analysis of dimensionality reduction techniques for ozone retrieval from GOME instruments. In: *Proceedings of Atmospheric radiation and dynamics*, Saint-Petersburg State University, ISARD 2013, Saint-Petersburg-Petrodvorets, Russia, 2013
- Eichmann, K.-U., Bovensmann, H., Noël, S., Richter, A., Wittrock, F., Buchwitz, M., Rozanov, A., Kokhanovsky, A., Burrows, J.P., Lerot, C., Van Roozendaal, M., Tilstra, L.G. Snel, R., Krijger, M., Lichtenberg, G., Doicu, A., Schreier, F., Hrechanyy, S., Gimeno García, S., Kretschel, K., Meringer, M., Hess, M., Gottwald, M., Dehn, A., Fehr, T., Brizzi, G.: Development of SCIAMACHY Operational ESA Level 2 Version 6 Products. In: *Proceedings of the ESA Living Planet Symposium*, ESA SP-722, Edinburgh, 2013
- Gottwald, M.: Heimat Erde - Das Bild unseres Planeten. Public lecture, Munich, 19 April 2013
- Gottwald, M., Fritz, T., Breit, H., Schättler, B., Harris, A.: Mapping Terrestrial Impact Craters with the TanDEM-X Digital Elevation Model. *4<sup>th</sup> TanDEM-X Science Team Meeting*, Oberpfaffenhofen, Germany, 2013
- Gottwald, M., Fritz, T., Breit, H., Schättler, B., Harris, A.: Mapping Terrestrial Impact Craters with the TanDEM-X Digital Elevation Model. *Large Meteorite Impacts and Planetary Evolution V*. Sudbury, Canada, 2013
- Gottwald, M., Krieg, E., Reissig, K., How, J., Brizzi, G., Dehn, A., Fehr, T.: The SCIAMACHY Consolidated Level 0 Dataset. In: *Proceedings of the ESA Living Planet Symposium*, ESA SP-722, Edinburgh, 2013

- Gottwald, M.: Fremde Welten - Raumsonden erkunden unser Sonnensystem. Public lecture, Munich, 6 December 2013
- Grossi, M., Valks, P., Slijkhuis, S., Loyola, D., Aberle, B., Beirle, S., Mies, K., Wagner, T., Gleisner, H., Nielsen, J., Lauritsen, K.: Validation of Water Vapour Column Density Product from the GOME, SCIAMACHY and GOME-2 Instruments. ACVE Workshop, Frascati, Italy, 2013
- Grossi, M., Valks, P., Slijkhuis, S., Loyola, D., Aberle, B., Beirle, S., Mies, K., Wagner, T., Gleisner, H., Nielsen, J., Lauritsen, K.: Water Vapour Column Density Time Series from the GOME, SCIAMACHY and GOME-2 Instruments. ESA Living Planet Symposium, Edinburgh, United Kingdom, 2013
- Grossi, M., Valks, P., Slijkhuis, S., Loyola, D., Aberle, B., Beirle, S., Mies, K., Wagner, T., Gleisner, H., Nielsen, J., Lauritsen, K.: Water vapour column density time series from the GOME, SCIAMACHY and GOME-2 instruments. EUMETSAT Meteorological Satellite Conference, Vienna, Austria, 2013
- Hamidouche, M.: Infrared Astronomy: Unveiling the Hidden Universe. Infrarottechnik-Grundlagen, Trends und moderne Anwendungen. Wessling, Germany, 2013
- Hao, N., Ding, A.J., Valks, P., Safieddine, S., Clerbaux, C., Trautmann, T.: Assessment of the Impact of The East Asian Summer Monsoon on the Air Quality Over China from space. EGU General Assembly, Vienna, Austria, 2013
- Hao, N., Ding, A.J.: East Asian Monsoon & Air quality. In: 2013 Dragon Brochure, Dragon 3 Symposium, Palermo, Italy, 2013
- Hao, N., Ding, A.J., Valks, P., Clerbaux, C., Safieddine, S., Hedelt, P., Wang, T., Trautmann, T.: Space Assessment of the impact of the East Asian Monsoon on the air quality over China. EUMETSAT Meteorological Satellite Conference, Vienna, Austria, 2013
- Hao, N., Ding, A.J., Valks, P., Safieddine, S., Clerbaux, C., Trautmann, T.: Assessment of the Impact of The East Asian Summer Monsoon on the Air Quality Over China from space. ESA Living Planet Symposium, Edinburgh, United Kingdom, 2013
- Hedelt, P., Valks, P., Loyola, D., van Gent, J., Van Roozendael, M., Theys, N., Hao, N., Zimmer, W.: Monitoring of Volcanic and Anthropogenic SO<sub>2</sub> Emissions using the GOME-2 Instruments Aboard METOP-A and B. ESA Living Planet Symposium, Edinburgh, United Kingdom, 2013
- Hedelt, P., Valks, P., Loyola, D., van Gent, J., Van Roozendael, M., Theys, N., Hao, N., Zimmer, W.: Monitoring of volcanic and anthropogenic SO<sub>2</sub> emissions using the GOME-2 instruments aboard METOP-A and B. EUMETSAT Meteorological Satellite Conference, Vienna, Austria, 2013
- Koukouli, M., Balis, D., Valks, P., Zimmer, W., Hao, N., Loyola, D., Lambert, J.-C., Lerot, C., Van Roozendael, M.: Continuing the total ozone record: validating the first six months of GOME-2/MetOp-B data. EUMETSAT Meteorological Satellite Conference, Vienna, Austria, 2013
- Koukouli, M., Lerot, C., Balis, D., Van Roozendael, M., Lambert, J.-C., Grainville, J., Spurr, R., Loyola, D., Zehner, C.: Validation of the total Ozone Climate Data Record from GOME, SCIAMACHY and GOME-2 as Part of the ESA Climate Change Initiative. ACVE Workshop, Frascati, Italy, 2013
- Lerot, C., Van Roozendael, M., Spurr, R., Loyola, D., Koukouli, M., Balis, D., Lambert, J.-C., van Gent, J., Granville, J., Zehner, C.: A Consistent Long-Term Total Ozone Data Record based on GOME, SCIAMACHY and GOME-2 as Part of the ESA Climate Change Initiative. ACVE Workshop, Frascati, Italy, 2013
- Lerot, C., Van Roozendael, M., Spurr, R., Loyola, D., Coldewey-Egbers, M., Koukouli, M., Balis, D., Lambert, J.-C., Granville, J., Goutail, F., Pommereau, J., Zehner, C.: An improved European Multi-Sensor Total Ozone Climate Data Record as Part of the ESA Climate Change Initiative. ESA Living Planet Symposium, Edinburgh, United Kingdom, 2013
- Lichtenberg, G., Gottwald, M., Doicu, A., Schreier, F., Hrechanyy, S., Meringer, M., Hess, M., Gimeno García, S., Noël, S., Eichmann, K.-U., Bovensmann, H., Liebig, P., Richter, A., Buchwitz, M., Rozanov, A., Burrows, J.P., Krijger, M., Snel, R., Lerot, C., Dehn, A.: SCIAMACHY – New Algorithms for Operational Processors. Proceedings of the International Geoscience and Remote Sensing Symposium (IGARSS 2013), Melbourne, Australia, 2013

- Lichtenberg, G., Slijkhuis, S., Aberle, B., Gimeno García, S., Noël, S., Bramstedt, K., Snel, R., Krijger, J.M., v. Hees, R., Dehn, A.: SCIAMACHY: First review of calibration parameters for the SWIR channels. ESA Living Planet Symposium, Edinburgh, United Kingdom, 2013
- Lichtenberg, G., Slijkhuis, S., Aberle, B., Sherbakov, D., Noël, S., Bramstedt, K., Liebing, P., Bovensmann, H., Snel, R., Krijger, J.M., v. Hees, R., Lerot, C., Dehn, A.: SCIAMACHY: New Algorithms for the Operational Level 0-1 Processor. ESA Living Planet Symposium, Edinburgh, United Kingdom, 2013
- Loyola, D.: Satellite remote sensing of trace gases and clouds, Meteorologisches Kolloquium. LMU, Munich, November 2013
- Loyola, D., Gimeno García, S., Doicu, A., Spurr R.: Retrieval of Macrophysical Cloud Parameters from Sentinel 5 Precursor. ESA Living Planet Symposium, Edinburgh, United Kingdom, 2013
- Meringer, M.: Biomolecules in Astrobiology. Research Seminar of the Helmholtz Alliance Planetary Evolution and Life, Berlin Adlershof, 8 May 2013
- von Paris, P., Hedelt, P., Selsis, F., Schreier, F., Trautmann, T.: Retrieval of atmospheric properties of terrestrial exoplanets through spectroscopic characterization. 527. Wilhelm und Else Heraeus-Seminar: Plasma and Radiation Environment in Astrospheres and Implications for the Habitability of Extrasolar Planets, Bad Honnef, Germany, 2013
- von Paris, P., Hedelt, P.: Calculating spectral signatures of atmospheric biosignatures for Earth-like planets based on an E-ELT configuration. 6th HGF Alliance Week, Berlin, 2013
- von Paris, P., Hedelt, P., Selsis, F., Schreier, F., Trautmann, T.: Retrieval of atmospheric properties for habitable planets. Protostars and Planets VI, Heidelberg, 2013
- Schreier, F., Gimeno García, S.: Py4CATS - Python Tools for Line-by-Line Modelling of Infrared Atmospheric Radiative Transfer. AIP Conference Proceedings, 1531, 123-126, American Institute of Physics, DOI: 10.1063/1.4804723, 2013
- Schreier, F., Xu, J., Doicu, A., Vogt, P., Trautmann, T.: Deriving Stratospheric Trace Gases From Balloonborne Infrared/Microwave Limb Sounding Measurements. AIP Conference Proceedings, 1531, 392-395, American Institute of Physics, DOI: 10.1063/1.4804723, 2013
- Schreier, F., Gimeno García, S., Milz, M., Kottayil, A., Höpfner, M., von Clarmann T., Stiller, G.: Intercomparison of three microwave/infrared high resolution line-by-line radiative transfer codes. AIP Conference Proceedings, 1531, 119-122, American Institute of Physics, DOI: 10.1063/1.4804723, 2013
- Valks, P., N. Hao, N., P. Hedelt, P., W. Zimmer, W., D. Loyola, D.: GOME-2 observations of air quality in Chinese megacities. PRESCRIBE Workshop, Bremen, Germany, 2013
- Valks, P., Hao, N., Hedelt, P., Zimmer, W., Loyola, D., Pinardi, G., Van Roozendael, M., De Smedt, I., Theys, N., Lambert, J.-C., Koukouli, M., Balis, D.: Trace gas column observations from the GOME-2 instruments on MetOp-A and B. EUMETSAT Meteorological Satellite Conference, Vienna, Austria, 2013
- Van Roozendael M., Braesicke, P., Dameris, M., Lambert, J.-C., Loyola, D., van der A, R., Weber, M., Wolfmueller, M., Zehner C.: Overview of Results from the ESA Ozone\_cci Project. ESA Living Planet Symposium, Edinburgh, United Kingdom, 2013
- Veefkind, P., Loyola, D., Richter, A., Aben, I., Van Roozendael M., de Smedt, I., Siddans, R., Wagner, T., Nett, H.: Sentinel 5 Precursor / TROPOMI: Science Opportunities and Level-2 Products. ESA Living Planet Symposium, United Kingdom, 2013
- Wagner, T., Beirle, S., Mies, K., Loyola, D., Valks, P., Grossi, M.: Investigation of the effect of ground pixel size on the retrieval of the atmospheric H<sub>2</sub>O column from UVVIS satellite instruments. EUMETSAT Meteorological Satellite Conference, Vienna, Austria, 2013
- Zehner C., Aben, I., Fehr, T., Ingmann, P., Loyola, D., Van Roozendael M.: Sentinel 5P for Science Use. ESA Living Planet Symposium, Edinburgh, United Kingdom, 2013

## 5.4 Attended Conferences

Volcanic Ash Strategic Initiative Team (VAST) User Workshop, Dublin, Ireland, 4-6 March 2013

ACVE Workshop – ESA/ESRIN, Frascati, Italy, 13-15 March 2013

527. Wilhelm und Else Heraeus-Seminar: Plasma and Radiation Environment in Astrospheres and Implications for the Habitability of Extrasolar Planets. Bad Honnef, Germany, 10-15 March 2013

European Geosciences Union General Assembly, Vienna, Austria, 7-12 April 2013

HGF Evaluierung, Cologne, Germany, 17-19 April 2013

Research Seminar of the Helmholtz Alliance Planetary Evolution and Life, Berlin, Germany, 8 May 2013

Pollution Studied by Remote Sensing of Conurbations/Megacities and Retrieved from Observations Made by Instrumentation on Space Based Platforms (PRESCRIBE), ACCENT Plus and ICACGP Workshop, Bremen, Germany, 15-16 May 2013

6<sup>th</sup> HGF Alliance Week. Berlin, Germany, 20-23 May 2013

7<sup>th</sup> International Symposium on Radiative Transfer, Kusadasi, Turkey, 2-8 June 2013

Dragon 3 Symposium, Palermo, Italy, 3-7 June 2013

4<sup>th</sup> TanDEM-X Science Team Meeting, Oberpfaffenhofen, Germany, 12-14 June 2013

Atmospheric Radiation and Dynamics (ISARD 2013) Saint Petersburg, Russia, 24-27 June 2013

MACC joint AER-GRG-VAL Workshop, Wermelskirchen, Germany, 26-28 June 2013

2<sup>nd</sup> Workshop on Studies of Atmospheric Aerosol Using Multi-Angle Spectropolarimetry (ISSI), Bern, Switzerland, 15-19 July 2013

Protostars and Planets VI. Heidelberg, Germany, 14-20 July 2013

Large Meteorite Impacts and Planetary Evolution V. Sudbury, Canada, 5-8 August 2013

ESA Living Planet Symposium 2013, Edinburgh, United Kingdom, 9-13 September 2010

Joint EUMETSAT Meteorological Satellite Conference & 19<sup>th</sup> Satellite Meteorology, Oceanography, and Climatology Conference of the American Meteorological Society, Vienna, Austria, 16-20 September 2013

## 5.5 Academic Degrees

- Fischer, P.: Solving Optimization and Inverse Problems in Remote Sensing by using Evolutionary Algorithms. Master thesis in Geodesy and Geoinformation master course at TUM, May 2013 (Supervisors: Dr. Diego Loyola and Dr.-Ing. Stefan Auer, Technical University of Munich)
- Gimeno García, S.: Simulation of solar radiative transfer and comparison with spectro-radiometric measurements. Dissertation, Faculty of Physics and Earth Science, University of Leipzig. (Supervisor: Prof. Dr. Thomas Trautmann)
- Köhler, C. H.: Radiative Effects of Mixed Mineral Dust and Biomass Burning Aerosol in the Thermal Infrared. Dissertation, Faculty of Physics and Earth Science, University of Leipzig, thesis defence completed in December 2013. (Supervisors: Prof. Dr. Manfred Wendisch, University of Leipzig and Prof. Dr. Thomas Trautmann)
- Loyola, D.: Methodologies for solving Satellite Remote Sensing Problems using Neuro Computing Techniques. Dissertation, Faculty of Civil Engineering and Surveying, Technical University of Munich, thesis defence completed in April 2013. (Supervisors: Prof. Dr. Richard Bamler, Technical University of Munich, Prof. Martin Wirsing and Prof. Bernhard Mayer, both Ludwig-Maximilians-University Munich)
- Schüssler, O.: Combined Inversion Methods for UV/VIS Nadir Sounding. Dissertation, Civil Engineering and Surveying, Technical University of Munich. (Supervisors: Prof. Dr. Richard Bamler, Dr. Adrian Doicu and Dr. Diego Loyola)
- Vasquez, M.: Radiative transfer in planetary atmospheres with clouds. Dissertation, Centre of Astronomy and Astrophysics, Technical University of Berlin, thesis defence completed in November 2013. (Supervisors: Prof. Dr. Heike Rauer, German Aerospace Center, Institute of Planetary Research, Dr. Franz Schreier and Prof. Dr. Thomas Trautmann)
- Xu, J.: Inversion for Limb Infrared Atmospheric Sounding. Dissertation, Civil Engineering and Surveying, Technical University of Munich. (Supervisors: Prof. Dr. Richard Bamler, Dr. Franz Schreier, and Prof. Dr. Thomas Trautmann)

## 5.6 Seminar Talks

- Michael Hess: VINO - Regularized Retrieval of Trace Gas Profiles From IR Spectra, 22 January 2013
- Lee Grenfell (DLR-IPF and TUB-ZAA): Atmospheric Biomarkers, 27 February 2013
- Philipp Hochstaffl (University Innsbruck): Exoplanet Remote Sensing: Feasibility of Atmospheric Retrievals, 27 March 2013
- Denis Sherbakov: Privacy on the Internet, 17 April 2013
- Peter Fischer: Solving Inverse Problems in Remote Sensing by using Evolutionary Algorithms, 7 May 2013
- Margherita Grossi: Unsolved Mysteries of the Universe: Dark Energy and Non-Gaussianity, 11 June 2013
- Karsten Schmidt: Zur Untersuchung des Einflusses nichtsphärischer Partikelformen auf die ADM-Aeolus L1B-Windgeschwindigkeiten, 9 July 2013
- Yuri Eremin (Moscow State University): Discrete Sources Method in Electromagnetic Scattering Theory, 24 September 2013
- Mayte Vasquez: Radiative Transfer in Planetary Atmospheres with Clouds, 25 October 2013



## Abbreviations and Acronyms

3MI	Multi-viewing Multi-channel Multi-polarization Imager
AAI	Aerosol Absorbing Index
ADM	Atmospheric Dynamic Mission
AMF	Airmass Factor
AMIL2DA	Advanced MIPAS Level 2 Data Analysis
AMSU	Advanced Microwave Sounding Unit
ARTS	Atmospheric Radiative Transfer Simulator
ATBD	Algorithm Theoretical Baseline Document
ATP	Atmosphärenprozessoren
BDM	Brion-Daumont-Maliget
BIRA	Belgisch Instituut voor Ruimte-Aëronomie
BIRRA	Beer Infrared Retrieval Algorithm
BU	Binary Unit
CAL	Clouds-as-Layers
CarbonSat	Carbon Monitoring Satellite
CCD	Convective-Cloud-Differential
CCI	Climate Change Initiative
CDOP	Continuous Development and Operations Phase
CIR	Colour Index Ratio
CNES	Centre Nationale d'Etudes Spatiales
CRB	Clouds-as-Reflecting-Boundaries
DAOD	Differential Absorption Optical Depth
DENDRAL	Dendritic Algorithm
DFD	Deutsches Fernerkundungsdatenzentrum
DLR	Deutsches Zentrum für Luft- und Raumfahrt
DNSMI	Dynamical Normalized Seasonality Monsoon Index
DOAS	Differential Optical Absorption Spectroscopy
DU	Dobson Unit
DWT	Discrete Wavelet Transform
E2S	End-to-End Simulator
EAM	East Asian Monsoon
Eawag	Eidgenössische Anstalt für Wasserversorgung, Abwasserreinigung und Gewässerschutz
ECMWF	European Centre for Medium-Range Weather Forecasts
ECV	Essential Climate Variable
ENVISAT	Environmental Satellite
EOC	Earth Observation Center
EOS	Earth Orbiting System
EPS-SG	EUMETSAT Polar System Second Generation
ERS	European Remote Sensing Satellite
ESA	European Space Agency
EUMETSAT	European Organisation for the Exploitation of Meteorological Satellites
EVOSS	European Volcano Observatory Space Services
EXV	Experimentelle Verfahren
FIR	Far-Infrared
FLEX	Fluorescence Explorer
FO	First Order
FoV	Field-of-View
FTS	Fourier Transform Spectrometer
FWHM	Full Width Half Maximum
GARLIC	Generic Atmospheric Radiation Line-by-Line Infrared Code
GCAPS	Generic Calibration Processing System
GDP	GOME Data Processor
GFED	Global Fire Emissions Database

GODFIT	GOME Direct Fitting
GOME	Global Ozone Monitoring Experiment
GTO	GOME-type Total Ozone
HITRAN	High Resolution Transmission
HKO	Hong Kong Observatory
HSRL	High Spectral Resolution Lidar
HYSPLIT	Hyper Single-Particle Lagrangian Integrated Trajectory
ICGCR	Institute for Climate and Global Change Research
IMF	Institut für Methodik der Fernerkundung
INTEX-B	Intercontinental Chemical Transport Experiment Phase B
IPA	Institut Physik der Atmosphäre
IPDA	Integrated Path Differential Absorption
IR	Infrared
IRS	Infrared Sounder
IRTMW01	International Radiative Transfer Workshop 2001
ISRF	Instrument Spectral Response Function
IUP-IFE	Institut für Umweltphysik / Institut für Fernerkundung
IYE	International Year of Astronomy
JPL	Jet Propulsion Laboratory
KNMI	Koninklijk Nederlands Meteorologisch Instituut
KOPRA	Karlsruhe Optimized and Precise Radiative Transfer Algorithm
L2	Level 2
LbL	Line-by-Line
LEA	Locality Embedded Analysis
Lidar	Light detection and Ranging
LIDORT	Linearized Discrete Ordinate Radiative Transfer
LMM	Linear Mixing Model
LPDM	Lagrangian Particle Dispersion Modelling
LPE	Locality Pursuit Embedding
LPP	Locality Preserving Projection
LT	Local Time
LUT	Look-up Table
LWC	Liquid Water Content
MACC	Monitoring Atmospheric Composition and Climate
MERIS	Medium Resolution Imaging Spectrometer
MERLIN	Methane Remote Sensing Lidar Mission
MetOp	Meteorological Operational Polar Satellites of EUMETSAT
MF	Methodik der Fernerkundung
MIPAS	Michelson Interferometer for Passive Atmospheric Sounding
MIRART	Modular Infrared Atmospheric Radiative Transfer
MLS	Microwave Limb Sounder
MoCaRT	Monte Carlo Radiative Transfer
MOPITT	Measurements of Pollution in the Troposphere
MPIC	Max-Planck-Institut für Chemie
MS	Mass Spectrometry
MTG-S	Meteosat Third Generation Sounder
MTP	Microwave Temperature Profiler
NASA	National Aeronautics and Space Administration
NH	Northern Hemisphere
NIR	Near-Infrared
NLC	Noctilucent Cloud
NOAA	National Oceanic and Atmospheric Administration
NPOESS	National Polar-orbiting Environmental Satellite System
NPP	NPOESS Preparatory Project
NRT	Near-realtime
O3M	Ozone Monitoring
OCRA	Optical Cloud Recognition Algorithm

OFL	Offline
OMCLDO2	OMI Level 2 Cloud Product (Cloud Pressure and Fraction using O <sub>2</sub> -O <sub>2</sub> Absorption)
OMCLDRR	OMI Level 2 Cloud Product (Cloud Pressure and Fraction using Raman Scattering)
OMI	Ozone Monitoring Instrument
OPAC	Optical Properties of Aerosols and Clouds
OPACN	New OPAC
ORR	Operational Readiness Review
PALM	Parallelized Large-Eddy-Simulation Model
PCA	Principal Component Analysis
PDGS	Payload Data Ground Segment
PBL	Planetary Boundary Layer
QSPR	Quantitative Structures Property Relationship
REP	Reprocessing
PILS	Profile Inversion for Limb Sounding
PMD	Polarization Measurement Device
PQM	Product Quality Monitoring
PSC	Polar Stratospheric Cloud
RAL	Rutherford Appleton Laboratory
RMS	Root Mean Square
ROCINN	Retrieval of Cloud Information using Neural Networks
RT	Radiative Transfer
S5	Sentinel 5
S5P	Sentinel 5 Precursor
SAA	South Atlantic Anomaly
SACS	Support to Aviation Control Service
SAF	Satellite Application Facility
SAMUM	Sahara Mineral Dust Experiment
SBUV	Solar Backscatter Ultraviolet
SCD	Slant Column Density
SCIAMACHY	Scanning Imaging Absorption Spectrometer for Atmospheric Chartography
SHDOM	Spherical Harmonic Discrete Ordinate Method
SMASH	Study of an End-to-End System for the Monitoring of Volcanic Ash
SMHI	Swedish Meteorological and Hydrological Institute
SMILES	Superconducting Submillimeter-Wave Limb Emission Sounder
SQWG	SCIAMACHY Quality Working Group
SRF	Spectral Response Function
SRON	Netherlands Institute for Space Research
SSM/IS	Special Sensor Microwave Imager/Sounder
STM	Stochastic Model
SWIR	Shortwave Infrared
TCWV	Total Column Water Vapour
TELIS	TeraHertz Limb Sounder
TROPOMI	Tropospheric Ozone Monitoring Instrument
TU	Technical University
UTLS	Upper Troposphere Lower Stratosphere
UV	Ultraviolet
UVN	UV-VIS-NIR
UVNS	UV-VIS-NIR-SWIR
VCD	Vertical Column Density
VDISORT	Vector Discrete-Ordinate Radiative Transfer
VII	Visible Infrared Imager
VIS	Visible
WMO	World Meteorological Organization



## DLR at a Glance

DLR is the national aeronautics and space research center of the federal Republic of Germany. Its extensive research and development work in aeronautics, space, energy, transport and security is integrated into national and international cooperative ventures. In addition to its own research, as Germany's Space Agency DLR has been given responsibility by the federal government for the planning and implementation of the German space program. DLR is also the umbrella organization for the nation's largest project management agency.

Approximately 7700 people are employed at 16 locations in Germany: Cologne (headquarters), Augsburg, Berlin, Bonn, Braunschweig, Bremen, Göttingen, Hamburg, Jülich, Lampoldshausen, Neustrelitz, Oberpfaffenhofen, Stade, Stuttgart, Trauen and Weilheim. DLR has also offices in Brussels, Paris, Tokyo and Washington, D.C.

### Remote Sensing Technology Institute Institut für Methodik der Fernerkundung

DLR's Remote Sensing Technology Institute (IMF) is located in Oberpfaffenhofen, Berlin-Adlershof, Bremen and Neustrelitz.

IMF carries out research and development for retrieving geoinformation from remote sensing data. It conducts basic research on physical principles of remote sensing and develops algorithms, techniques, and operational processing systems for synthetic aperture radar, optical remote sensing, and spectrometric sounding of the atmosphere. The processing systems are in operational use for national, European, and international Earth observation missions.

For preparation and in support of space missions, IMF operates a suite of optical airborne sensors and laboratories. The institute contributes its expertise to novel sensor and mission concepts.

The German Remote Sensing Data Center (DFD) and MF form DLR's Earth Observation Center (EOC).



DLR

**Deutsches Zentrum  
für Luft- und Raumfahrt e.V.**

in der Helmholtz-Gemeinschaft

**Institut für Methodik der Fernerkundung**

Oberpfaffenhofen  
82234 Weßling

[www.dlr.de/eoc](http://www.dlr.de/eoc)